Modelling and Fabrication of inhalable microbubbles for drug targeting in the lungs

Hyunhong Min

Kellogg College

University of Oxford

Supervised by

Professor Eleanor Stride

Professor Stephen Payne

29th Feb 2024

This thesis is submitted to the Department of Engineering Science, University of Oxford, in fulfilment of the requirements for the degree of Doctor of Philosophy

Abstract

Microbubble ultrasound contrast agents have been used safely and effectively in diagnostic applications for several decades. Although their use in the lungs has not been widely explored due to safety concerns and poor ultrasound penetration through gas-filled tissue, the fragile and low-density properties of microbubbles make them attractive for drug delivery. This thesis aims to investigate the potential of microbubbles as inhalable agents for treating lung conditions.

Chapters 2 to 4 of the thesis explored the potential of microbubbles for targeting small conducting airways using an in silico method. Chapter 2 reviewed the existing literature on lung particle deposition models, and an in silico lung particle deposition model was developed in Chapter 3. However, an alternative approach to drug targeting in small conducting airways was proposed in Chapter 4. It was found that existing medical devices could achieve this without needing microbubbles by controlling the tidal volume and flow rate.

The latter part of the thesis focuses on exploring the feasibility of using inhalable microbubbles to treat neonatal respiratory distress syndrome (nRDS). Chapter 5 reviewed the relevant literature on nRDS, and identified three critical aspects for effective treatment: 1) delivering surfactant into the lungs of preterm infants, 2) maintaining low surface tension on the lung surface lining, and 3) the immunomodulatory action of lung surfactant proteins. Chapter 6 demonstrated that incorporating microbubbles in aerosols improved post-extrathoracic penetration in a 3D-printed preterm model. Chapter 7 showed that microbubbles enhance the surface activity of phospholipids, resulting in low surface tension on the air-aqueous interface, even with a low concentration of phospholipids. In Chapter 8, in vitro experiments on LPS-induced RAW264.7 macrophages suggested that microbubbles may have immunomodulatory effects. Overall, the work in this second half of the thesis demonstrates that inhalable microbubbles hold the potential for treating nRDS through nebulization.

Statement of originality

I hereby declare that this submission is my own work and, to the best of my knowledge, it contains no materials previously published or written by another person, or substantial proportions of material which have been accepted for the award of any other degree or diploma at the University of Oxford or any other educational institution, except where due acknowledgement is made in the thesis.

Any contribution made to the research by others, with whom I have worked at the University of Oxford or elsewhere, is explicitly acknowledged in the thesis. I also declare that the intellectual content of this thesis is the product of my own work, except to the extent that assistance from others in the project's design and conception or in style, presentation and linguistic expression is acknowledged.

HJ Min

Hyunhong Min

Feb 2024

Acknowledgements

Completing my D.Phil would not have been possible without the support, guidance and advice from many people during my time in Oxford.

First and foremost, I would like to express my gratitude to my two supervisors who have been instrumental in the completion of this thesis. Without Professor Eleanor Stride's unwavering support, this project would not have been possible. I am immensely grateful for her encouragement and mentorship throughout my D.Phil. program. She has not only taught me how to be a scientist but also how to be a good mentor. Professor Stephen Payne has helped me navigate through my first experience with mathematical modelling. With his guidance, I was able to challenge myself and delve into an unfamiliar area of study.

I feel incredibly lucky to have had the opportunity to work with such brilliant people in both BUBBL and the Cerebral Haemodynamics Group. I want to express my gratitude to Luca Bau who has always been my go-to person for scientific discussions on all sorts of crazy experiments. I also want to thank Dr. Nikolaos Kanellakis and Nikita Manoharan for teaching me the ins and outs of cell culture. Throughout all the ups and downs, I've learned so much from them. I want to give a sincere thanks to everyone in both groups for their friendly advice and for making the D.Phil experience so enjoyable. I'd also like to mention Luna - thank you for being a part of our lab. Your infectious laughter always made the lab a more cheerful place, and you will be greatly missed.

Outside of the lab, I am grateful to my uni boys Jason, Ben, and Jay for helping me forget all the stresses of my D.Phil and enjoy life. Many thanks to MJ and the Muay Thai team at OMAA for providing regular gym sessions to blow off some steam and keep my sanity in check. I would like to express my appreciation to everyone on the pharmacy team at Boots, Oxford retail park, for all the wonderful chats over tea and biscuits during my night shifts

I would like to thank Professor Suk-Chul Bae for being a scientific inspiration for over a decade. I was always fascinated by our conversations and his insights into the mysterious nature of science and the way it reveals the truth. I thank you for your decades of service to science, and wish you all the best with your post-academic life.

Dad, Mum, Yoonhong, and Eunhong; thank you for always being there in my life. Life is better knowing I have you on my side. And Yurim, you are the best thing that has happened to me past 3 years in Oxford. You remind me it’s the simple things that matter like our daily wine and dine nights. Thank you for being there for me and I look forward to our adventures together.

Statement of Contributions

Chapter 1

- This introductory section is entirely my own work.
- This chapter was reviewed by Professors Eleanor Stride and Stephen Payne prior to submission.

Chapter 2

- This literature review is entirely my own work.
- This chapter was reviewed by Professors Eleanor Stride and Stephen Payne prior to submission.

Chapter 3

- The results in this section are entirely my own work.
- This chapter was supervised and reviewed by Professors Eleanor Stride and Stephen Payne.

Chapter 4

- The results in this section are entirely my own work.
- This chapter was supervised and reviewed by Professors Eleanor Stride and Stephen Payne.

Chapter 5

- This literature review is entirely my own work.
- This chapter was reviewed by Professors Eleanor Stride and Stephen Payne prior to submission.

Chapter 6

- The 3D-printed model of a preterm neonate was made with the help of several people. ‘Paul’ model (Sim Characters GmbH) was kindly provided by Dr. Zoltan Molnar & Dr. Sanja Zivanovic from Oxford University Hospital (OUH). Mr. Sathees Kuttappan (OUH) performed CT scan of the model. Dr. Xinghao Cheng converted the NIfTI file to STL. Dr. Peter Walters helped to 3D-print the preterm model.
- The rest of the results are entirely my own work.

- This chapter was supervised and reviewed by Professors Eleanor Stride and Stephen Payne.

Chapter 7

- Dr. Luca Bau was instrumental for discussions on experimental design and interpretation of the results.
- The results are entirely my own work.
- This chapter was supervised and reviewed by Professors Eleanor Stride and Stephen Payne.

Chapter 8

- Dr. Nikolaos Kanellakis and Nikita Manoharan performed plasmid transfection of RAW264.7 macrophage, helped with general cell culture.
- Dr. Nikolaos Kanellakis taught and helped with Luminex Assays.
- The rest of the results are entirely my own work.
- This chapter was supervised and reviewed by Dr. Nikolaos Kanellakis, Professors Eleanor Stride and Stephen Payne.

Chapter 9

- This concluding chapter and suggestions for further work are entirely my own work.
- This chapter was supervised and reviewed by Dr. Nikolaos Kanellakis, Professors Eleanor Stride and Stephen Payne

Dissemination

Peer-Reviewed Journal Papers

Min, H.J., Stride, E.P., Payne, S.J., 2023. *'In silico investigation of the effect of particle diameter on deposition uniformity in pulmonary drug delivery',* Aerosol Science and Technology 57 (4), 318-328.

Min, H.J., Payne, S.J., Stride, E.P., 2024. *'Modelling drug delivery to the small airways: optimization using Response Surface Methodology',* Pharmaceutical Research (2024): 1-10.

Min, H.J., Payne, S.J., Stride, E.P., 2024. *'Microbubble-laden aerosols improve post-nasal penetration efficiency in a preterm neonate model',* International Journal of Pharmaceutics (Under Review).

Min, H.J., Bau, L., Bernardino de la Serna J., Payne, S.J., Stride, E.P., 2024. *'Microbubbles for lung surfactant therapy',* (Under review, ACS Applied materials and interfaces)

Conference Presentations

Min, H.J., Payne, S.J., Stride, E.P., 2021. *'Modeling interaction of particle size and breathing characteristics, and their optimization for maximum lung regional deposition' (Poster),* Journal of aerosol medicine and pulmonary drug delivery 34 (5), A11-A11

Jeon, S.*, Min, H.J.*, Payne, S.J., Stride, E.P., 2021. *'Effect of budesonide aerosol particle size on systemic exposure using in silico whole lung particle deposition coupled pharmacokinetics model' (Poster),* AAPS PharmSci 360, USA.

*indicate equal contributions.

Content

Chapter 1 Introduction

The use of microbubble ultrasound contrast agents in diagnostic applications has been established as safe and effective over several decades. Recent clinical trials have also demonstrated the potential of bubbles in therapeutic applications; e.g. for drug delivery across the blood-brain barrier and into solid tumours. However, the use of microbubbles and ultrasound in the lungs has not been widely explored due to the poor penetration of ultrasound through gas-filled tissue [1], [2]. Despite this limitation, the unique properties of microbubbles, such as their low density and fragility, are potentially attractive for drug delivery. The aim of this thesis was to explore the possible applications of microbubbles as inhalable agents for the treatment of various lung conditions, such as asthma and chronic obstructive pulmonary disease (COPD).

Inhalation therapy has greatly improved clinical outcomes for asthmatic and COPD patients since the advent of pressurised metered-dose inhalers in 1955, making inhalation a convenient and reliable method of drug delivery. However, despite these improvements, a significant proportion of patients continue to experience deterioration of their condition, resulting in poor quality of life and sometimes hospitalisation. The small conducting airways have received increasing attention in asthma and COPD management in recent years. These airways, also known as the "silent zone" of the lungs, were historically overlooked due to their accounting for only a small fraction of airway resistance in healthy lungs. However, recent research has demonstrated that closures of small conducting airways are responsible for emphysematous destruction and increased peripheral airway resistance in patients. Consequently, targeting therapy to small conducting airways has become an active area of research in asthma and COPD management.

Therapeutic targeting of the small conducting airways remains a challenging task. Studies using computational fluid dynamics (CFD) simulations have demonstrated that conventional dry powder inhalers and metered-dose inhalers deliver very little to the small conducting airways. This is primarily due to the fact that conventional aerosols cannot effectively target the small conducting airways, as particles with a mass median aerodynamic diameter (MMAD) greater than 3 μm deposit mainly in the upper airways, while smaller particles tend to deposit throughout the lungs.

To address this issue, we hypothesized that particles capable of changing their size at the target site could successfully achieve drug targeting in the lungs. We suggested that microbubbles, which have a low density and can fragment into smaller particles, are a potential candidate for targeting the small conducting airways. Due to the COVID-19 outbreak, this project was initiated in April 2020 in South Korea and focused on computational modelling of particle transport in the lung. The development of a lung particle deposition model forms the first half of the thesis (Chapters 2 to 4).

Chapter 2 reviews the existing literature on lung particle deposition modelling. Chapter 3 presents the development of the model. Chapter 3 forms a part of a published paper in Aerosol Science and Technology. The model was initially intended to evaluate the feasibility of microbubbles to target the small conducting airways for COPD/asthma treatment. However, an alternative approach to drug targeting in small conducting airways was proposed in Chapter 4, which investigates the use of controlled breathing parameters to target these airways. This chapter is currently under review in Pharmaceutical Research. The findings indicate that by controlling the tidal volume and flow rate, existing medical devices could achieve drug targeting in small conducting airways without the need for microbubbles.

The second half of the thesis examines potential applications. In particular, inhalable microbubbles have been identified as a promising solution for treating neonatal respiratory distress syndrome (nRDS). Currently, the administration of surfactant for nRDS treatment requires invasive measures, which can lead to severe complications for preterm babies. However, by inhaling lung surfactant at birth, the risks associated with intratracheal administration can be minimized, improving both short and long-term outcomes for preterm neonates. Unfortunately, conventional nebulized surfactants often fail to reach the lungs and instead deposit on the narrow airways in extrathoracic regions such as the nasal and throat. Additionally, high concentrations of animal-derived lung surfactant are typically needed to achieve sufficiently low surface tension in the lung airways.

Chapter 5 presents a literature review on nRDS and existing inhalable treatments. The review found that recent clinical trials of inhalable surfactants have failed due to insufficient material reaching the lung airways, resulting in a failure to achieve a therapeutically relevant reduction in surface tension in the air-lung fluid interface. The review also indicated that lung surfactants could have immunomodulatory effects against infections, preventing nRDS aggravation. Chapters 6, 7, and 8 present three studies exploring the potential of microbubbles in treating nRDS by improving lung penetration, surface tension reduction, and/or immunomodulation.

Chapter 6 compares the delivery efficiency of microbubble-laden aerosols to conventional aerosols in a 3D-printed preterm neonate upper airway model. In this study, the term "aerosols" refers to liquid droplets suspended in air. For example, microbubble-laden aerosols are aqueous droplets containing microbubbles. The 3D model was recreated from a CT scan of a 27-week gestational-old preterm neonate, and the study analysed the amount of dipalmitoylphosphatidylcholine (DPPC), a major component in lung surfactants, penetrating the model using HPLC. Chapter 7 studies the effectiveness of microbubbles in reducing air-lung fluid interface using a Langmuir-Blodgett Trough and compares it to a suspension of lung surfactants. Chapter 8 compares the immunomodulatory effect of microbubbles compared to lung surfactants using LPS-induced macrophage to represent a case of bacterial infection in preterm neonates.

Chapter 9 reviews the key findings and limitations of the thesis. Additionally, it outlines the potential areas of future research that need to be explored to enhance the efficacy of microbubble-based therapy for nRDS.

Chapter 2 Literature review on lung particle deposition model

2.1 Drug targeting in asthma and COPD

The small (peripheral) airways of the human lung were initially believed to be a ‘silent’ region because of their relatively low effect on the whole lung airflow resistance. In the last three decades, however, the small airways have been identified as a crucial region that determines disease progression. Small airways are defined as airways with inner diameters smaller than 2mm. The role of small airways in asthma was first confirmed in humans in 1992 [3]. Intrabronchial pressure measurements in the small airways revealed that these are the predominant obstruction sites [3]. Increased expression of inflammatory mediators such as IL-5 and IL-4 in asthmatic patients' small airways was found compared to healthy subjects [4]. Inflammation and obstruction in the small airways have been correlated with poor clinical outcomes, with inflammation in this region increasing the risk of severe asthma or even fatal asthma [5]. Inflammation in the small airways is now believed to be a cornerstone of asthma management, and non-invasive methods of assessment are becoming increasingly important.

Similarly, small conducting airways remained irrelevant in chronic obstructive pulmonary disease (COPD) management until a few decades ago but are receiving increasing attention in COPD management. However, the finding that closures of small conducting airways are responsible for emphysematous destruction and increased peripheral airway resistance [6], [7], [8] in COPD patients redirected the focus of the research, and this is now an active field in COPD management.

Small airways include tracheobronchial and acini airways (Figure 2.1), and the former is suspected to play a more significant role in airway obstruction than acini airways [9]. A modelling study found that poorly ventilated volume increases with airway constrictions in small tracheobronchial airways [9], and airway obstructions have been more often found in small tracheobronchial airways in micromanometer [3] and high-resolution CT imaging [10] studies.

Despite the importance of small airways, most inhaled therapies do not sufficiently reach this region [11]. A computational fluid dynamics (CFD) model has shown that coarse particles with a median mass aerodynamic diameter (MMAD) of 3μm deposit approximately 1 % of the total dose in the small tracheobronchial airways [12]. Extra-fine particle inhalers (<1.5 μm) have been shown to improve small airway obstruction and inflammation [13] and lead to increased quality of life [14]. Extra-fine particles may increase deposition in small tracheobronchial airways. Most particles, however, deposit in the acini region. To the best of the author’s knowledge, no commercially available inhalers target the small tracheobronchial airways, and hence, effective treatment for small tracheobronchial airway is still required.

2.2 Physiology of the lungs

The human lungs are an efficient gas exchange system that provides a large surface area (50-100 m^2) and a small diffusion length at the air-to-blood interface (0.2-0.5 μm) [15]. The other key components of the respiratory system are the muscles of the chest wall (e.g., diaphragm and intercostal muscles) and air-conducting pipes outside of the lungs (e.g., mouth, sinus, and larynx). Their primary role is to bring in fresh oxygen and remove carbon dioxide from the body.

Breathing begins with an expansion of the thoracic cavity. The contraction of the diaphragm and intercostal muscles pulls the rib cage upward and outward. The resulting increase in lung volume creates negative intrapleural and alveolar pressures and, hence, the inspiration of air through the tracheobronchial (conducting) airways (Figure 2.1) and into the acini (respiratory) airways [15].

The trachea is the first tracheobronchial airway that air encounters. To protect airways from collapsing due to high flow velocities, the walls of the trachea are supported by C-shaped cartilage rings. Similar structures are also found in the large bronchi but then change to plates in the smaller bronchi. In the bronchioles and alveoli ducts, where the flow velocity is much lower, the airways are surrounded by fibromuscular tissue. Consequently, they have greater elasticity and facilitate larger changes in volume and pressure during inhalation. Tissue elasticity is maximised in the alveoli, maximizing the surface area for the gas transfer [15].

Alveoli have several other features that facilitate an efficient and robust gas transfer. The first is a lining of pulmonary surfactant, which reduces surface tension and minimises the energy required to increase the lung volume during breathing. The second is the structure known as the pore of Kohn, which connects alveoli to one another and balances the difference in negative pressure between them. This prevents alveoli from collapsing [15].

Morphometry studies on the human lungs have facilitated understanding of their physiology. Specifically, they have allowed the modelling of airflow and air distribution in the lungs and helped to deduce the role of various tissues in the lungs and their role in obstructive airway diseases such as asthma and chronic obstructive pulmonary disease (COPD). The following literature review will describe how different studies have revealed the lungs' structure and will describe the various lung morphometry models that have been developed.

2.3 Lung morphometry

2.3.1 Tracheobronchial morphometry

The modern study of lung morphometry began with Weibel in 1962 [16] (Figure 2.1). Rubber casting of human lungs facilitated the measurement of morphometric characteristics of the human lung airways [16]. It suggested that the airways have 23 generations. A generation is a division point (or bifurcation) where one parent airway branches into two daughter airways. The trachea is Generation 0 by Weibel's definition [17], and the generation number increases by one at each bifurcation. Although the study focused on the respiratory region, it also provided useful insight into the diameter and lengths of tracheobronchial airways. The measurements led to the development of a 'single-path' model whose values are generation-averaged. It also revealed that the cross-sectional surface area of the airways increases with an increase in generation, and hence helped to reject a previous hypothesis that air resistance increases in deeper airways [18].

Further work from Weibel in 1963 [17] also provided important insights into lung physiology. Simulation of lung particle deposition, however, required other crucial information, specifically branching and gravity angles. The branching angle is the angle formed between two daughter branches at the bifurcation. The gravity angle is the angle between the airway and the direction of gravity. For example, the gravity angle would be 0 ° if it is parallel to the direction of gravity and 90 ° if it is perpendicular. Another rubber casting study [19] provided data on these measures and led to the development of many different models [20], [21], [22]. The first of these was a 'lobe-averaged' lung model [20]. The lungs have five lobes (two on the left and three on the right) that are separated by walls of tissue called fissures. Generation-averaged morphometric values (diameter, length, branching angle, and gravity angle) were given for each of the five lung lobes. This study facilitated whole-lung particle deposition simulations for each of the five lobes. This model, however, was not suitable for modelling the effect of variation in the airways (e.g. diameters, length, branching angle, gravity angle, and asymmetry in daughter airways) or allowing for any inter-subjective variability.

Inter-subject and airway variability were later introduced using statistical analysis [23]. This approach became the basis for a 'stochastic asymmetric' lung model [21] and a 'deterministic multiple-path' model [24]. The difference between the two models is that the stochastic asymmetric lung model creates an airway for each generation during particle deposition simulation, whereas the deterministic multiple-path model creates the whole lung and calculates deposition in each of the airways of the lungs. The multiple-path model allows for the analysis of deposition in different parts of the airways and an explanation of the differences in deposition in different lungs.

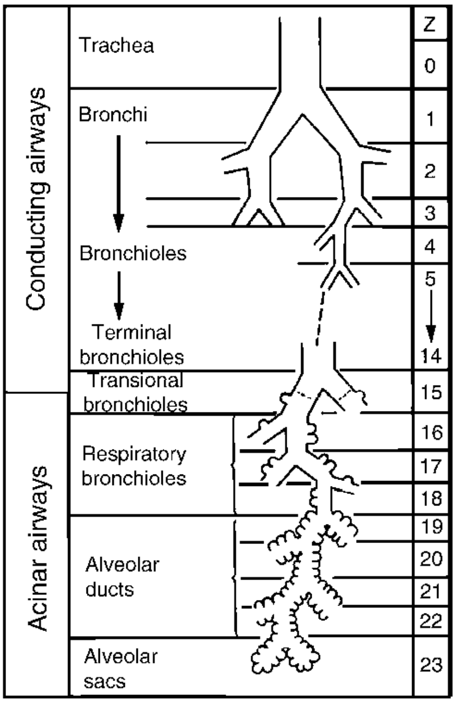

Figure 2.1. The figure describes the lung morphometry. Z represents airway generation, where the first airway (i.e., trachea) is Z = 0. The airway generation increases by one at each bifurcation. The lung has 23 generations on average, and it is primarily divided into two parts: conducting airways and the acinar (or respiratory) airways. Generation 8 and higher represent the small airways. Small is further divided into conducting small airways and small acinar airways. Adapted from 'Morphometry of the human lung', Springer, Vol.1 by Weibel et al., 1963.

Progress in X-ray computed tomography (CT) imaging [25] and magnetic resonance imaging (MRI) [26], [27] of the lung airways has facilitated the building of patient-specific lung airway models. High-resolution CT [25] imaging can identify and measure the morphometric characteristics of airways whose diameter is 3mm or larger and has successfully been applied up to Generation 9. The rest of the airways are recreated using measurements from rubber casting [17], [23], [28]. The patient-specific lung models show good agreement with the previous literature [29] in terms of number of acini, average generation number of terminal tracheobronchial airways, diameter, and length. This progress from population-averaged values using human plastic rubber casting to patient-specific airways using non-invasive CT and MRI imaging is paving the way for personalized medicine in inhaler treatment.

2.3.2 Acini morphometry

The acini comprise the respiratory region of the lungs, where the alveoli are located. Alveoli are tiny air sacs that allow efficient gas exchange between the air and the blood. Morphometry studies of the acini began with counting the total number of alveoli in the human lungs [16]. Weibel estimated that there are 300 million alveoli in the lungs [16]. The alveoli are distributed in different numbers in different generations. Weibel estimated that there are between 5 to 12 alveoli per duct in the three generations of respiratory bronchioles, increasing to 20 alveoli in the four generations of alveolar ducts and sacs [17]. Based on these estimations, Weibel [17] provided data on the diameter, length, and number of alveoli in the acini region. However, the number of acini measurements was insufficient because the material used for the casting could not penetrate through the narrow opening of the acini.

Improvement in casting techniques [19] facilitated more accurate acini measurement [30]. These revealed that there were up to 11 generations of acini airways, instead of 7 as suggested in Weibel's first model [17]. Weibel followed up on the original paper and showed there could be up to 12 generations of acini [31]. This led to a revision of Weibel's first model. In addition to average values for airway length and diameter for each generation and their corresponding distributions, the revised model also specified the volume distribution of acini, and the linear relationship between the number of alveoli sacs and the volume of acini ($R^2 = 0.99$). This information enabled randomised modelling to capture the effect of variability in acini morphometry [31].

There are discrepancies in the number of alveoli in the literature. The studies reported in references Schreider et al., 1981 [30], Haefeli-Bleuer & Weibel, 1988 [31], and Hansen & Ampaya, 1975 [32] estimated approximately 7100, 14200-17500, and 19800 alveoli per acini, respectively. Schreider et al., 1981 argued that their measurements were more accurate because they measured more samples (11 acini) than Hansen & Ampaya, 1975, which used a portion of an acinus. There was, however, a closer agreement between Hansen & Ampaya, 1975 and Haefeli-Bleuer & Weibel, 1988, and the latter was based on measurements of 5 acini. It was later confirmed that Hansen & Ampaya, 1975 and Haefeli-Bleuer & Weibel, 1988 had more accurate estimates of the number of alveoli when Ochs et al., 2004 [33] found that the total number of alveoli is ~480 million.

There are relatively few published data on human acini because of the difficulties associated with collecting data. Firstly, CT imaging and MRI cannot identify and measure acini airways because of their small size. Secondly, the casting of human lungs is tricky due to the lack of samples. An alternative approach is therefore to extrapolate from measurements of the tracheobronchial airways for gravity and branching angles [19], [23]. Whole lung models have been successfully developed on this basis for particle deposition studies [21], [22].

2.3.3 Summary of lung morphometric models

There are four different types of lung morphometry models. The first is a single or typical-path model, initially suggested by Weibel [17]. Average values of airway dimensions for each generation are used. The second type of model uses generation-averaged values for each of the lungs' five lobes [20], which captured the effects of morphometry differences in the lobes on deposition. The third type of model is the stochastic lung airway model [21], which captured the effect of inter-subject variability in the airways characteristics. The limitation of this method is that the whole lung is not modelled, and hence it is challenging to confirm agreement with literature values (e.g., number of alveoli, lung volume, number of acini, etc). This limitation is addressed by the fourth type of model [22], the deterministic multiple-path model, which captures inter-subject variability and airway variability. Therefore, the deterministic multiple-path method was selected for the rest of the studies in this thesis.

2.4 Lung particle deposition models

2.4.1 Numerical and analytical methods

Modelling lung particle deposition involves simulating particles' physical movement that is entrained in airflow inside the airways. The air carries the particles into the lungs, and the particles, while moving at a similar velocity, deposit in the lungs via impaction, sedimentation, and diffusion. The solution for particle transport can be either numerical (e.g., computational fluid dynamics, CFD) or analytical methods.

The main advantages of CFD are that it can be used to simulate flows in non-idealized (e.g., obstructed) airways and provide information on the effects of turbulence flow on particle deposition. It can also be used to study the effects of other mechanisms (such as electrostatic [34] and magnetic [35] attraction) on particle deposition. However, it is computationally intensive and therefore most useful for modelling small sections of the lungs, for example, a simulation in the whole-lung would take approximately 70 hours in a high-performance computer with 175 nodes[36]. Hence, comparison against in vivo data becomes difficult.

Analytical methods are much more computationally efficient, but they rely on simplified assumptions about the air flow and airway geometry. In particular, they assume that the air volumetric flow rate is proportional to distal volume (or the number of alveoli attached to the selected airway). Distal volume is defined as the 'lung volume distal to the proximal end of the airway' [24]. This assumption is acceptable in healthy lungs where the negative pressure gradient is the primary determinant of the volumetric flow rate. However, this assumption may not hold for air flow in obstructed airways, in which the radii of some airways are constricted. Consequently, these methods fail to capture pressure losses due to increased resistance in diseased airways. Other assumptions include particles having the same velocity as the air and airways having a cylindrical shape. Despite these assumptions, however, the analytical models have shown good agreement with in vivo particle deposition data in healthy human lungs [20], [21], [37]. Analytical methods also have the practical advantage that it can simulate a whole lung deposition in minutes compared to tens of hours for CFD.

Since the project's primary aim is to develop a novel inhaler, the aim of the in silico modelling was to evaluate the feasibility of using microbubbles to target specific regions whilst being independent of flow rate and lung morphology. Hence, it was decided that analytical models, which can simulate whole-lung deposition in a time-efficient manner, should be used for this part of the work.

2.4.2 Analytical particle deposition equations

As described above, particle deposition occurs by one of three processes: inertial impaction, sedimentation, and Brownian diffusion. Deposition by inertial impaction occurs at the airway bifurcation, where particles with considerable momentum cannot change direction in time and collide with the airway wall. Sedimentation and diffusion occur as particles travel through the airway. Sedimentation deposition is due to gravity and so is greater for heavier particles. Diffusion deposition depends on the particle size and is the primary deposition mechanism for particles smaller than 0.5µm in diameter [38]. This part of the literature review will cover the techniques that have been used to model these processes, including the use of empirical equations.

2.4.2.1 Inertial impaction

Inertial impaction problems are solved by calculating the relaxation time and stop distance of the particle in the bifurcating region and then solving them in the given geometry. Two of the most frequently used analytical approaches are Landhal, 1950 [39] and Cai and Yu, 1988 [40]. Landhal, 1950 [39] assumes that the curvature of bifurcating airways follows a circular path but the path of the particle, due to its inertia, will deviate from that of the airway path. This is illustrated in Figure 2.2A. r_c is the curvature radius for the particle, and r_0 is the curvature radius for the airway. At the end of the bending region, particles (r_c) would have deviated a certain distance (δ) from airway (r_0), i.e., $\delta = r_c - r_0$, and particles that were travelling at the top δ distance at the initial point of the bending region will deposit by the end of the bending region. This may be written as:

$$\delta = r_c - r_0 = \theta h \cdot St \qquad \text{Equation 2.1}$$

where θ is the bending angle in radians, h is the airway's diameter, and St is the Stokes number.

Considering the circular cross-section (Figure 2.2B) circle:

$$\varepsilon_i = \frac{A_{\text{shaded}}}{\pi R^2} = 1 - \frac{2}{\pi}\cos^{-1}(\theta\ \mathrm{St}) + \frac{1}{\pi}\sin\{2\cos^{-1}(\theta\ \mathrm{St})\} \qquad \text{Equation 2.2}$$

where θ is the bending angle in radians, ε_i is impaction deposition efficiency, and St is the Stokes number.

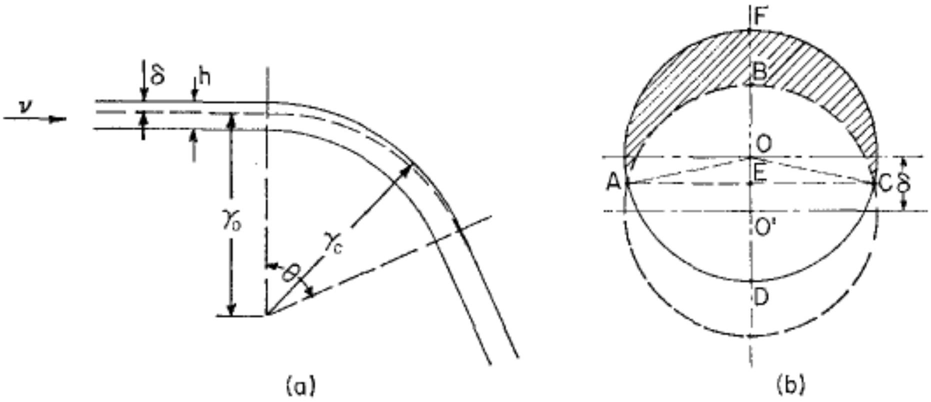

Figure 2.2. (A) represents the bending region at the branching point. Two horizontal lines on the left represent the parent airway walls, followed by the bending region and a daughter airway. The dotted line represents the particle trajectory. (B) shows two circles at the end of the bending region. The bottom circle is the airway's cross-sectional area. The top circle, which has moved up by δ, represents particles. The shaded area represented a fraction of deposited particles. Adapted from [41]. v is the air velocity, and h is the airway's diameter. r_0 and r_c are the curvature radius for the bending airway and the particle, respectively. δ is r_c- r_0.

Landhal, 1950 [39], assumes the same cross-sectional area and the same air velocity for the parent and daughter airways. Cai and Yu, 1988 [40] address this limitation by adding the effect of the ratio of parent and daughter airway diameter on air velocity and assuming that the flow is parabolic. The authors calculate the stop distance using the following equation:

$$s = Cv_p\tau(1 - e^{-1/\tau}) \qquad \text{Equation 2.3}$$

where C is the Cunningham slip factor, v_p is the particle velocity, τ is the relaxation time. The stop distance and the branching angle are used to solve for the fraction of area over which deposition occurs. Kim and Iglesia, 1989 [42] developed an empirical equation based on in vitro experiments under physiologically relevant conditions (e.g., 0.001-0.1 Stokes number). This approach did not incorporate the effect of bifurcation angle, and hence was not considered for the modelling in the present work.

2.4.2.2 Sedimentation

Sedimentation deposition, driven by the particle weight, occurs during the particle travel. Pich, 1972 [43] provides an equation for the sedimentation deposition efficiency in a rectangular and horizontal channel (Figure 2.3). The equation calculates the time over which particles travel through the airway (i.e., $t = {}^{L}/_{U}$), and then calculates the downward distance travelled during this time (i.e., $d = V_s \times \text{time}$). Therefore, particles at distance d from the bottom at the proximal end would have travelled downwards and deposited by the distal end (dotted line in Figure 2.3), and the deposition fraction may be represented as $\frac{d}{h}$.

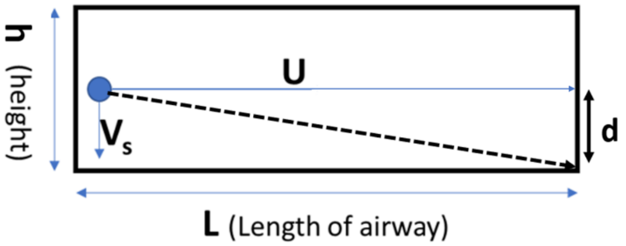

$$E = \frac{V_s L}{Uh} \qquad \text{Equation 2.4}$$

Figure 2.3. The figure represents 2-D rectangular and horizontal airway with L, and the height is h. The blue dot represents a particle with velocity, U, and settling velocity of V_s. E is the deposition fraction. d is the downward distance travelled by a particle from the entrance to the exit. The dotted black line represents the particle trajectory during its travel.

An improvement to equation (Equation 2.4) was made by changing the airway geometry from rectangular to cylindrical, again on a horizontal plane [43]. However, there remained the limitation that the effect of gravity angle (i.e., airway orientation in parallel to the direction of gravity) was not included. This was addressed by Wang, 1975 [44], which included the effect of gravity angle and introduced the concept of “retrieved particles”, i.e., particles that re-enter the parent airways.

Semi-empirical equations for sedimentation deposition have also been developed [45]. These equations incorporate the effect of gravity angle (φ), the orientation of airway (uphill/downhill), relaxation time (τ), and settling velocity (V) into a negative exponential term and calculate their effect on deposition probability:

For uphill flow,
$$\mathrm{P(S)} = 1 - \mathrm{e}^{-\frac{4\mathrm{g\,L\,\tau\cos\varphi}}{\pi \mathrm{D(U-V\sin\varphi)}}} \qquad \text{Equation 2.5}$$

For downhill flow,
$$\mathrm{P(S)} = 1 - \mathrm{e}^{-\frac{4\mathrm{g\,L\,\tau\cos\varphi}}{\pi \mathrm{D(U+V\sin\varphi)}}} \qquad \text{Equation 2.6}$$

where P(S) is sedimentation deposition probability, g is gravity, L is length of airway, φ is the gravity angle, D is diameter of airway, U is particle velocity along the airway and V is the settling velocity.

2.4.2.3 Diffusion

The diffusion equation is derived by solving the steady-state mass diffusion equation for a cylindrical airway [46]:

$$\mathrm{u_r}\frac{\partial \mathrm{c}}{\partial \mathrm{r}} + \mathrm{u_z}\frac{\partial \mathrm{c}}{\partial \mathrm{z}} = \mathrm{D}\left[\frac{1}{\mathrm{r}}\frac{\partial}{\partial \mathrm{r}}\left(\mathrm{r}\frac{\partial \mathrm{c}}{\partial \mathrm{r}}\right) + \frac{\partial^2 \mathrm{c}}{\partial \mathrm{z}^2}\right] + \mathrm{q} \qquad \text{Equation 2.7}$$

where c is the concentration of particles per unit volume, u is the average particle velocity by advection, D is the diffusion coefficient, and the q is the rate of formation of aerosols per unit volume of the flowing fluid. Particle position vectors in an airway are expressed in cylindrical coordinates, where r is the length of the vector on the airway cross-sectional plane and z is the length in the airway length direction. φ would have represented the angle of the vector on the cross-sectional plane, but particles are assumed to spread equally in all directions in this case, and hence it is not included.

Ingham, 1975 [46] assumes that no additional aerosols are formed (i.e., $q = 0$), and this is true for the current application. Movement of the particle in the direction z (or along airway length) by diffusion is negligible compared to their movement due to advection. Hence, $\frac{d^2c}{dz^2} = 0$. Airflow is assumed to have zero velocity in the cross-sectional plane, i.e., $u_r = 0$. u can be defined as $U(1 - \frac{r^2}{r_0^2})$ in Poiseuille flow, where U is the centreline velocity, and the r_0 is the radius of the airway. Equation 2.7 can be described as below:

$$U(1 - \frac{r^2}{r_0^2}) \frac{dc}{dz} = D\left[\frac{1}{r}\frac{d}{dr}\left(r\frac{dc}{dr}\right)\right] \quad \text{Equation 2.8}$$

Applying the boundary conditions $c = c_0$ at $z = 0$ for all r, and $c= 0$ at $r = r_0$ for $z > 0$ (i.e., the same concentration of particles enters at all points on its surface and particles deposit when they touch the airway wall), Equation 2.8 can be solved using a perturbation method [46], yielding:

$$P_D = 1 - 0.819e^{-14.63\Delta} - 0.0976e^{-89.22\Delta} - 0.0325e^{-228\Delta} - 0.0509e^{-125.9\Delta^{2/3}} \quad \text{Equation 2.9}$$

where $\Delta = \frac{DL}{4UR^2}$. D is the diffusion coefficient, L is the airway length, R is the airway radius, and U is the average centreline air velocity. The coefficients are taken from Nusselt (1910) for the first three terms [47], and the coefficients for the last term are derived empirically, as shown in Ingham, 1975 [46].

2.4.3 Comparison between numerical and analytical solutions

Zhang et al., 2009 [48] compared CFD simulations to analytical solutions in a healthy human lung model and showed a good agreement. Figure 2.4A describes deposition fraction in the tracheobronchial region, and it shows that the two models agree for particles with diameters in the range 1-10 μm. Figure 2.4B shows deposition fraction in each airway generation; it shows that the two models generally agree well, despite some differences in the higher generations. It suggests that the analytical model can simulate whole lung particle deposition in a time-efficient manner without compromising the accuracy of the result in the whole lung deposition.

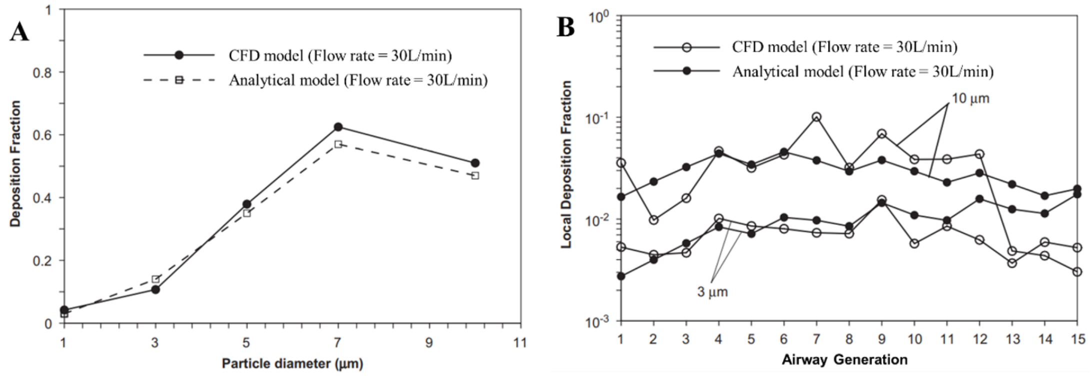

Figure 2.4. A) Comparison of inspiratory tracheobronchial deposition fractions between CFD simulations and analytical modelling at inhalation flow rate Q = 30 L/min, B) Comparison of bifurcation-by-bifurcation deposition fractions of micron particles during inspiration between CFD simulations and analytical modelling at inhalation flow rate Q = 30 L/min. Adapted from Zhang et al., 2009 [48].

2.4.4 in vivo lung particle deposition data

Lung particle deposition in humans can be studied using a range of methods. Pharmacokinetic methods measure pulmonary drug absorption while inhibiting oral absorption e.g., using charcoal-block [49]. Although pharmacokinetic studies can accurately measure systemic exposure of inhaler drugs, they are less helpful in measuring regional deposition. Estimation of deposition in the periphery (e.g., acini and small tracheobronchial) region can be made by measuring the maximum systemic drug concentration in the blood (C_{max}), and total systemic exposure to the drug (AUC_{∞}), but pharmacokinetic data are usually unreliable due to high inter-subject variability and insufficient sample sizes to compensate for this high variability [49]. Imaging techniques, such as 2-D gamma scintigraphy or single-photon emission computed tomography (SPECT), have also been used to study regional deposition in the lungs [50].

In 2-D gamma scintigraphy, the central region is defined as the 25% of the lung area in the centre, and the rest is assumed to be the periphery. The deposition region is quantified in terms of Penetration Index (P.I.) [50]. The P.I. is the ratio of particles entering the periphery (P) over the central (C) region of the lungs (P/C). SPECT divides the lung volume into ten compartments (or shells) and defines the first five compartments as central and the rest as peripheral [50]. However, the methods do not separate tracheobronchial airways from acini airways, and both central and periphery regions will have a mixture of tracheobronchial and acini airways. Hence, imaging alone does not provide a good estimation of tracheobronchial and acini particle deposition.

Estimating tracheobronchial particle deposition can be improved by taking into account the muco-ciliary mechanisms of large tracheobronchial airways. Large tracheobronchial airways clear particles within 24 hours [51], whereas small tracheobronchial airways and acini have a slower clearance rate due to shorter and less densely packed cilia [52]. Hence, particle deposition in the large tracheobronchial airways can be estimated by measuring radiation reduction in the lungs 24 hours after the initial deposition (radioactive decay is also taken into account).

SPECT has a higher spatial resolution than 2-D gamma scintigraphy and can describe the regional deposition in more detail (two vs 10 compartments). In addition, the progress in high-resolution CT (which can image airway dimensions) has facilitated particle deposition imaging in specific airways. These studies, however, have only been conducted on specific inhaler products or a small number of particle sizes under specific breathing conditions. In contrast, 2-D gamma scintigraphy has been widely used for decades and has been used to conduct human lung deposition studies with an extensive range of particle sizes and breathing conditions [53]. Hence, 2-D gamma scintigraphy in vivo human studies will be used for model validation in this study.

2.5 Conclusion

Simulation of particle deposition requires a lung airway model, an airflow model and a means of calculating particle deposition efficiency in the airways. The in silico model in the current project will create the upper tracheobronchial airways using CT-image measurements, and the rest of the airways will be created using the rubber casting data. The airflow and particle deposition model can be solved either numerically (CFD) or analytically. Since the aim of the in silico model is to evaluate the ability of microbubbles to target specific regions in the whole lungs, and not to facilitated detailed comparison with experimental data, analytical solutions will be used to predict lung particle deposition on account of their computational efficiency.

Chapter 3 Whole lung particle deposition model development

3.1 Introduction

In this chapter, we aim to create an in silico lung particle deposition model after reviewing relevant literature. Our model will be based on a deterministic 'multiple-path' lung that can account for inter-subject variability, allowing us to predict lung particle deposition with greater precision [54]. We will first develop a continuous administration model and evaluate its agreement with in vivo human data. Following this, we will create a bolus administration model accounting for the bolus dispersion.

3.2 Methodology

3.2.1 Deterministic multiple-path lung airway model

The tracheobronchial airway model used for the present work was based on a deterministic multiple-path lung model [54], [55]. The method is summarised in Figure 3.1. The development of high-resolution CT imaging has facilitated a non-invasive measurement of upper tracheobronchial airways. For example, Montesantos et al. (2013) measured tracheobronchial airway dimensions (e.g., diameter, length, and branching angle) in seven healthy subjects (n=7) [56]. For this study, upper tracheobronchial airway dimensions (Generation 1-7) were taken from Montesantos et al. (2013) [56] and gravity angles from Raabe et al. (1976) [57].

The airway diameter values from the high-resolution CT data were found to be lower than those of the human airway rubber casting. It was shown by Takahashi et al. (2011) that multi-detector CT underestimates the airway area by approximately 5% to 50% in airways with a diameter of 8mm or below [58]. Therefore, in order to match the airway diameters to the casting measurements, a scale factor of 1.075 was used here on the HR-CT for airways with diameters smaller than 6mm.

For Generations 8 to 21 of the tracheobronchial airways, data from Koblinger (1985) were used to create a deterministic multiple-path lung model (Figure 3.1) [59]. The cross-sectional area ratio between parent and daughter airways was randomly assigned from the reported average and its distribution in Koblinger (1985). The diameter ratio of the major and the minor daughter airways was similarly randomly selected from its reported distribution, and airway length was determined from the corresponding diameter-length correlation. Branching and gravity angles were randomly selected from their generation-averaged values from Raabe et al. (1976) and Koblinger (1985) [57], [59]. Lastly, the termination of the airways was determined from the termination probability equation given by Koblinger (1985). The process was repeated until all tracheobronchial airways terminated.

The branching angle values were taken from Raabe et al. (1976) and Koblinger (1985) [57], [59]. For Generations 20 and 21, the cumulative distribution function of Generation 19 was used because of the lack of available data. For the gravity angle, data from Raabe et al. (1976) were used for airways up to Generation 13 for each of the corresponding airway generations. Due to low sample numbers for airways in Generation 14 or above, measurements from all generations were pooled, and the resulting average and standard deviation values were used for Generation 14 and higher.

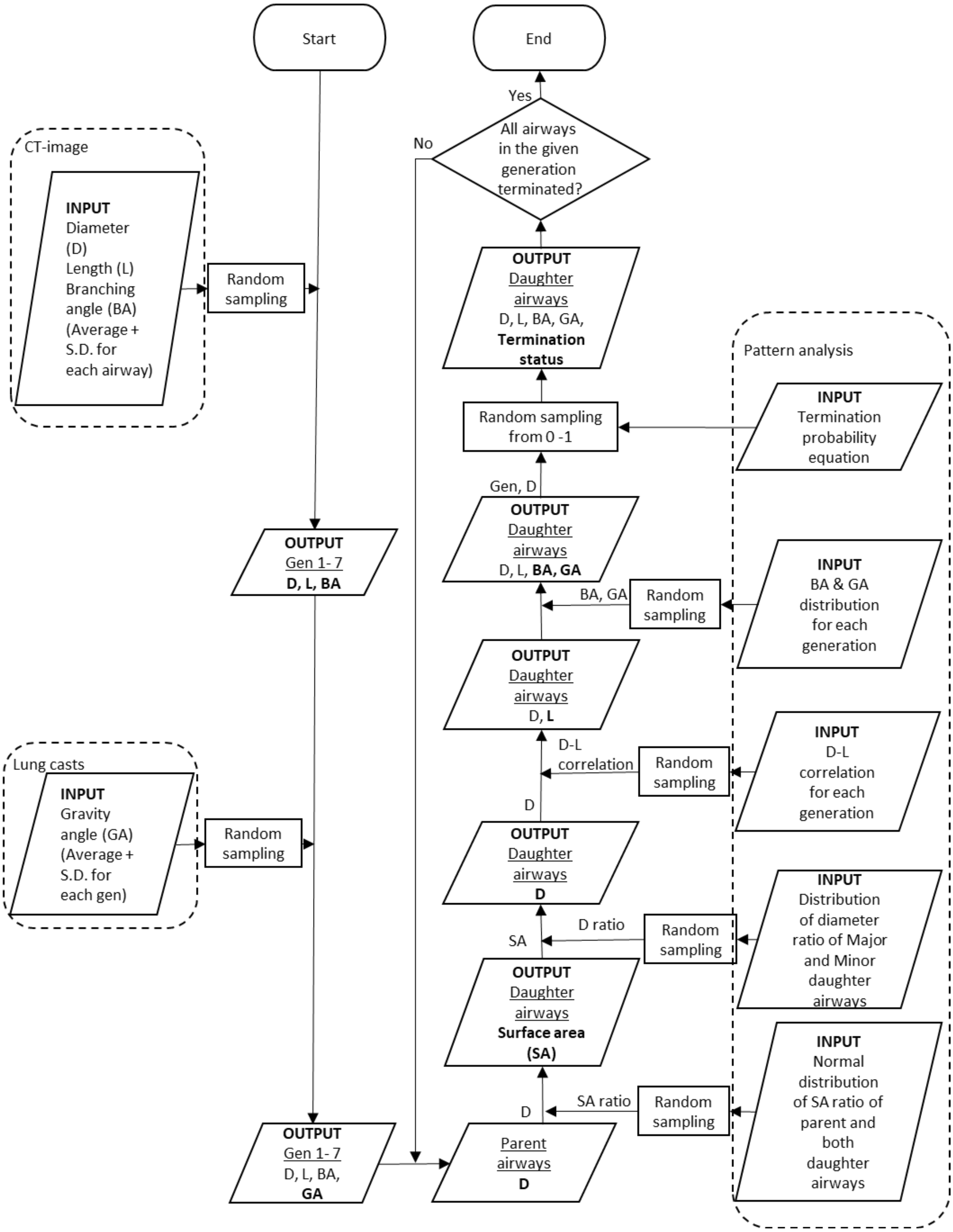

Figure 3.1. Summary of the method used to create the tracheobronchial model. The left-hand side of the flow chart corresponds to Generations 1 to 7, and the right-hand to Generations 8 to 21. CT-image measurements were from Montesantos et al. (2013) [56]. Lung cast measurements were taken from Raabe et al. (1976) [57]. Pattern analysis was from Koblinger (1985) [60]. INPUT refers to lung characteristic data from the literature. Bold formatted terms inside OUTPUT boxes represent characteristic values assigned at that step. MATLAB (2020b, MathWorks, Inc.) software was used to implement the method.

The method of modelling the acini airways is summarised in Figure 3.2. Each airway was assigned a diameter and length from Haefeli-Bleuer & Weibel (1988) [61]. Branching and gravity angle values were taken from Raabe et al. (1976) [57]. Since a terminal airway number distribution was not given, it was calculated indirectly from the reported acini volume distribution, and a linear relationship was assumed between the number of sacs and acini volume following Haefeli-Bleuer & Weibel (1988) of the form:

$$\text{Number of terminal airways} = 13.6 + 2.33 \times \text{Volume of acini (mL)}\ (\mathrm{r} = 0.99) \qquad \text{Equation 3.1}$$

The volume of each acinus was randomly selected from the distribution, and the equation above was then used to calculate the number of terminal airways. The number of terminal airways, in turn, decided the number of airways and terminal airway generation in each acinus.

Airway characteristics (i.e., length, diameter, gravity angle, and branching angle) were randomly assigned. Length and diameter were taken from Haefeli-Bleuer & Weibel (1988) [61]. As before, the gravity angle data were pooled from Raabe et al. (1976), and the average and standard deviation were calculated [57]. The angle for each airway was randomly selected from the corresponding normal distribution. Similarly, for the branching angle, the cumulative distribution function of Generation 19 of the tracheobronchial airways was again used. The average number of alveoli for each generation was taken from Weibel (1963) [62]. Ten thousand model acini were simulated, and one of them was randomly selected to be attached to each terminal bronchiole.

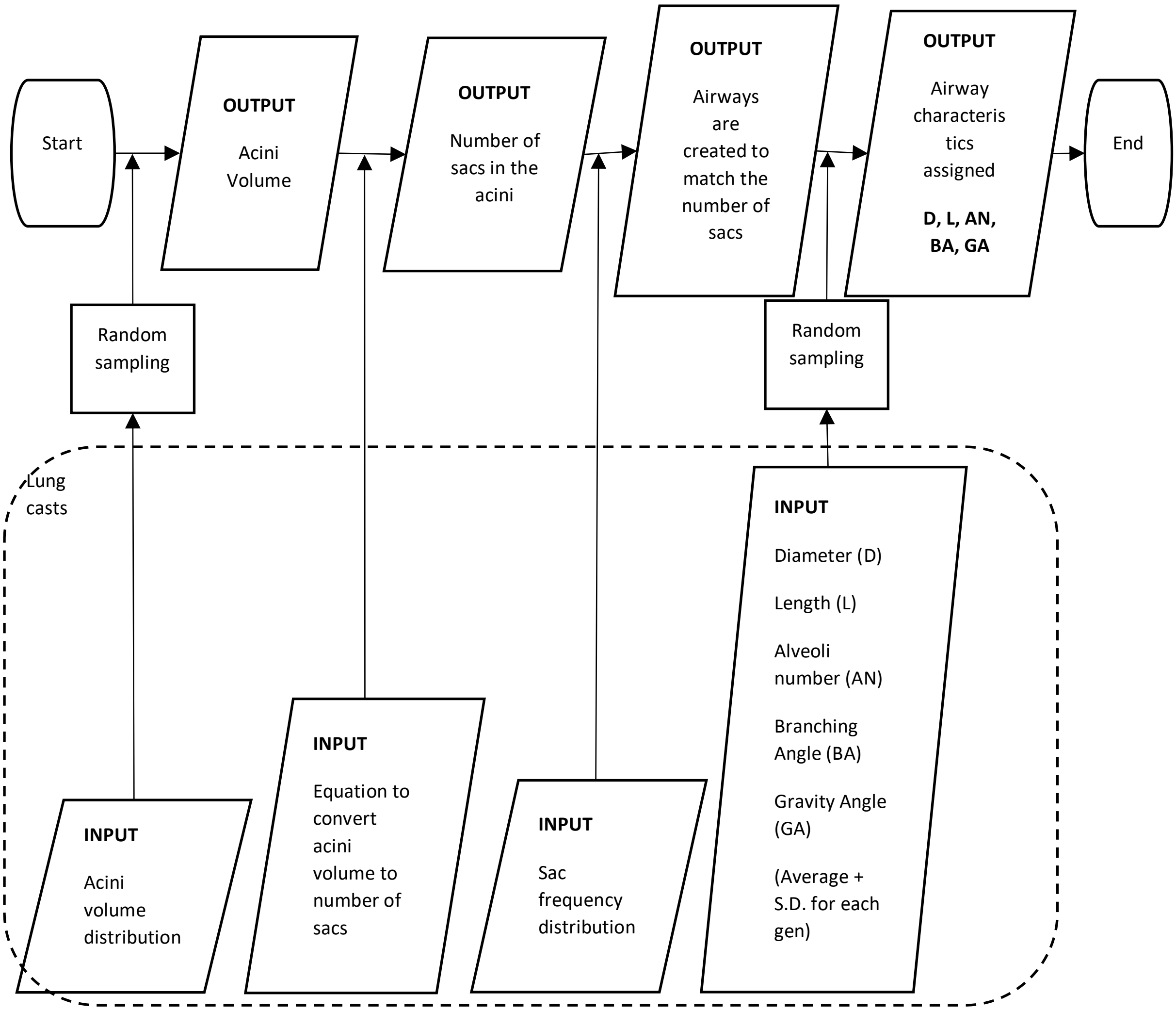

Figure 3.2. A summary of the four steps of acini airway modelling. INPUT refers to lung characteristic data from the literature. Gravity angle and branching angle data were taken from Raabe et al. (1976) [57], and the rest of the data from Haefeli-Bleuer & Weibel (1988) [61]. Bold formatted terms inside OUTPUT boxes represent characteristic values assigned at that step. MATLAB (2020b, MathWorks, Inc.) software was used to implement the method.

3.2.2 Particle deposition model for continuous administration & selecting analytic equations for deposition efficiency calculation

It was assumed that no particles were present in the lungs prior to inhalation. Particles were assumed to be spherical and have a smooth and rigid surface and unit density. Airway walls were assumed to be rigid, and particle depositions were assumed upon contact. A steady flow rate and constant initial concentration were also assumed so that the particle concentration in the airway does not change as a function of time. Hence, constant concentration enters and exits each airway during inhalation. This may be written as:

$$C_{inh}^{k,0}(t) = \begin{cases} 0, & t < t_{inh}^{par(k)} \\ C_{inh}^{k,0}, & t \geq t_{inh}^{par(k)} \end{cases} \qquad \text{Equation 3.2}$$

where C is the particle concentration, t is time, k is the selected airway, 0 represent the proximal end of the airway, $t_{inh}^{par(k)}$ represents the time required for air to cross the parent airway. The particle concentration is expressed as the mass of material per unit volume of air.

Particle deposition was assumed to begin soon as the particles exit each parent airway and enter a bifurcating region. At the bifurcation, impaction deposition dominates. The remaining undeposited particles then enter the daughter airways, where deposition by sedimentation and diffusion takes place. The deposition efficiencies for impaction (ε_i), sedimentation (ε_s), and diffusion (ε_d) for each airway are calculated using analytical equations. This may be written as:

$$C_{inh}^{k,0} = C_{inh}^{par(k),1}\left(1 - \varepsilon_i^k\right) \qquad \text{Equation 3.3}$$

$$C_{inh}^{k,1} = C_{inh}^{k,0}\,(1 - \varepsilon_s^k)(1 - \varepsilon_d^k) \qquad \text{Equation 3.4}$$

C is the concentration, 0 is the proximal end, 1 is the distal end, and k is the airway. Once the concentration was obtained, the deposited mass was calculated using the principle of mass balance:

$$m_{dep}^k = m_{in}^k - m_{out}^k - m_{rem}^k \qquad \text{Equation 3.5}$$

where *dep* refers to the deposited mass, *in* and *out* refer to mass entering and exiting the airway, and *rem* refers to the mass that is remaining. Mass entering and exiting the airway is given by:

$$m_{in}^k = \int_0^{T_{inh}} F^{k,0}\, C_{inh}^{par(k),1}(t)dt = C_{inh}^{par(k),1}\left(T_{inh} - t_{inh}^{par(k)}\right)F^{k,0} \qquad \text{Equation 3.6}$$

$$m_{out}^{k} = \int_{0}^{T_{inh}} F^{k,1}\, C_{inh}^{(k),1}(t)dt = C_{inh}^{k,1}\left(T_{inh} - t_{inh}^{k}\right)F^{k,1} \qquad \text{Equation 3.7}$$

F is the volumetric flow, C is the concentration, k is the airway, *par(k)* is the parent airway, 0 and 1 are proximal and distal ends, and t_{inh} is the time taken for particle-laden air to cross the airway. To calculate the mass remaining in the airway at the end of inspiration, a linear function was used to calculate the average concentration in the airway, i.e., ., $C_{inh}^{k,average} = (C_{inh}^{k,0} + C_{inh}^{k,1})/2$. The mass remaining was calculated by multiplying the average concentration and the airway volume.

$$m_{rem}^{k} = A^{k} \int_{0}^{L^{k}} C_{inh}^{(k),1}\,(x)dx \approx C_{inh}^{k,average}\, L^{k}A^{k} \qquad \text{Equation 3.8}$$

For particle deposition during exhalation, the deposited mass was calculated directly from the total mass entering the airway. In other words, the deposited mass was essentially equal to the total mass that entered the airway multiplied by the deposition efficiency. Deposition in each airway was calculated as follows:

$$m_{in}^{k} = m_{out}^{d1} + m_{out}^{d2} \qquad \text{Equation 3.9}$$

$$m_{out}^{k} = (1 - \varepsilon_{sd})m_{in}^{k} + (1 - \frac{\varepsilon_{sd}}{2})m_{rem}^{k} \qquad \text{Equation 3.10}$$

$$m_{dep}^{k} = m_{rem}^{k} + m_{in}^{k} - m_{out}^{k} \qquad \text{Equation 3.11}$$

where m is the mass, $d1$ and d_2 are daughter airways of k. Deposition efficiency for the remaining particles is halved because no particle deposition occurs for particles at the proximal end of each airway. This is because they exit the airway as soon as exhalation begins. Deposition efficiency is assumed to reduce linearly from the distal to the proximal end of each airway, and the deposition efficiency for the remaining particles (m_{rem}^{k}), therefore, is $\varepsilon_{sd}/2$.

The different sets of analytical equations are summarised in Table 3.1. Two impaction equations were considered: Landahl (1950) [63] and Cai & Yu (1988) [64]. Cai & Yu (1988) included the effect of differences in parent and daughter airway diameter on deposition, whereas Landahl (1950) did not. Two sedimentation equations were also compared: Wang (1975) [65] and Beeckmans (1965) [66]. Beeckmans (1965) developed a semi-empirical equation, and Wang (1975) developed an analytical solution for deposition in inclining and declining cylindrical airway geometries. The diffusion equation was taken from Ingham (1975) [67].

The analytical model was next compared to in vivo human particle deposition data [68]. The results for large tracheobronchial deposition were compared against the particle fraction that cleared within 24 hours in the selected in vivo study [68] because large tracheobronchial airways are predominantly responsible for fast clearance (< 24 hours). In vivo acini deposition, which is the number of particles remaining in the lungs after 24 hours, can thus be assumed to be equivalent to small tracheobronchial and acini deposition. The lung particle deposition modelling was implemented using MATLAB (2020b, MathWorks, Inc.) software.

Mechanism of deposition	Sets of analytical equations			
	Method 1	Method 2	Method 3	Method 4
Impaction	Cai & Yu (1988)	Landahl (1950)	Cai & Yu (1988)	Landahl (1950)
Sedimentation	Wang (1975)	Wang (1975)	Beeckmans (1965)	Beeckmans (1965)
Diffusion	Ingham (1975)	Ingham (1975)	Ingham (1975)	Ingham (1975)

Table 3.1. Four different methods for deposition modelling were created from a combination of two impaction, two sedimentation and one diffusion equations. References for the equations are as follows: *Landahl (1950)* [63], *Cai & Yu (1988)* [64], *Wang (1975)* [65], *Beeckmans (1965)* [66], *and Ingham (1975)* [67].

3.2.3 Bolus administration model development

Bolus dispersion was modelled using the method from Hofmann et al., 2008 [69]. The model includes the effect of (1) mixing in the extrathoracic region, (2) convective mixing in conducting airways, (3) mixing at airway bifurcations, and (4) mixing of residual and new air in the alveoli. The model with bolus dispersion was then validated against in vivo data [70].

For the modelling of bolus administration, it was assumed that the total mass of particles enters the lungs at the initial inhalation point and that no particles are left behind in an airway if the volume of air in which they are suspended has left that airway. It was assumed that the bolus dispersion effect is a result of the air that the particles are entrained in, and thus, the assumption (i.e., if the volume of air has left the airway, the particles have also left the airway) still holds. It was also assumed that there was no particle-particle interaction. At each bifurcation, the particles were partitioned in proportion to the ratio of the distal volume of one daughter airway and that of both daughter airways, giving:

$$m_{in}^{k,1} = m_{out}^{p(k)} \times DV^{k,1}/(DV^{k,1} + DV^{k,2}) \qquad \text{Equation 3.12}$$

$$m_{out}^{k} = m_{in}^{k}(1 - \varepsilon_i)\,(1 - \varepsilon_s)\,(1 - \varepsilon_d) \qquad \text{Equation 3.13}$$

$$m_{dep}^{k} = m_{in}^{k} - m_{out}^{k} - m_{rem}^{k} \qquad \text{Equation 3.14}$$

where m is the particle mass, k is the airway, 1 is the major daughter airway, 2 is the minor daughter airway, $p(k)$ is the parent airway, and ε is deposition efficiency for i (impaction), s (sedimentation), and d (diffusion). m_{rem} is the remaining particles in the airway. m_{in} is particles entering the airway. m_{out} is particles leaving the airway. DV is the distal volume of the airway. The bolus model was compared to the continuous model to study the effect of administration mode on particle travel and deposition in the lungs.

3.3 Results and discussion

3.3.1 Deterministic multiple-path lung airway model

Results from the whole lung model were first evaluated against those from other lung models and experimental data. Figure 3.3 compares the average diameter and length values to literature values. Weibel (1963) [62] and Phalen et al. (1985) [71] used measurements from different human lung casts, and Montaudon et al. (2007) [72] used measurements of multi-detector computed tomography (MDCT). Figure 3.3 shows that there is good agreement between the model and the literature values, with discrepancies being within the standard deviation for most generations. The discrepancy in airway diameter between the model and Montaudon et al. (2007) in the 11th to 14th generations is likely to be due to the resolution limit of MDCT, which creates a bias for larger airways.

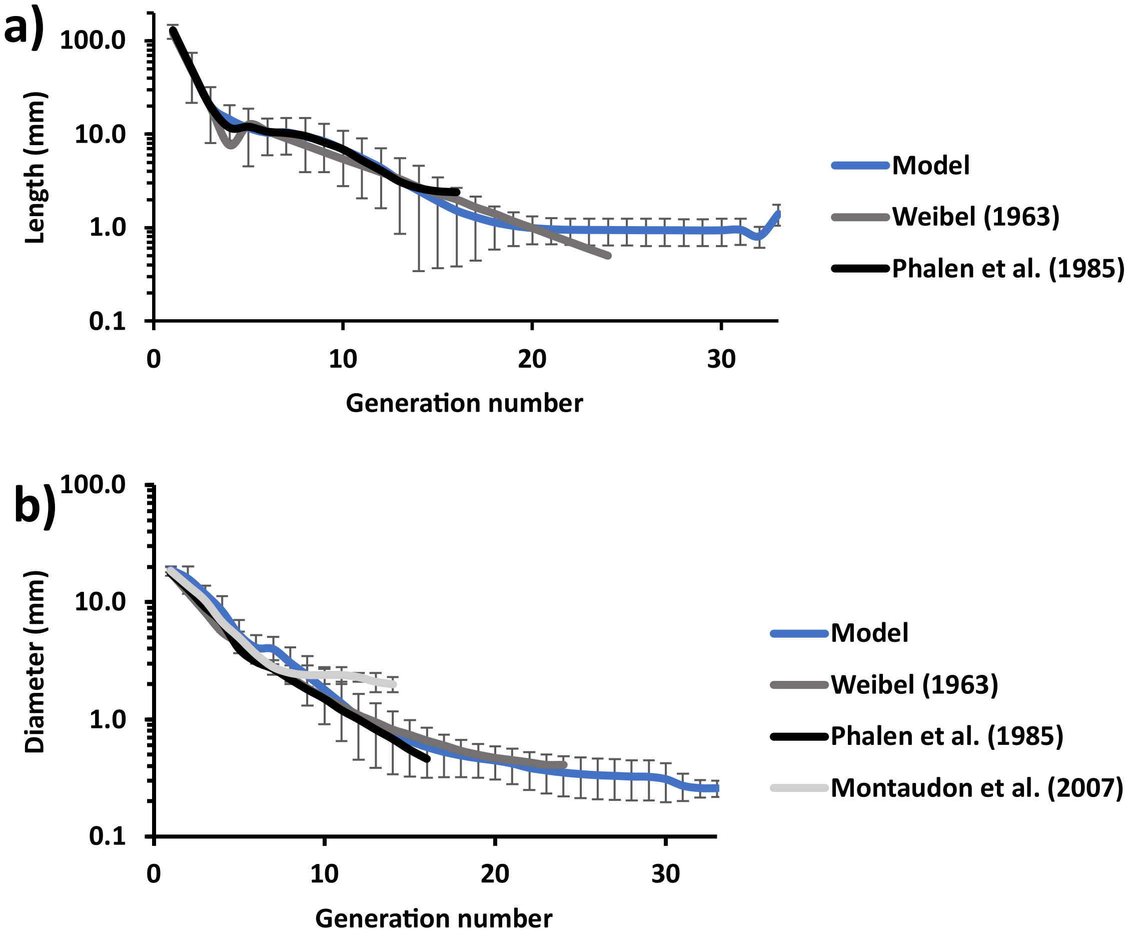

Figure 3.3. Average airway a) length and b) diameter of each generation for the current model (n=100, blue), the models of Weibel (1963) (grey), and the measurements of Phalen et al. (1985) (black). CT measurements from Montaudon et al. (2007) [72] are included for the diameter. The standard deviation is shown for the current model and Montaudon et al. (2007) by the black lines.

The branching angle values were also compared to those from another lung model (Phalen et al., 1985) (Figure 3.4). The two datasets that were used to make the model are also included in the figure for reference [56],[57]. No literature was found that included data for branching angle in the acini airways, and hence, only tracheobronchial airway values could be compared. The current model is in agreement with Otto et al. (1976) [57] for Gen 2-7 and Montesantos et al. (2013) [56] for Gen 8-14. From G15 to the terminal airway, the average branching angle remained constant. This is because the average of all branching angle measurements was used. Nevertheless, the large standard deviation still provides inter-airway and inter-subject variability. The model also showed reasonable agreement with the data from Phalen et al. (1985) [71], with most discrepancies remaining within one standard deviation.

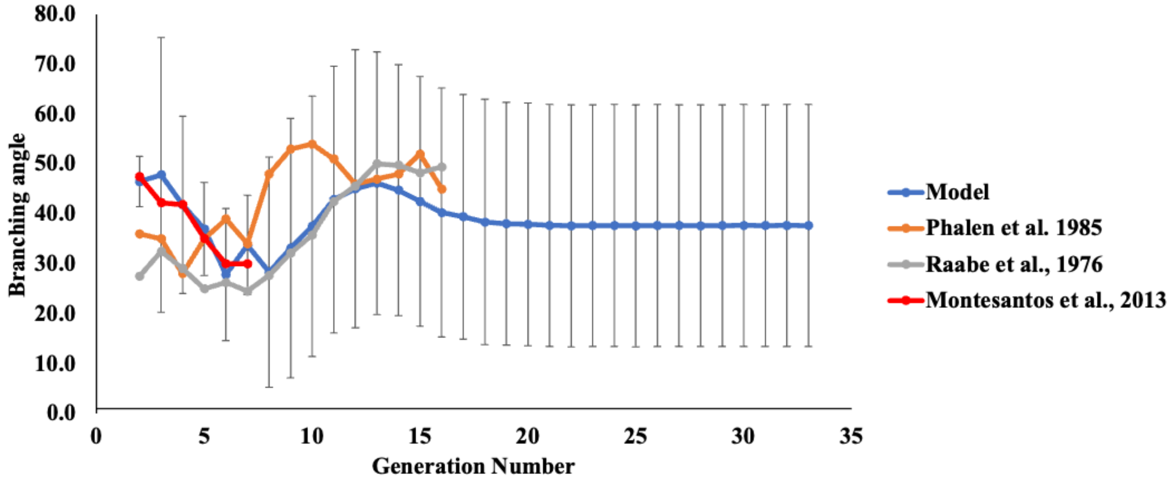

Figure 3.4. Average branching angle per generation for the current model (blue), Phalen et al. (1985) (orange), Raabe et al., (1976) (light grey), and Montesantos et al. (2013) (red). The standard deviation was calculated for the current model and is displayed in black limited lines. The y-axis shows branching angles, and the x-axis is the generation number.

The gravity angle values from the model were compared to the data that were used to create the model (Figure 3.5) because no other experimental data were available. The model showed good agreement with the dataset in all generations.

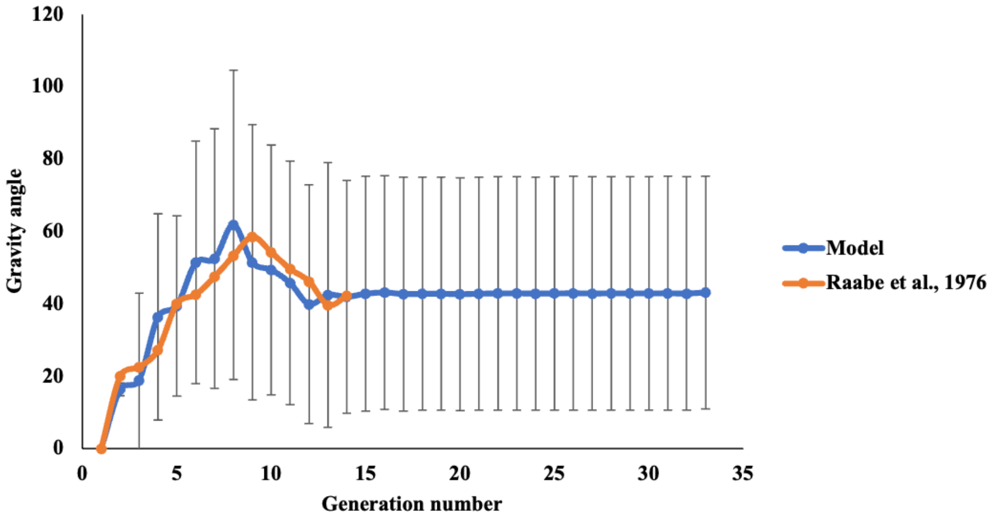

Figure 3.5. Average gravity angle for the current model (blue) and the dataset from Raabe et al. (1976) (orange). The standard deviation was obtained for the current model and is displayed by the black limited lines. y-axis shows the gravity angle, and the x-axis is the generation number.

The whole lung characteristics of the current model were compared to those from other lung models and experimental values (Table 3.2). The average number of acini, which reflects the total lung size, agreed well with other lung models. Generation numbers for terminal bronchioles and airways agreed with Hofmann et al. (2002) but were higher than earlier literature values (Weibel, 1963 and Yeh & Schum, 1980). One reason for this may be the development in the understanding of acini morphometry. Haefeli-Bleuer & Weibel (1988) found that there were, on average, 9 generations of acini instead of 7 as found by Weibel (1963). A second reason may be the lack of variability in terminal airway generation numbers in Weibel (1963) and Yeh & Schum (1980), which used a typical-path model as opposed to the multiple-path model used in the current model. The whole-lung characteristics (e.g., the total number of alveoli and total lung capacity) were also compared to the experimental values from the literature, there was found to be good agreement.

This study used a deterministic multiple-path lung airway model based on Asgharian et al. (2001) [54] to capture the variability in particle deposition due to variability in lung airway geometry. Asgharian et al. (2001) model could not accurately capture the average values and standard deviations in the upper airways due to a lack of lung samples (n=2) [54], [57], [73]. Variability in the upper airways is a particularly important factor because it results in large differences in particle deposition [74]. This issue was resolved in the present study by using imaging data from more human subjects (n=7) [56], [74]. This has enabled good agreement with both other lung airway models and experimental literature values.

Characteristics	Lung model (n = 100)	Reference value	Reference
Average number of acini	26402 (±3179)	26449 29240 27706 29445 23000 34856 (±11079) 32768	Yeh & Schum (1980) Horsfield et al., (1971) Kitaoka et al., (1999) Tawhai et al., (2000) Florens et al., (2011) Hofmann et al., (2002) Weibel (1963)
Average generation number of terminating bronchioles	17.7 (±0.25)	16 17.6 15	Yeh & Schum (1980) Hofmann et al., (2002) Weibel (1963)
Average generation number of terminating acini airways	27.6 (±0.25)	25 28 23	Yeh & Schum (1980) Hofmann et al., (2002) Weibel (1963)
Total number of alveoli	4.69×10^8 ($\pm 0.56 \times 10^8$)	4.80×10^8	Ochs et al., (2004)
Total lung capacity (mL)	5742 (±708)	approx. 6000mL	Delgado & Bajaj (2020)

Table 3.2. Comparing the current lung model to literature values for the average number of terminating bronchioles, the average generation number of terminating bronchioles and airways, the average number of alveoli, and average total lung capacity. Values in brackets are the standard deviation. The sample size for the current model is 100. References are as follows: Yeh & Schum (1980) [75], Horsfield et al., (1971)[76], Kitaoka et al., (1999) [77], Tawhai et al., (2000) [78], [79], Florens et al., (2011) [79], Hofmann et al., (2002) [80], Weibel (1963) [62], Ochs et al., (2004) [81], and Delgado & Bajaj (2020) [82].

3.3.2 Particle deposition model for continuous administration

Particle deposition fractions were calculated for particle diameters from 0.1 to 10 μm for both the whole lung and specific regions. The models were compared to in vivo data for three different breathing conditions: tidal volume (TV) = 1500mL and breathing frequency (BF) = 15/min (Figure 3.6), TV = 1000mL & BF = 7.5/min (Figure 3.7), TV = 500mL & BF = 15/min (Figure 3.8).

The figures below compare the results from the four methods described in Table 3.3. The four methods were found to have similar total and extrathoracic (ET) deposition, but there were differences found for the bronchial and acini regions (Table 3.3). For bronchial deposition, the impaction equation from Landahl (1950) [63] (Methods 2 and 4) showed better agreement with the experimental data than the equation from Cai & Yu (1988) [64] (Methods 1 and 3). Changing the sedimentation equation, however, had minimal effect on bronchial deposition predictions. For acini deposition, the four methods started to show differences from 2-10μm (Figure 3.6). For 2-3μm diameter particles, the semi-empirical sedimentation equation from Beeckmans (1965) [66] (Method 3 and 4) showed better agreement than Wang (1975) [65] (Method 1 and 2) with the experimental data. However, Cai & Yu (1988) impaction equation (Methods 1 and 3) showed better agreement for 6-10μm diameter particles.

Table 3.3 presents the average differences in deposition fraction between the methods and in vivo data (Heyder et al., 1986 [68]). Methods 2 and 4 showed the least difference in bronchial deposition, whilst Methods 1 and 3 showed better agreement in acini deposition. Method 4 showed the best agreement overall with the in vivo data. It was, therefore, selected for the subsequent modelling.

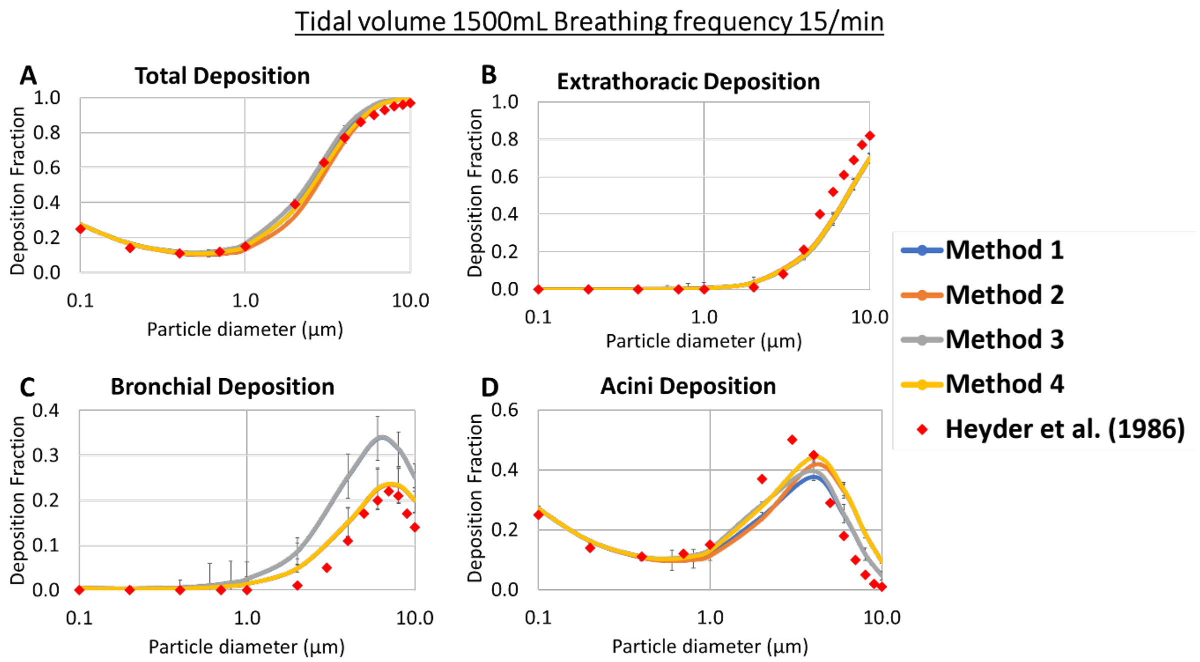

Figure 3.6. Effect of particle size upon total and regional deposition. Results from the model (n=3) are compared to in vivo data (n=3) [68].TV = 1500mL & BF =15/min. A) total deposition, B) extrathoracic deposition, C) bronchial deposition, D) acini deposition.

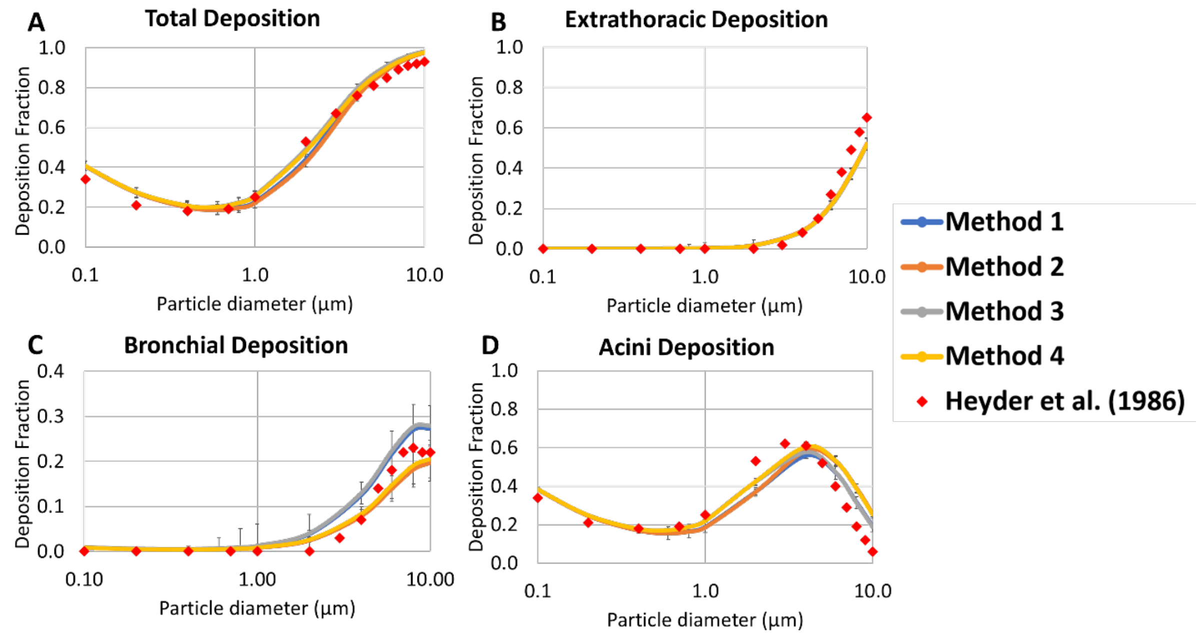

Figure 3.7. Effect of particle size upon total and regional deposition. Results from the model (n=3) were compared to in vivo data (n=3) [68]. TV = 1000mL & BF =7.5/min. A) total deposition, B) extrathoracic deposition, C) bronchial deposition, D) acini deposition.

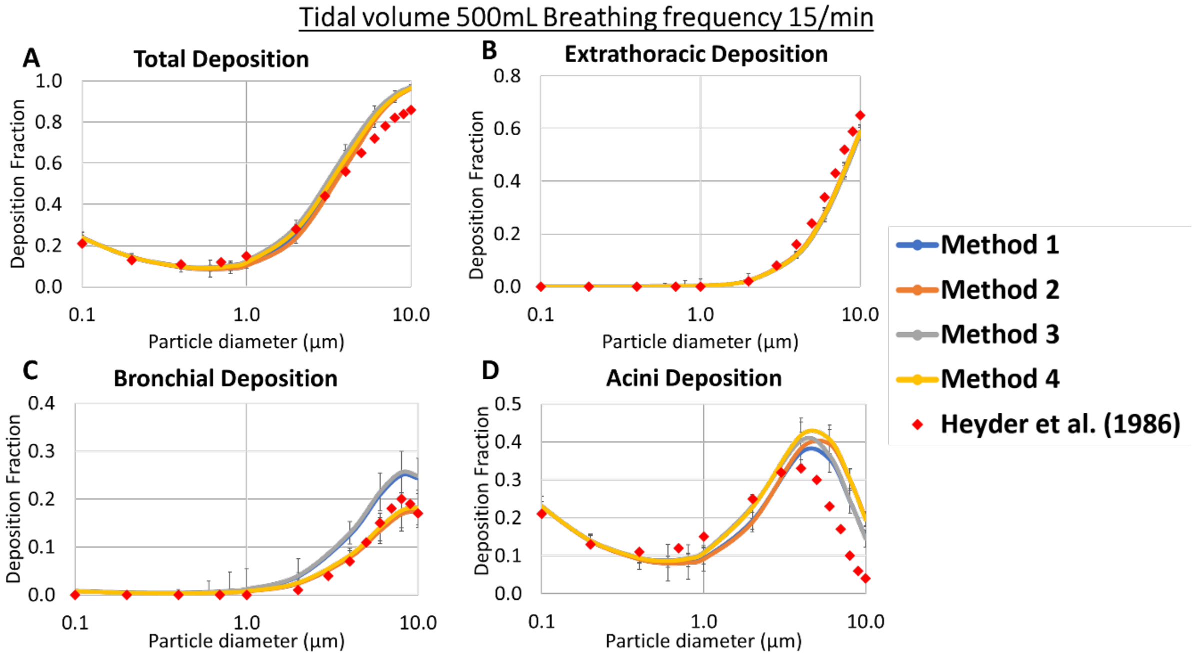

Figure 3.8. Effect of particle size upon total and regional deposition. Results from the model (n=3) were compared to in vivo data (n=3) [68]. TV = 500mL & BF =15/min. A) total deposition, B) extrathoracic deposition, C) bronchial deposition, D) acini deposition.

A) Bronchial deposition	Average difference between model and *in vivo* data			
*Breathi*ng conditions	Method 1	Method 2	Method 3	Method 4
Tidal Volume 500mL & BF 15	0.033	0.011	0.035	0.011
Tidal Volume 1000mL & BF 7.5	0.028	0.019	0.031	0.017
Tidal Volume 1500mL & BF 15	0.068	0.023	0.068	0.024
Average difference	0.043	**0.018**	0.045	**0.017**

B) Acini deposition	Average difference between model and *in vivo* data			
*Breathi*ng conditions	Method 1	Method 2	Method 3	Method 4
Tidal Volume 500mL & BF 15	0.065	0.083	0.063	0.082
Tidal Volume 1000mL & BF 7.5	0.077	0.096	0.064	0.083
Tidal Volume 1500mL & BF 15	0.050	0.069	0.042	0.060
Average difference	**0.064**	0.083	**0.056**	0.075

C) Bronchial + acini	Method 1	Method 2	Method 3	Method 4
Average	0.054	0.051	0.051	**0.046**

Table 3.3. Average difference in A) bronchial and B) acini deposition fraction between the model and in vivo for particle diameters from 0.1 to 10 µm (n=15). The last row shows the average of the three breathing conditions. C) calculates average differences in bronchial and acini. Bold text denotes method(s) with the best agreement with the in vivo data.

3.3.3 Particle deposition model for bolus administration

The bolus model predicted higher total and acini deposition than the continuous administration model, but bronchial and extrathoracic depositions were not statistically significantly different ($p > 0.05$) (Figure 3.9). The differences in predicted deposition can be explained by the difference in particle fraction entering deeper generations (Figure 3.10). Bolus administration delivers the total particle mass at the start of inhalation, and continuous administration delivers particles throughout inhalation. More particles can, therefore, reach the deeper airways of the former. This is illustrated in Figure 3.10A, which shows the particle fraction entering each airway generation. It shows that similar fractions of the emitted dose enter the lower generations for both administration methods, but as the air approaches the higher generations, fewer particles reach the deeper airways. Figure 3.10B shows that the increased number of particles entering an airway increases the deposition fraction.

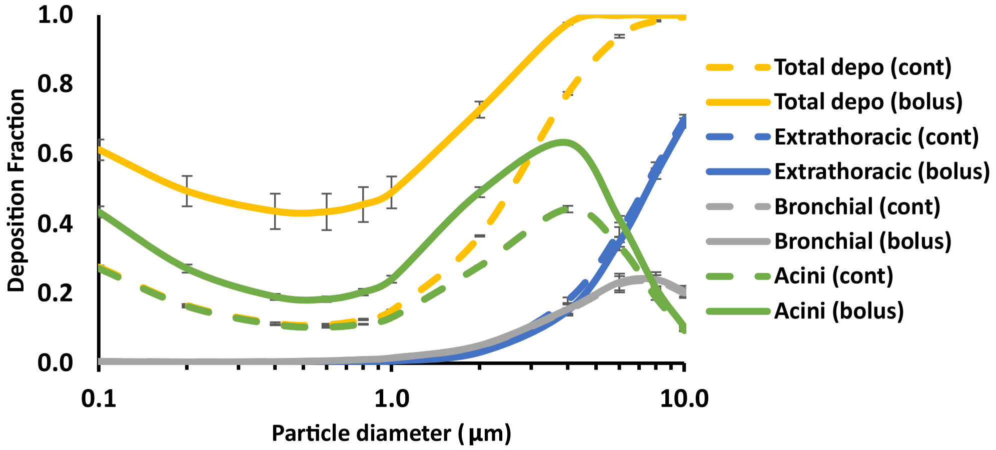

Figure 3.9. Comparison of the predicted deposition fraction for bolus (solid line) (n=3) and continuous (dashed line) (n=3) administration. Tidal volume = 1500mL, breathing frequency = 15/min. Particles were assumed to be spherical, rigid, smooth and to have a unit density (1g/mL). The black lines represent 1 standard deviation.

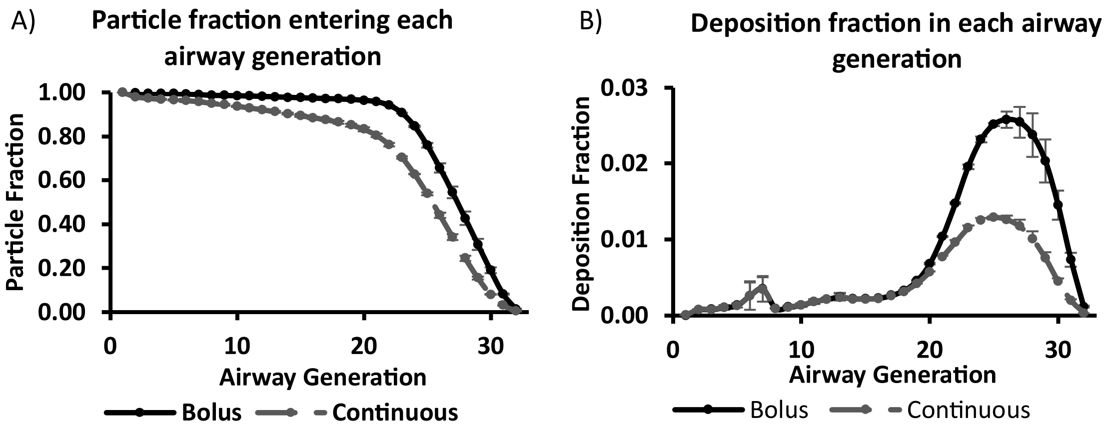

Figure 3.10. Comparison of A) particle fraction entering and B) deposition fraction in each airway generation for bolus (blue) (n=3) and continuous (yellow) administration (n=3). Tidal volume = 1500mL, breathing frequency = 15/min. Particles were assumed to be spherical, rigid, smooth and to have a unit density (1g/mL). The black lines represent 1 standard deviation.

The bolus dispersion model was validated against in vivo data [70] for lung deposition (Figure 3.11) and bolus dispersion effect (Figure 3.12). Figure 3.11 shows good agreement between in silico and in vivo data. Figure 3.12 shows bolus dispersion with increasing tidal volume. An increase in tidal volume increased bolus dispersion.

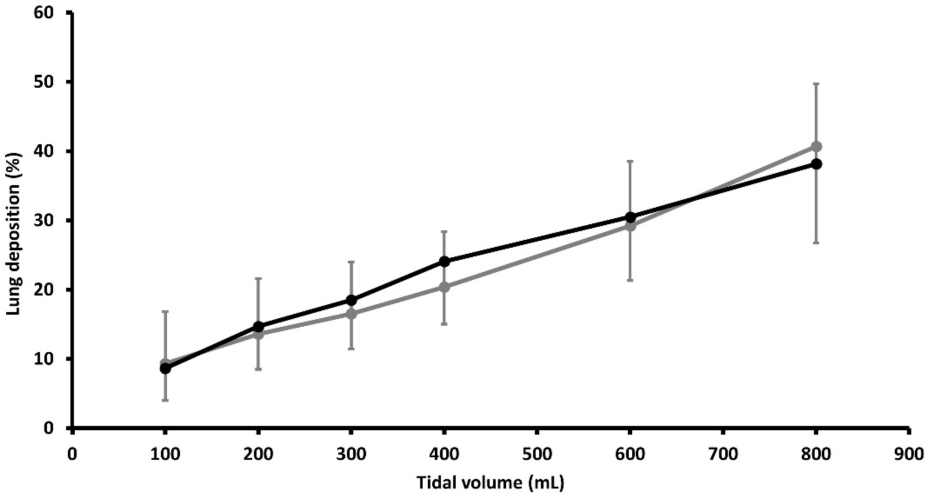

Figure 3.11. Comparison of the predicted deposition fraction of bolus administration for in vivo (grey line) and in silico (black line). x-axis is tidal volume and y-axis is deposition percentage (%). The black lines represent a standard deviation.

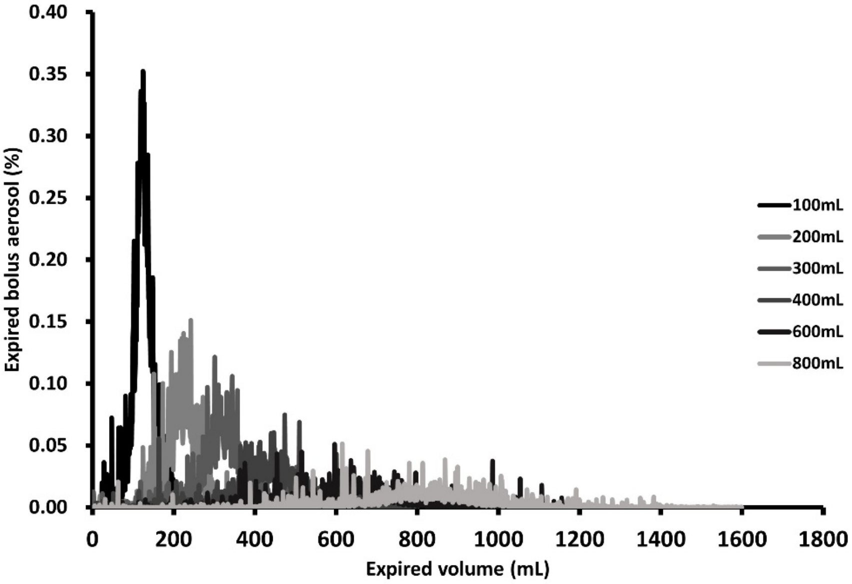

Figure 3.12. Expired bolus aerosol for different tidal volumes (100, 200, 300, 400, 600, and 800mL). It shows an increase in bolus dispersion with increasing tidal volume.

The results from the bolus administration model were compared to other in vivo study data for particle depositions in the extrathoracic region and in the lungs [83], [84], [85]. There was found to be good agreement, suggesting that the model accurately predicts human in vivo bolus lung deposition within the conditions studied.

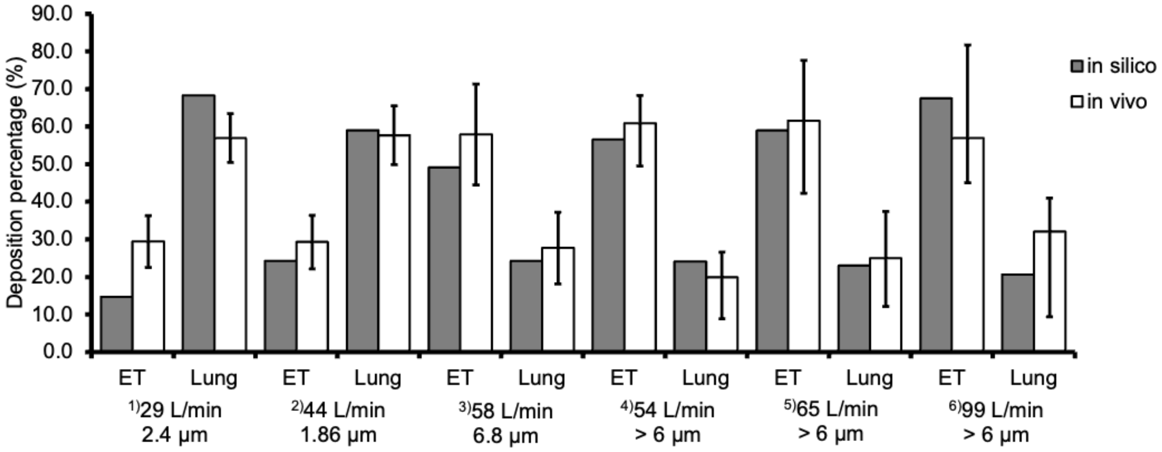

Figure 3.13. Results from the analytical bolus model ('in silico') are compared to in vivo data (Borgstrom et al., 1994 [83]; Duddu et al., 2002 [84]; Newman et al., 2000 [85]). Six different comparisons, indicated by superscripted bracketed numbers, are made for the extrathoracic region ('ET') and the lungs ('lung') deposition. in vivo data for conditions (1) and (2) are taken from [84]. Condition (3) is taken from [83] . Conditions (4), (5), and (6) are taken from [85]. LPM is an abbreviation for litres per minute (L/min). The particle size is the mass median aerodynamic diameter (MMAD). The orange bars ('in silico') represent data from the current analytical model. The blue bars ('in vivo') are the average values for conditions (1), (2), and (3), and the black lines represent one standard deviation. For conditions (4), (5), and (6), the blue bars are the median values, and the black lines with asterisks (*) represent ranges.

3.4 Conclusion

In this chapter, a lung airway model, airflow model, and particle deposition model were created. The lung airway model showed good agreement with other lung models and experimental data such as measurements of whole lung characteristics (Chapter 3.3.1). Successful development of the healthy lung models was followed by airflow and particle deposition calculation. Different analytical deposition equations were tested in the model, and a combination of impaction, sedimentation, and diffusion equations that best agreed with the in vivo human data was selected [68] (Chapter 3.3.2). Despite a simple airflow model and idealized airway geometry, the continuous administration model agreed well with the in vivo human data.

A bolus administration model was subsequently developed (Chapter 3.3.3). The bolus dispersion effect was added to the air flow and was validated against appropriate in vivo data [70]. The study compared the results of the bolus administration model with other research data on the deposition of particles in the lungs and extrathoracic region. [83], [84], [85], and showed good agreements. The findings of the study, however, are limited to the spherical shape and unit density of the particles. This particularly applies to particles whose deposition is diffusion-driven (i.e., nanoparticles). Aerodynamic diameter includes factors that determine particle deposition in sedimentation and impaction. However, aerodynamic diameter does not describe the factors that determine diffusion-driven deposition, and thus the study assumes spherical shapes and unit density. The bolus model was subsequently used in the next chapter, which investigated the use of controlled breathing parameters and micron-sized particles to target small conducting airways.

Chapter 4 Modelling drug delivery to the small airways: optimizing breathing parameters using Response Surface Methodology

4.1 Introduction

The small conducting airways are receiving increasing attention in chronic obstructive pulmonary disease (COPD) management. These airways, also known as the ‘silent zone’ of the lungs, have been historically overlooked because they account for only a tiny fraction of airway resistance (< 10 %) in healthy lungs [86], [87] and thus are thought to play only a minor role in airflow limitation in COPD patients. The lack of methods to measure the deterioration of small conducting airways has aggravated the situation. Spirometry, the primary method of measuring lung function, could not detect changes in the small conducting airways, especially in the early stages of COPD [88]. Thus, small conducting airways remained irrelevant in COPD management until a few decades ago. However, the finding that closures of small conducting airways are responsible for emphysematous destruction and increased peripheral airway resistance [6], [7], [8] in COPD patients redirected the focus of the research, and this is now an active field in COPD management.

Small conducting airways, also known as small tracheobronchial airways, are typically defined as those lacking cartilage and having an internal diameter of less than 2 mm [62]. These airways are located between the eighth generation of airways and the respiratory bronchioles. In COPD patients, tissues in the small airways exhibit chronic inflammation. The inflammation causes morphological changes in the cells. For instance, the airway walls are thickened due to squamous metaplasia and goblet cell hyperplasia, and inflammatory exudates obstruct the airway lumen [89]. These factors lead to reduced airway radius and, hence, airflow. The reduction in the small airway radius can further aggravate symptoms by premature closures of airways during expirations, leading to destruction in alveoli and a reduction in the number of acinar airways [90], [91].

Targeting therapy to small conducting airways, however, is challenging. A CFD simulation study has shown that conventional dry powder (e.g., Flovent Diskus) and metered-dose inhalers (e.g., Flovent HFA MDI) deliver less than 1% of the inhaled dose to small conducting airways [92]. Extrafine (i.e. < 1 μm diameter) particle inhalers have been shown to enable better lung deposition in the peripheral regions [93], [94] and improvements in symptoms in patients with severe COPD, e.g., reduction in exacerbation rate and improved lung function [95], [96], [97]. However, the optimal particle size of aerosols to effectively reach and deposit in the small airways has not been clearly defined [98].

Drug targeting in inhaled therapies involves modification of both drug particle characteristics and the inhalation pattern. Particle deposition in the upper and central airways is predominantly driven by inertial impaction [99]. Therefore, large particles (5 – 20 μm) and high flow rates favour deposition in the upper and central airways [100] [101]. Tidal volume also plays a role: an increase in tidal volume increases particle penetration and deposition in the deeper lungs and vice versa [102].

Various studies have attempted to optimise drug targeting in the lungs by changing inhalation patterns and/or particle characteristics. Brand et al., 2005 [103] studied the effect of tidal volume and flow rate on particle deposition in peripheral lungs of cystic fibrotic patients using 2, 3, 4, and 5.5 μm monodisperse particles. Other in vivo human studies have investigated the effect of particle size on regional deposition [68], [104]. However, no studies (to the best of the authors' knowledge) have examined the combined effect of tidal volume, flow rate, and particle diameter on deposition in the small conducting airways.

Design of Experiments (DoE) is a statistical method of designing experiments to create a descriptive model. It has been used in various industries (e.g., aerospace [105], chemical synthesis [106], agriculture [107], and pharmaceutical manufacturing [108]) for parameter optimisation. In this study, we extend its application to explore optimal parameters for targeting small conducting airways. An in silico whole lung particle deposition model is used with DoE to find the optimal parameters for drug targeting in the small conducting airways. Bolus administration, as delivered by dry powder inhalers (DPI) and soft-mist inhalers, is assumed. Pressurised metered-dose inhalers (pMDI) produce a high initial particle velocity regardless of inhalation rate, so they are not considered here.

4.2 Methodology

4.2.1 In silico lung particle deposition model

The airway model used for the present work was based on the whole lung particle deposition model developed in Chapter 3. Due to an insufficient data pool for airway dimensions in mild COPD patients, data from healthy human lungs were used. The difference in airway dimensions between healthy subjects and patients with mild COPD has been reported as being insignificant [109]. The number of small conducting airways in our model was around 60,000. Lung models were created using a Monte Carlo method [31], [32], and the full methodology of the airway model and its validation are described in detail in Chapter 3 and our previous paper [110]. The lungs were assumed to undergo linear expansion and contraction, and thus, the inhaled and exhaled flow rates were assumed to be constant. The flows in the lung airways were assumed to be steady [111]. The spatial average flow velocity was calculated by dividing volumetric flow by the corresponding airway’s cross-sectional area. The method was adapted from [112].

Steady flow was assumed. The effect of unsteady flow on particle deposition is most noticeable in the extrathoracic region, and thus, its effect on particle deposition in the region was incorporated into the model by using an empirical equation [113]. The effect of unsteady flow on particle deposition in the airways beyond the extrathoracic region appears to be marginal [114], and thus, unsteady flow is not expected to change lung deposition significantly.

For particle deposition, several analytical equations were compared, and a combination of analytical equations that best fit the in vivo data was selected [68], [110]. These were taken from Beeckmans (1965) [66], Ingham (1975) [67], and Landahl (1950) [63] for sedimentation, diffusion, and impaction deposition, respectively. Golshahi et al., 2013 [113] were used for extrathoracic deposition for the bolus administration model. Particles were assumed to be spherical, to have a smooth surface, to be rigid, and to have a unit density (i.e., 1 g/mL). Airway walls were also assumed to be rigid, and particle deposition was assumed to occur upon contact.

Bolus dispersion was modelled using the method from Hofmann et al., 2008 [69]. The model includes the effect of (1) mixing in the extrathoracic region, (2) convective mixing in conducting airways, (3) mixing at airway bifurcations, and (4) mixing of residual and new air in the alveoli. The bolus model was validated against in vivo lung deposition data for polydisperse dry powder inhalers [83], [84], [85]. The result is available in [110]. MATLAB R2022b (The MathWorks, Inc.) was used for the in silico lung particle deposition model.

4.2.2 Response surface methodology

This study used response surface methodology (RSM) to characterise the relationship between tidal volume, flow rate, particle diameter, and small conducting airway deposition (or small tracheobronchial deposition). The regression analysis was then used to find the optimal parameters that improved deposition. The optimal values were investigated using the bolus model within the following ranges: 100 – 2000 mL/s for flow rate, 40 – 1500 mL for tidal volume, and 0.4 – 10 µm for particle diameter. Respiratory time was fixed at 10 seconds. The ranges of flow rate and tidal volume were chosen to represent physiologically relevant breathing conditions. The particle diameter range reflects that used in commercially available dry powder inhalers.

A screening step was first performed (Figure 4.1) to characterise the relationship between the independent variables (i.e., particle diameter, flow rate, and tidal volume) and the response (i.e., small tracheobronchial deposition) in a simple first-order manner within the selected parameter range. The screening step used a fractional factorial (2^{3-1}) design. Low inhaled flow rate (i.e., 500 - 1000 mL/s), low tidal volume (i.e., 200 – 400 mL), and extrafine dry powder inhalers (i.e., 0.4 – 1.0 µm) have been reported to improve deposition in distal airways [103], and thus these parameter ranges were selected for the screening step.

The linear equation derived from the screening step was then used to determine the direction of change for each independent variable to increase the response (Figure 4.1). This is called the method of steepest ascent. It helps to find the region of the optimum, which is the parameter range that includes the optimal parameter set. The independent variables were increased or decreased in equal intervals. They continued until the response started to drop, indicating the region of the optimum.

Central composite design (CCD) was then used to develop a descriptive second-order model inside the region of the optimum point (Figure 4.1). The model was described by linear terms (x_i), quadratic terms (x_i^2), cross-product interaction terms $(x_i x_j)$, intercept (β_0) and the error term (ε). To avoid overfitting, terms that have insignificant contributions to the response were deleted based on ANOVA analysis. Terms with p-values greater than 0.10 in ANOVA were eliminated using backward elimination.

The quadratic model was assessed for accuracy and predictability using adjusted R^2 and predicted R^2 values [115]. Contour plots and factorial plots were used to visualise and examine the relationship between independent variables and the response. The optimal parameter conditions were found, and the predicted responses were validated using the lung deposition model.

Lastly, ten random CCD simulations were conducted within the studied range (namely, 100 – 2000 mL/s for flow rate, 40 – 1500 mL for tidal volume, and 0.4 – 10 µm for particle diameter). This checked for any other region of optimum that may have a high small tracheobronchial deposition. RSM and its statistical analysis were conducted using Minitab® Version 20 (Minitab LLC) software.

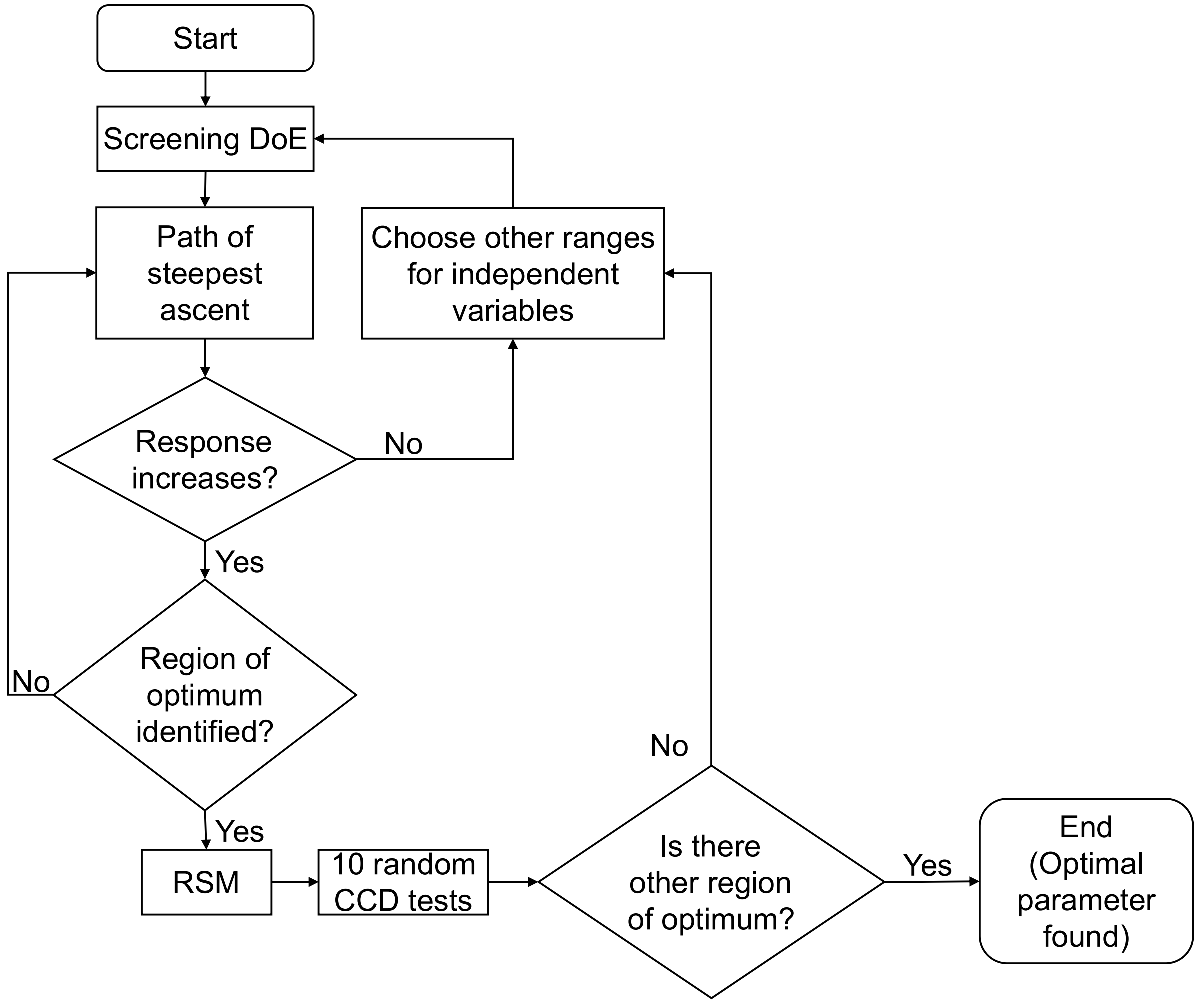

Figure 4.1 shows the steps used to find the optimal parameters for targeted delivery in small tracheobronchial airways. It began with the initial screening step. A minimum number of simulations was used to find a linear relationship between the three variables (particle diameter, flow rate, and tidal volume) and the deposition. The linear relationship derived from the screening step was used for the method of steepest ascent step. The variables were changed in the direction of increasing the deposition. This step allowed us to find the region of the optimum. A CCD model was created inside the region. The model was used to find the optimal parameters for drug targeting. The flow chart ends with a double-checking step. Ten CCD models were created at random points inside the studied ranges to confirm that there are no other regions of the optimum.

4.3 Results and Discussion

4.3.1 Response surface methodology

The screening step revealed that small tracheobronchial deposition increased with an increase in particle diameter and decreased with an increase in flow rate and tidal volume

(Figure 4.2A). In the method of steepest ascent step, flow rate and tidal volume were decreased by 50mL/s and 20mL, respectively. At the same time, particle diameter increased by 0.1 in log-10 scales (Figure 4.2B). Incrementally increasing particle diameter in log-10 scales allowed more data points in the smaller particle diameters (1 – 5 μm), where changes in response are proportionally larger. It showed the change in deposition with incremental changes in each independent variable. CCD was thus set up around the region where small tracheobronchial deposition is highest to analyse the relationship (Figure 4.2C).

The CCD model accurately described the relationship, as suggested by the high adjusted R^2 value (88.63 %), but the difference between adjusted R^2 and predicted R^2 values (> 10 %) suggested possible overfitting (Table 4.1). It was, however, later confirmed in the validation study (Table 4.2) that the response prediction by RSM is in good agreement with the whole lung deposition simulation data.

Ten more CCD models were created at random points within the studied ranges, but no other optimal region was found in the studied ranges. This suggests that the region found by the method of steepest ascent is the only region relevant for delivery to the small tracheobronchial airways (Figure 4.2D).

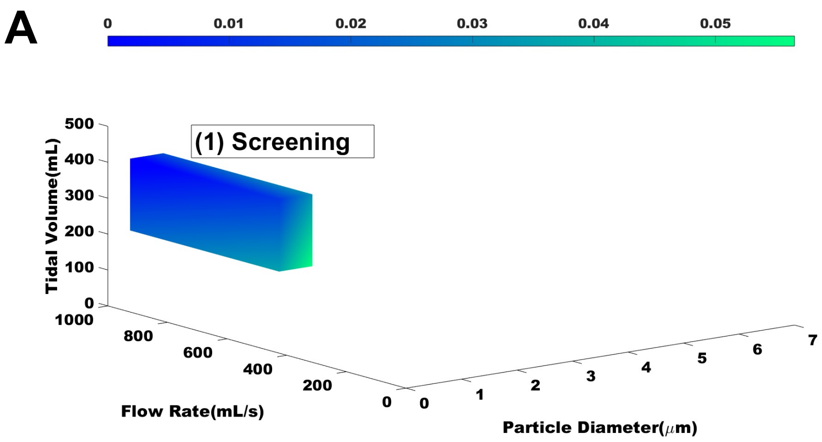

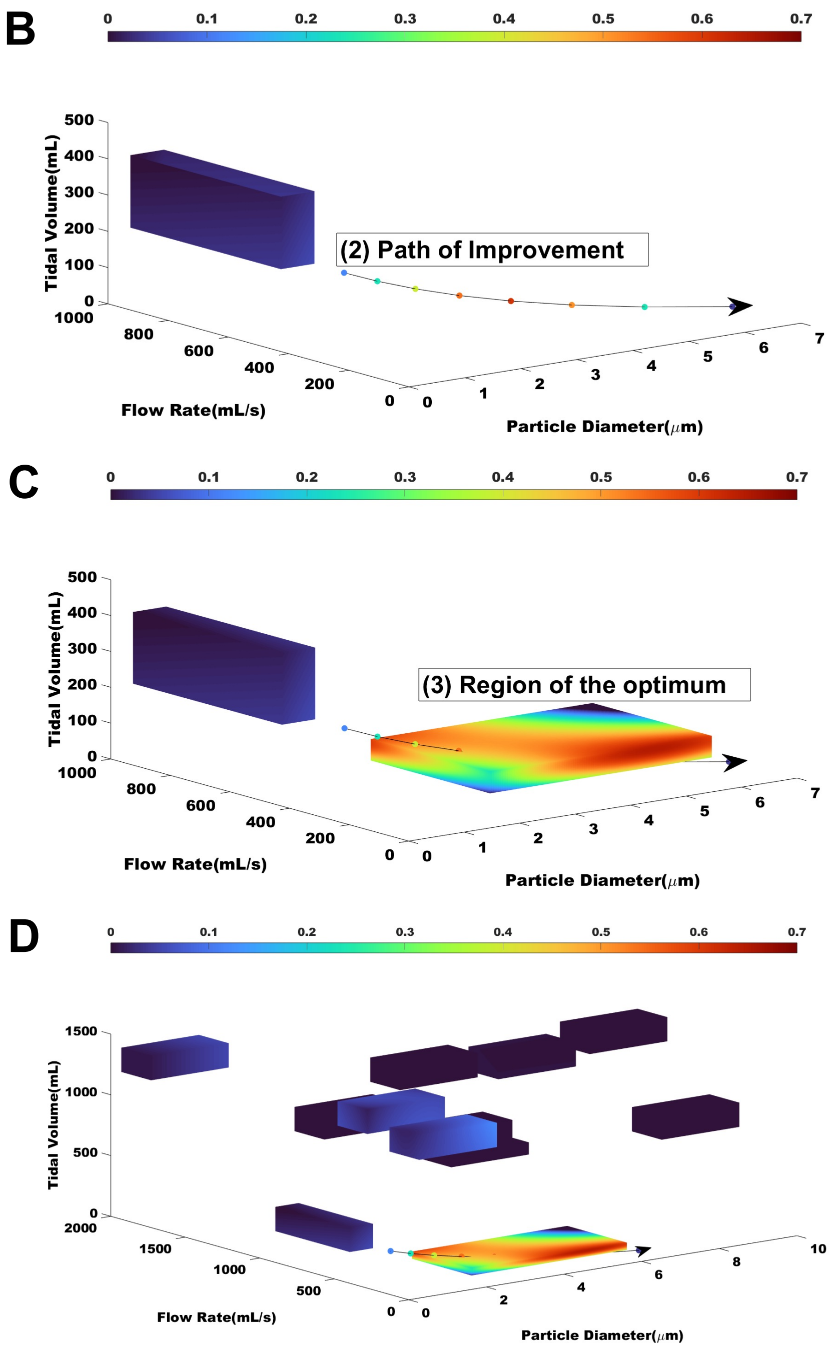

Figure 4.2. shows the steps used to find the optimal parameters for targeted delivery in small tracheobronchial airways. (A) shows the initial screening step. A minimum number of simulations was used to find a linear relationship between the three variables (particle diameter, flow rate, and tidal volume) and the deposition. (B) is the method of steepest ascent step. The variables were changed in the direction of increasing the deposition. This step allowed us to find the region of the optimum. (C) shows a CCD model that was created inside the region. The model was used to find the optimal parameters for the drug targeting. (D) shows a double-checking step. Ten CCD models were created at random points inside the studied ranges to double-check that there are no other regions of the optimum. The color bar represents the deposition percentage (%).

Deposition region	Equation	R^2 (adj)	R^2 (pred)
Small TB	$y = -186.1 + 52.80\,\mathrm{A} + 2.29 \times 10^{-1}\,\mathrm{B} + 2.11\,\mathrm{C} - 4.63\,\mathrm{A}^2 - 9.70 \times 10^{-3}\,\mathrm{C}^2 - 7.09 \times 10^{-2}\,\mathrm{AB}$	88.63 %	74.46 %

Table 4.1. A quadratic model equation for small tracheobronchial (Small TB) is presented. A, B, and C are particle diameter, flow rate, and tidal volume, respectively. Superscript 2 on the alphabet represents the quadratic terms, and two alphabets represent interaction terms (i.e., AB is the interaction term for A and B). Terms were removed from the equation using the backward elimination method for p-value > 0.10.

4.3.2 Targeted delivery to small tracheobronchial airways

As expected from the literature, deposition in the small tracheobronchial airways was found to be affected by tidal volume, particle size, and flow rate (Figure 4.3). Tidal volume and particle diameter had a negative quadratic relationship with deposition, suggesting that local maxima and, hence, potential optimal conditions exist.

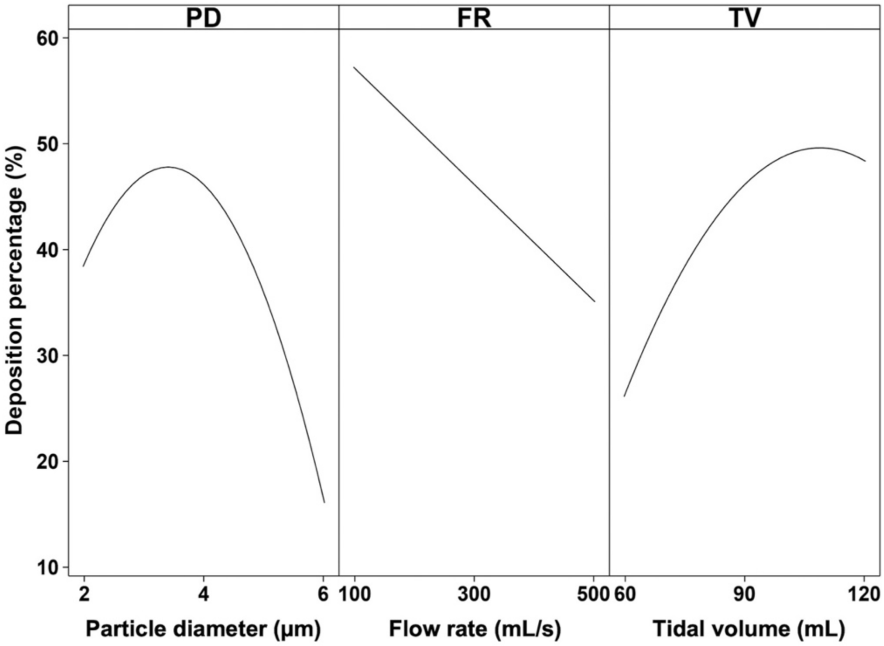

Figure 4.3. The predicted effects of particle diameter, flow rate (FR), and tidal volume (TV) on small tracheobronchial deposition

Small tracheobronchial airway deposition was found to be highly dependent on tidal volume and flow rate. Figure 4.4A and B show the effect of flow rate and tidal volume on deposition of 2 µm and 4.9 µm monodisperse aerosol particles, respectively. Both particle sizes showed the highest deposition at 109.1 mL tidal volume. The flow rate, on the other hand, affected the two particle sizes differently. It was found that a higher flow rate (500 mL/s) was favourable for aerosols of 2 µm diameter and vice versa for monodisperse 4.9 µm aerosols.

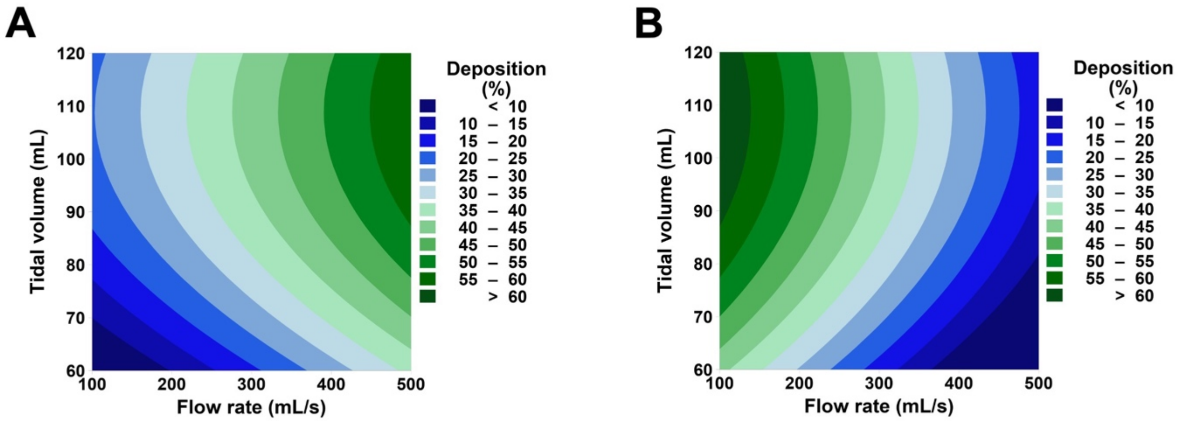

Figure 4.4. Contour plots showing the effects of tidal volume and flow rate on small tracheobronchial deposition for monodisperse aerosols having particle diameters of **(A)** 2 µm and **(B)** 4.9 µm. The graphs show that small tracheobronchial deposition can vary from below 10 % to above 50 %, depending on the tidal volume and flow rate.

Figure 4.5 shows that the optimal flow rate for small tracheobronchial deposition varies with particle size. The larger particles (i.e., 4 – 6 µm) increased deposited in the airways at slower flow rates (i.e., around 100 mL/s), whereas the smaller particles (i.e., 2 – 3 µm) increased the deposition at higher flow rates (i.e., around 500 mL/s). Large particles (i.e., 4 – 6 µm) at slow flow rates facilitate increased particle penetration into the small tracheobronchial airways because the slow flow rate reduces deposition in the extrathoracic and large tracheobronchial regions. On the other hand, smaller particles (i.e., 2 – 3 µm) deposit in the small airways better at higher flow rates because of inertial impaction in the small tracheobronchial airways.

The optimal sets of parameters for targeting small conducting airways may, however, change depending on various factors, such as the disease state and age. The airway model is based on healthy lungs, which should accurately represent the lung airways of mild COPD patients. However, as COPD progresses into moderate or severe states, the number of distal airways reduces, and airways begin to narrow [109]. Despite the fact that several clinical studies have found that the disease state of COPD does not change lung deposition and its deposition pattern [116], [117], [118], the authors believe that these factors may change the optimal breathing and particle parameter for targeting the small conducting airways. Firstly, the location of stenosis in the lung airways can affect lung particle deposition differently. For instance, stenosis in the upper airways can increase deposition in the region and thus reduce the available particles in the small conducting airways [119]. Secondly, a reduced number of distal airways in certain regions of the lungs can selectively reduce airflow and, thus, particle deposition in those specified parts of the lungs. Therefore, it is suspected that the severity of COPD will affect lung particle deposition, and thus, the optimal set of parameters would change.

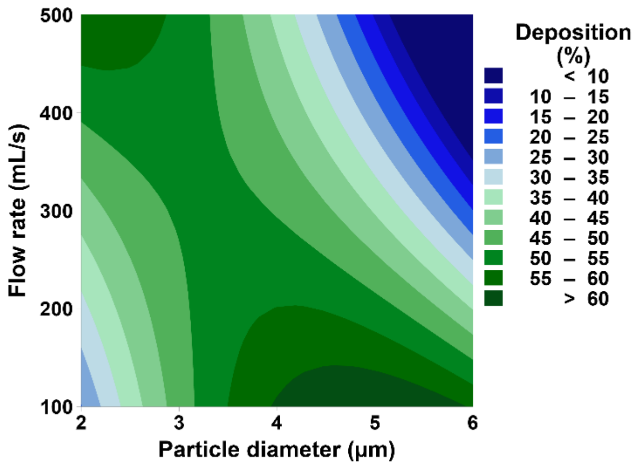

Figure 4.5. A contour plot shows the effects of particle diameter and flow rate on small tracheobronchial deposition. The tidal volume is set at 109.1 mL.

The optimal parameters were found using the desirability function approach, incorporated within 'Response Optimization' function of Minitab®. It found two optimal parameter sets (Table 4.2) suggesting that large aerosols sized 4.9 μm in diameter could target the small tracheobronchial airways when inhaled at a flow rate of 100 mL/s and with a tidal volume of

109.1 mL; and that particles with a relatively small diameter (2 μm) could target the small tracheobronchial airways when inhaled at 500 mL/s of flow rate and 109.1 mL of tidal volume.

Regional deposition	Optimal parameter set			Deposition percentage (%)	
	Diameter (μm)	Flow Rate (mL/s)	Tidal volume (mL)	Predicted (95 % C.I.)	Validation (95 % C.I.)
Small TB	4.9	100.0	109.1	64.6 % (51.9 – 77.3 %)	53.6 % (38.9% – 65.2%)
	2.0	500.0	109.1	55.5 % (38.0 – 72.5 %)	42.0 % (38.9 – 45.2 %)

Table 4.2. Optimal parameter sets for high deposition percentage in small tracheobronchial are given. The predicted deposition percentage using the CCD model (‘Predicted’) is compared to the in silico lung particle deposition model (‘Validation). The in silico model values given are the averages of 20 samples (n = 20), and 95 % confidence interval (C.I.) is given. ‘Predicted’ and ‘Validation values were found not to be significantly different ($p < 0.05$, 2-way t-test).

It was previously reported that commercial inhalers deliver less than 1% of the emitted dose to the small conducting airways, which are typically inflamed in COPD [92]. Controlling aerosol size has been suggested as a means of improving drug delivery to the region, and inhalers with extrafine particles (i.e., < 1 μm) have been reported to improve symptoms of COPD [98], [120], [121]. There is, however, no direct evidence of increased drug delivery to the small conducting airways nor direct proof of reduction in inflammation in the small conducting airways. The improvement in symptomatic outcomes could be a result of increased deposition in the alveolar airways and increased systemic exposure.

In contrast to the currently accepted notion that particle size control is crucial for targeting the small conducting airways, this study suggests that drug targeting may be achieved by more simply controlling the tidal volume and flow rate. Figure 4.5 shows that a wide range of particle sizes from 2 to 6 μm can achieve a high deposition percentage (> 50 %) if flow rate and tidal volume are controlled. Similarly, shows that the change in flow rate and tidal volume can reduce deposition percentage from above 50 % to below 10 %. The findings suggest that inhalers with different aerosol sizes could successfully target the small conducting airways by controlling the flow rate and tidal volume of COPD patients.

4.3.3 Practical considerations and limitations

In this study, targeted delivery to the small tracheobronchial airways was found to require fine control of tidal volume and flow rate. Such fine control of breathing, however, is unachievable without a device that controls the entire inhalation maneuver of patients. For example, the AKITA inhalation system (Activaero, Gemünden, Germany) is a computer-controlled compressor that stores and analyses subjects' breathing patterns. It controls the tidal volume and flow rate by applying positive air pressure. AKITA has successfully controlled subjects' breathing characteristics and reduced flow rate and tidal volume variability [122].

Unfortunately, the AKITA inhalation system is not yet compatible with inhalers for bolus administration (e.g., pMDI, DPI, or soft-mist inhalers), and there are no other systems currently available. The lack of inhalation control systems may be due to poor incentives for development. The market for inhalation control systems is limited to clinical trials, and thus, the market size is insufficient to incentivise new development. This study, however, shows that controlling tidal volume and flow rate is critical for targeting the small conducting airways. If inhalation systems were found to improve prognosis in COPD patients, they might become a central part of COPD management.

If found to be efficacious, the treatment for small conducting airways would complement the current therapy rather than a replacement. Deposition in the small conducting airways alone would not improve the prognosis of COPD patients because other regions of the lung airways, such as large conducting airways and respiratory airways, also play essential roles in COPD management. For instance, large conducting airways determine lung function tests such as

FEV_1, FVC, and FEV_1/FVC [123]. The acini are responsible for gas exchange [124]. Thus, the treatment for small conducting airways would be an add-on to the current regimen of COPD management, which may help to improve small airway obstructions and, thus, patient prognosis.

There are, however, some important limitations to practical implementation. The first is that the device-flow rate interaction adds complexity to optimising drug delivery with dry powder inhalers. The negative peak pressure (which controls the flow rate) determines the emitted dose and the emitted particles' mass median aerodynamic diameter (MMAD). Hence, the optimal flow rate for the device should ideally match the optimal flow rate for the target lung region. The second limitation is that increasing the complexity of the treatment regimen can result in poor adherence. Effective patient education and behavioural assistive tools may help to address poor adherence, but further research will be required to determine the appropriate level of intervention.

The current lung deposition model assumes that the aerosols have no initial velocity. Hence, the aerosols have the same velocity as the air. This means the findings apply to dry powder inhalers and possibly soft-mist inhalers but not pressurised meter-dose inhalers. In future studies, particle-fluid dynamics of different inhalers can be incorporated into the model to study the effect of inhaler devices on small tracheobronchial deposition.

4.4 Conclusion

This study used the DoE methodology to find the optimal breathing and particle characteristics for targeting the small conducting airways. The model developed was compared to experimental data and was found to accurately describe the relationship between lung regional particle deposition and three independent variables (tidal volume, flow rate, and particle size). The model found that all particles between 2 and 6 µm can sufficiently target the small conducting airways (i.e., > 50 % of emitted dose) when tidal volume and flow rate are controlled. This study suggests that tidal volume and flow rate are critical for drug targeting. Thus, the development of an inhalation control system that is compatible with DPI, pMDI, or soft-mist inhalers may help to achieve drug targeting to the small conducting airways.

The present study found that conventional inhalers can potentially effectively target drug delivery to the small conducting airways using an inhalation control system. This has consequently weakened the need for microbubbles for drug targeting to these airways. As a result, the current study aimed to explore a different application for inhalable microbubbles. To this end, a comprehensive literature review was conducted about neonatal respiratory distress syndrome (nRDS) and nebulised lung surfactant therapy, with a particular focus on identifying potential applications of inhalable microbubbles for nebulised lung surfactant therapy in preterm neonates with nRDS.

Chapter 5 Literature review on nRDS

5.1 Introduction

Neonatal respiratory distress syndrome (nRDS) is a widespread respiratory disorder that occurs primarily in preterm neonates, usually within hours after birth, and infrequently in term infants. The incidence of RDS is inversely proportional to the gestational age of the infant, with more severe disease observed in smaller and more premature neonates. Despite treatment advancements, including antenatal corticosteroids, surfactants, and advanced respiratory care of the neonate, RDS remains a leading cause of morbidity and mortality in preterm infants. This chapter reviews the current knowledge of nRDS, lung surfactants, and lung surfactant proteins, as well as the research progress on nebulised lung surfactants in pre-term neonates.

5.2 Pathology of nRDS

In healthy lungs, the surfactant is distributed as a thin film across the air–liquid interface of the alveolar surface, effectively reducing surface tension. It reduces the pressure required to facilitate subsequent alveolar inflation and preserves an optimal functional residual capacity [125]. The reduced surface tension is also important to reduce the risk of alveolar collapse, which is particularly high during end-expiration. Furthermore, it mitigates the pressure required for subsequent alveolar inflation and preserves an optimal functional residual capacity [126].

The lungs of premature infants exhibit structural and biochemical immaturity. A significant proportion of premature infants requiring ventilatory support are born during the saccular phase of lung development, spanning from the 24th to the 36th week of gestation [127]. In this phase, the distal lung sees the initiation of the formation of alveolar ducts, which represent the last airway generation before the establishment of mature alveoli [127]. Concurrently, the synthesis and release of pulmonary surfactant by type II alveolar cells commence around the 24th week of gestation, steadily increasing until birth [128]. The presence of surfactant in the alveolar space plays a crucial role in modulating surface tension throughout the respiratory cycle, minimising it to nearly zero at low gas volumes and preventing alveolar collapse at end-expiration [126]. As intrapulmonary surfactant pools gradually augment with advancing maturation, the least mature infants consequently exhibit the lowest levels of intrapulmonary surfactant, placing them at the highest risk of developing nRDS [129].

In the absence of a sufficient quantity of fully developed pulmonary surfactant, infants afflicted with nRDS progressively exhibit atelectasis and anomalies in lung function. Notably, at end-expiration, the alveoli are prone to collapse, resulting in a diminished functional residual capacity [130]. Consequently, the pressure necessary for lung inflation is elevated, lung compliance experiences a reduction, and the overall work of breathing is significantly heightened. Infants with nRDS typically manifest a diminished tidal volume and an augmented physiological dead space [131].

Atelectasis, concurrent with regions of overinflation, may coexist, particularly in mechanically ventilated infants. Atelectasis can result in ventilation–perfusion mismatching and intrapulmonary shunting. This condition hinders carbon dioxide elimination and diminishes oxygen saturation in pulmonary venous blood, thereby inducing respiratory acidosis and hypoxemia [132]. Prolonged hypoxemia gives rise to metabolic acidosis, decreased cardiac output, and hypotension. Consequently, arterial blood gases in severe nRDS reflect a mixed metabolic and respiratory acidosis. The danger of acidosis is that it can further diminish surfactant production and elevate pulmonary vascular resistance, in some cases resulting in death [133].

The chances of survival for infants with nRDS increase dramatically two days after birth [134]. Endogenous surfactant production initiates around 2–3 days after birth, marking the clinical improvement of respiratory distress. Through the reduction of surface tension, surfactant facilitates the re-expansion of alveoli during inhalation. As a result, effective gas exchange occurs by aligning ventilation and perfusion. From a clinical perspective, there is a notable enhancement in functional residual capacity, accompanied by a significant reduction in the effort required for breathing due to decreased airway resistance and improved lung compliance [135].

5.3 Lung surfactant – the lipid fraction

Lung surfactants primarily consist of phospholipids, making up around 80% of their mass. These amphiphilic molecules form an oriented monolayer at the alveolar interface, with hydrophobic acyl chains exposed to the air and polar headgroups facing the aqueous phase. Dipalmitoyl phosphatidylcholine (DPPC) is the most abundant phospholipid in lung surfactants (40%), contributing to minimal surface tension values at the end of expiration. Other phospholipids and anionic phospholipids, like phosphatidylglycerol and phosphatidylinositol, play essential roles in interactions with surfactant proteins [136].

Cholesterol (5–10% of phospholipid mass) is crucial for modulating lipid packing in lung surfactant, influencing lateral structure and functionality. Minor variations in cholesterol levels can have a significant impact [137]. Neutral lipids, including cholesterol esters, triglycerides, diglycerides, and free fatty acids, are present in small quantities. Phospholipid packing, integral to LS surface activity, is influenced by composition, temperature, and lateral pressure.

The surface activity of lung surfactant is fundamentally influenced by the packing of phospholipids, a process intricately regulated by factors such as composition, temperature, and lateral pressure [138]. The melting temperature (T_m) plays a crucial role in this context, representing the point at which a transition occurs from a gel to a fluid phase in pure phospholipid membranes, signifying an ordered-to-disordered shift. Below T_m, phospholipid mobility in bilayers is significantly restricted, indicating a gel phase. Conversely, temperatures above T_m lead to enhanced lateral fluidity, representing a liquid-crystalline fluid phase.

The specific molecular properties of phospholipids determine T_m, with DPPC, featuring two saturated acyl chains, exhibiting a T_m of 41 ◦C, while membranes comprising unsaturated acyl chain-containing phospholipids like palmitoyl-oleoyl-phosphatidylcholine (POPC) have a considerably lower T_m, reaching as low as -3 °C. Additionally, cholesterol has a profound impact on membrane lipid packing, fluidising gel phase and stiffening liquid-crystalline fluid phase. Membranes with cholesterol exhibit lateral structuring into liquid-ordered and liquid-disordered phases [138].

In monolayers, phase transitions are typically associated with alterations in surface pressure (Π), where $\Pi = \gamma_0 - \gamma$, with γ_0 representing the surface tension of a clean air-water interface (72 mN/m at 37 ◦C). Consequently, a phospholipid monolayer assumes a gas phase when the phospholipid's surface concentration is low, indicating exceptionally high lipid mobility. As molecules approach and make contact due to area reduction, the monolayer structurally forms a liquid-expanded phase. With increasing surface pressure, the acyl chain mobility gradually diminishes, leading the monolayer to adopt a liquid-condensed phase. Ultimately, monolayers can attain a solid-like two-dimensional state at sufficiently high surface pressure, characterised as solid-ordered phases [138].

Surfactant lipid membranes can organise into various three-dimensional structures in aqueous suspensions through lipid polymorphism. This self-aggregation capability results in different structures, such as lamellar or non-lamellar phases. The shape of phospholipids, particularly the arrangement of hydrophilic and hydrophobic moieties, is crucial for understanding LS adsorption at the interface and its reorganisation during breathing dynamics.

5.4 Lung surfactant – the proteins

The functions of lung surfactant are intricately tied to the involvement of four proteins [139], categorised into two groups: (i) hydrophobic surfactant proteins SP-B and SP-C, playing a crucial role in the surface activity of lung surfactant and (ii) hydrophilic proteins belonging to the collectin family, namely SP-A and SP-D, primarily associated with innate immunity in the alveolar spaces.

SP-B is a positively charged polypeptide consisting of 79 amino acids (8.7 kDa) with a predominantly amphipathic α-helical secondary structure [140], [141]. It features six conserved cysteines forming three intramolecular disulphide bonds and an additional cysteine involved in an intermolecular disulphide bond that stabilises a homodimer [140]. Alongside the homodimer, SP-B is suggested to create oligomers structured as hydrophobic channels, facilitating the flow of phospholipids across various surfactant structures. This includes the movement of surface-active lipid species from the aqueous phase to the interface [142]. SP-B demonstrates activities such as permeabilisation, aggregation, fusion, and lysis of phospholipid vesicles (liposomes) in vitro [143], [144], [145]. These activities are closely associated with lung surfactant adsorption and the established connections between the interfacial monolayer and associated membrane reservoirs [140]. Moreover, SP-B plays a crucial role in the assembly of surfactant lipids into lamellar bodies during the intracellular storage of lung surfactant [146]. Notably, SP-B deficiency is fatal, underscoring its vital biological function [147]. On the other hand, SP-C is a small hydrophobic protein composed of 35 residues (3.7 kDa). Its deficiency is not lethal at birth but may be linked to chronic respiratory disorders. SP-C is essentially a transmembrane α-helix with a positively charged N-terminal segment that contains two palmitoylated cysteines, contributing to the stabilisation of its helical structure [148]. It has been suggested that SP-C facilitates vesicle fragmentation by stabilising a dimeric form that promotes membrane curvature [149].

SP-A and SP-D belong to the hydrophilic, oligomeric, and fibrous proteins constituting the collectin family. The SP-A monomers consist of four domains: an N-terminal domain, a collagen-like domain forming a trimeric stem through triple helix formation in the quaternary structure, an α-helical connecting region, and a C-terminal region containing a carbohydrate recognition domain (CRD) with calcium-binding sites [150]. Octadecamers are formed by six SP-A trimers, where three C-terminal domains create a globular end. Consequently, each octadecamer encompasses six of these globular heads. Conversely, SP-D forms dodecamers composed of four trimers, with each monomer also featuring the four described domains characteristic of collectins [151]. Both proteins exhibit the ability to recognise, bind to, opsonise, and present microorganisms to immune system cells, along with intrinsic antimicrobial activity [152]

5.5 Clinical trials on nebulised lung surfactant (relevant to Chapter 6)

In 1964, Robillard and colleagues made the pioneering attempt to treat neonates with nRDS by nebulising a synthetic lipid mixture using an aerosol generator placed in the incubator [153]. The nebulisation duration ranged from 15 minutes to four hours, resulting in the alleviation of respiratory distress in 8 out of 11 treated infants [153]. Over the years, advancements in aerosol and ventilatory technologies have significantly enhanced the management of respiratory conditions in the neonatal population.

Most clinical trials involving nebulised lung surfactants have been with small sample sizes, which makes discussion for treatment efficacy inadequate [154], [155]. Instead, the discussion emphasises the potential impact of the chosen non-invasive ventilation (NIV) modality, the type of nebuliser, and its placement in the respiratory circuit on the quantity of inhaled drugs.

The initial clinical investigation involving nebulised surfactant with NIV was conducted by Jorch et al. in 20 premature infants (28–35 weeks gestational age) receiving pharyngeal bubble continuous positive airway pressure (CPAP) in an uncontrolled study [156]. Nebulised surfactant (Bovactant, Alveofact, Lyomark Pharma, Obehaching, Germany) was administered through a jet nebuliser (RO252/ME, Intersurgical, Wokingham, UK) directly connected to a T piece positioned between the inspiratory limb and a nasopharyngeal tube. Improvements in oxygen saturation were observed, with only 6 out of 20 infants requiring intubation. It is worth noting that jet nebulisers produce high-speed particles that require deceleration to limit impaction. The placement of the nebuliser near the airway was likely chosen to minimise drug losses but may have resulted in a substantial amount of drug impacting the nasopharyngeal tube. This impact could lead to surfactant reaching the pharynx in liquid form rather than as an aerosol, causing drug accumulation in the upper airways rather than the lungs.

Arroe et al. documented the therapy of 22 infants (22–36 weeks gestational age) utilising a Sidestream 45 jet nebuliser positioned in the inspiratory limb of the circuit [157]. The treatment did not demonstrate any therapeutic effect. The absence of surfactant proteins in the synthetic surfactant employed (Exosurf) and the minimal inhaled dose (due to the nebuliser type and its position) are probable factors contributing to the observed lack of clinical effectiveness.

Berggren presented findings from a limited non-randomized trial involving 34 infants (27–34 weeks gestational age) where CPAP alone was compared to CPAP in conjunction with nebulised surfactant. In contrast to earlier investigations, the utilised technology was intricately explained [158]. A jet nebuliser (Aiolos, Karlstad, Sweden) was situated in the inspiratory limb of a variable flow ventilator (Infant Flow, Dansjö Medical AB, Bromma, Sweden) with a flow of 7 L/min and a nebulisation rate of 0.2 mL/min. The treatment spanned about 3 hours to nebulise a total of 34 mL of study medication (Poractant alfa, Curosurf®, 480 mg diluted with saline to a 20 mg/mL concentration). The authors ensured the drug maintained its surface tension properties on a Wilhelmy balance before commencing the study. Despite the safety of surfactant nebulisation, the study outcomes were unfavourable. The authors acknowledged that an unmeasurable factor influencing the results was lung deposition in the patients. As a substitute, they gauged lung deposition post-nebulization in a rat model. The quantity of exogenous phospholipids in post-mortem lung lavages after surfactant aerosolisation represented only 0.5% of the nominal surfactant dose. However, the authors noted a significant enhancement in arterial oxygenation after nebulisation, although aerosolised surfactant remained notably less effective than bolus endotracheal surfactant administration [159]. Nevertheless, the animal study involved mechanically ventilated rats, enabling better control over air leaks compared to the clinical study; these factors likely contributed to an even lower lung deposition in the clinical investigation.

Nebulisation using a vibrating-membrane nebuliser was first reported by Finer et al., [160]. The nebuliser was positioned at the Y piece with a special connector to prevent surfactant loss into the expiratory limb, particularly when linked to either bubble CPAP or synchronised nasal intermittent ventilation. The trial aimed to investigate two prophylactic surfactant regimens in 20 preterm infants categorised by gestational age (28–29 and 30–32 weeks gestational age). These infants were treated with 20 mg/mL of synthetic surfactant (Lucinactant) over a 3-hour period, allowing up to 3 surfactant retreatments. The generated aerosol had a low Mass Median Diameter (MMD) of 1.9 ± 0.3 µm, with an aerosol output rate reaching a maximum of 0.4 mg/min. The authors asserted that under these conditions, surfactant delivery to an infant of up to a maximum total dose of 72 mg was possible, similar to the dose provided by endotracheal administration. The study results indicated a transient beneficial effect, distinct from observations with endotracheal surfactant. However, the actual lung dose might have been considerably less than claimed due to short neonatal inspiratory times and leakage at the patient interface. Indeed, the low lung delivery could account for the absence of sustained efficacy.

Most recently, Dani et al., 2022 conducted a clinical trial Phase 2 study nebulising poractant alfa to preterm infants (28 – 32 weeks gestational age) after optimisation of the nebuliser type, position, and delivery rate[161]. The study assessed nebulised poractant alfa's effectiveness (at 200 mg/kg and 400 mg/kg) in combination with nasal continuous positive airway pressure (nCPAP) versus nCPAP alone in premature infants with respiratory distress syndrome. Involving 129 infants born between 28 to 32 weeks of gestation, the trial was stopped early. Results showed no significant differences in respiratory failure rates or secondary outcomes between the groups. Nebulised poractant alfa was well-tolerated, with no serious adverse events related to the treatment. In conclusion, the intervention did not reduce the likelihood of respiratory failure within the initial 72 hours of life.

5.6 Surface activity of SP-B and SP-C (relevant to Chapter 7)

Newly produced lung surfactant complexes must adhere to the air-liquid interface to reduce surface tension. The insertion of lipids from lung surfactant membranes into the interface is a crucial process and necessitates bilayer-to-monolayer transitions to form active interfacial films. Anionic phospholipids and proteins SP-B and SP-C are vital in this process [138]. SP-B forms assemblies, which are believed to be instrumental in the rapid movement and distribution of lipid species among membranes in multilamellar arrays (i.e., lamellar-body particles or LBP) [143]. LBPs expose external SP-B assemblies, which likely initiate the initial contact with the interface. Furthermore, SP-B's ability to facilitate membrane aggregation, fusion, and permeabilisation may be linked not only to stabilising non-lamellar phases but also to the swift flow of lipids between the monolayer and membrane reservoirs [143].

Once pulmonary surfactant is adsorbed and spreads across the air-liquid interface in the lungs, it significantly reduces surface tension (γ) during exhalation by undergoing rapid changes with only a limited reduction in surface area [136]. In laboratory experiments, γ drops from 70 mN/m to 25 mN/m at 37 °C immediately after LS adsorption and reaches values close to <2 mN/m with a modest 10–15% area reduction, corresponding to the end of exhalation. This process, known as the "squeeze-out," involves a potential restructuring of surfactant films to achieve minimal γ during alveolar compression [162]. During lateral compression, certain components like unsaturated phospholipids, cholesterol, and surfactant proteins, unable to withstand high pressure (Π), are excluded from the interface. This exclusion results in a lipid film enriched with DPPC, exposed to air, and capable of meeting the demanding surface requirements. The mechanical characteristics of a DPPC monolayer at Π near 70 mN/m resemble those of a solid-like material. Additionally, through interactions mediated by lipids and proteins, the monolayer is linked to membranous reservoirs containing excluded lipids, proteins, and newly secreted lung surfactant complexes. These reservoirs play a crucial role in supplying the interface with fresh lipids during inhalation and providing mechanical stability due to cohesive interactions between protein layers within the reservoir [163].

It is suggested that nucleation points of condensed domains enriched in DPPC are attached to the interfacial monolayer on the air-liquid interface. These condensed domains, upon compression, would grow to eventually form an extended solid phase [138]. Although the exact mechanisms through which SP-B and SP-C modulate the mechanical properties of LS membranes during compression-expansion cycles are not fully understood, SP-B and SP-C are believed to regulate the mechanical properties of the interfacial monolayer during the dynamic process of breathing. During inspiration, the monolayer reverts its structure to the liquid phase when less packable lipids (e.g., anionic lipids, unsaturated phospholipids, cholesterol) re-adsorb.

To investigate the formation of interfacial monolayers from lung surfactants, researchers have historically employed adsorption experiments with surface balances. Klenz and colleagues proposed a two-step model for LS adsorption, suggesting that initially, lipid suspensions (e.g., liposomes) would insert into disordered phases, a process facilitated by unsaturated/anionic phospholipids or by SP-B and SP-C [164]. Anionic phospholipids are believed to overcome the thermodynamic barrier of bilayer-monolayer approximation during the initial stages of LS adsorption, involving a non-cooperative process with SP-B and SP-C [165]. However, after the early film formation, SP-B likely assumes a pivotal role, contributing to approximately 75–80% of LS adsorption by facilitating the potential formation of a high-energy intermediate during adsorption. Subsequently, surfactant proteins would be excluded, promoting a flip-flop of lipids from bilayers to monolayers.

In terms of the surface characteristics of SP-C, its palmitoylation appears to be essential for effective surface activity, contributing to improved adsorption, enhanced film stability, efficient re-spreading during over-compression, and reduced film compressibility and hysteresis during dynamic cycling. [166], [167]. Interestingly, the optimal activity of SP-C-containing samples has been observed in films composed of the native phospholipid fraction of lung surfactant [168], not in DPPC/POPC or DPPC/POPG mixtures [169]. Moreover, it is widely accepted that cholesterol, at a certain concentration, significantly hinders the surface activity of LS concerning adsorption, re-spreading, and optimal functional properties during dynamic cycling [170], [171]. Nonetheless, interactions between SP-C and cholesterol have been associated with the compression-driven exclusion of fluid lipids from the interface. This aligns with the observation that palmitoylated versions of SP-C, particularly in combination with SP-B, demonstrate greater efficiency in mitigating the detrimental effects of cholesterol during dynamic cycling [170], [171], [172].

5.7 Immunomodulation of lung surfactants (relevant to Chapter 8)

Lung collectins, such as SP-A and SP-D, exhibit binding affinity to various microorganisms, encompassing Gram-positive and Gram-negative bacteria, fungi, yeast, viruses, and mite extracts [170]. The interaction between lung collectins and most microorganisms is thought to be facilitated by the carbohydrate recognition domain (CRD) regions. The lung collectins form associations with pathogens, leading to opsonisation, growth inhibition, and neutralisation. Opsonisation involves microbial agglutination, making these aggregates more easily recognisable by macrophages. Additionally, the lung collectins have a direct impact on the growth and viability of microbes. Recent research indicates that SP-A and SP-D can impede the growth of Histoplasma capsulatum yeast and certain Gram-negative bacterial strains by increasing the permeability of the microbial cell membrane [173], [174]. The interaction between the CRD of lung collectins and glycoconjugates on the microbial cell surface is deemed crucial for these effects, which occur independently of macrophage activity and microbial aggregation.

SP-A and SP-D collectins are involved in regulating the production of reactive oxygen and nitrogen intermediates in phagocytic cells, thus facilitating microbial clearance. The modulation of free radical release by lung collectins appears to be dependent on the types of microorganisms. SP-A enhances the killing of M. pneumoniae and Mycoplasma pulmonis by increasing nitric oxide production [175]. However, in macrophages primed with IFN-α, SP-A suppresses nitric oxide production by inhibiting TNF-α secretion and nuclear factor NF-κB activation [176], [177].

Pathogen-derived components, such as LPS, activate inflammation by interacting with pattern-recognition receptors [178]. SP-A and SP-D modulate the inflammatory response by interacting with CD14 or TLRs. Studies show that SP-A inhibits TNF-α expression induced by smooth LPS and reduces the production of proinflammatory cytokines [179], [180]. Conversely, SP-A fails to decrease the inflammatory response induced by rough LPS, suggesting the formation of the SP-A/CD14-rough LPS complex [181].

After considering all relevant data, it appears that lung collectins regulate inflammatory cellular responses in a manner that is dependent on their binding specificities and orientations towards various stimulants and cell surface receptors.

5.8 Conclusion

The efficient delivery of nebulised lung surfactants, reduction in surface tension of air-lung fluid interface within the alveoli, and modulation of inflammation that can potentially inactivate surfactants are the three fundamental pillars of a successful nebulised lung surfactant therapy in preterm neonates. Chapters 6, 7, and 8 of the present work present a triad of studies designed to explore the potential of microbubbles in treating neonatal respiratory distress syndrome (nRDS) by improving lung penetration, reducing surface tension, and modulating the immune response. In Chapter 6, the delivery efficiency of microbubble-laden aerosols was compared to conventional aerosols in a 3D-printed preterm neonate upper airway model. In Chapter 7, the effectiveness of microbubbles in reducing air-lung fluid interface was studied using a Langmuir-Blodgett Trough and compared to a suspension of lung surfactants. Finally, in Chapter 8, the immunomodulatory effect of microbubbles compared to lung surfactants was evaluated using LPS-induced macrophages to simulate a bacterial infection in preterm neonates. Overall, the results of these studies suggest that microbubbles may hold promise as a potential treatment option for nRDS.

Chapter 6 Microbubble-laden aerosols improve post-nasal penetration efficiency in a preterm neonate model

6.1 Introduction

There are estimated to be 13-15 million premature babies born annually across the globe [182] and despite increasing survival rates, preterm birth is still associated with high morbidity and mortality, in particular from respiratory distress syndrome (RDS). One of the most relevant interventions which has led to a significant increase in preterm infants´ survival is the introduction of animal-derived surfactant replacement therapy, which, together with antenatal steroids and the development of respiratory support, is the primary treatment for RDS [133], [183].

The current standard of care of providing mechanical respiratory support, oxygen therapy, and exogenous surfactants, however, is far from ideal [184], [185]. Iatrogenic consequences of the current treatment regimen have often led to the development of chronic lung disease [186]. Clinical research has therefore focused on reducing the use of mechanical ventilation, which is a significant risk factor for lung inflammation and the onset of broncho-pulmonary dysplasia (BPD) [187], [188]. As a result, less-invasive ventilation techniques are increasingly being explored as the primary RDS treatment [183], [189]. Less-invasive surfactant administration (LISA) was developed to avoid mechanical ventilation and to administer lung surfactant while preterm neonates spontaneously breathe. LISA, however, carries a high risk of complications such as surfactant reflux, acute desaturations, uneven delivery of surfactant to one side of the lungs, pneumothorax, and the need for mechanical ventilation [190].

Inhalation of lung surfactant has been proposed as a means of circumventing the main complications of intratracheal surfactant administration [191]. Several clinical studies have been conducted in which surfactant was nebulised to treat neonatal RDS [161], [192]. To date, however, the results have not been promising. For example, a recent Phase II study (NCT03235986) was terminated with the conclusion that insufficient surfactants were reaching the lungs [161].

Poor lung delivery is an inherent challenge in preterm neonates because of the narrow airways. Lung deposition percentages in premature neonates are very low, ~1% of the nominal dose [193], [194]. Neonates are preferential nasal breathers [195] because they have a disproportionately large tongue relative to the mouth, which creates a larger resistance in the oral cavity than the nasal airway. Thus, nebulised surfactants are administered via the nasal cavity. A preterm neonate's nasal cavity, however, is also not a favourable aerosol pathway for penetration into the lungs. Nasal conducting airways are tortuous and narrow, accounting for up to 50% of airway resistance [196], and this can further decrease with endogenous secretions [197] and accumulation of nebulised aerosol particles.

Nasal deposition of aerosols is primarily determined by inertial impaction [198]. Inertial impaction occurs when particles deviate from the air streamlines when there is an abrupt change in the direction of the flow. The particles' inertia causes them to collide with the airway walls and deposit there. The degree of nasal deposition is determined by factors such as the flow rate, particle characteristics (i.e., size and density), and airway characteristics (i.e., branching angle and airway diameter). Lung deposition can thus be improved by changing the flow rate and/or the particle characteristics.

A reduction in flow rate has been shown to improve lung deposition, as shown in various in vivo studies [20] and[199], [200]. The reduction in flow rate, however, can reduce oxygen supply to the lungs and thus can potentially reduce blood oxygenation level and create further complications. Moreover, the lungs of preterm neonates with RDS have low lung compliance, requiring a high positive pressure (or high flow rate for flow rate-controlled ventilators) for breathing [133]. Thus, reducing the flow rate for improved lung deposition is not likely to be a viable solution to enhance lung penetration of aerosols.

Reducing the size of aerosol particles has been shown to achieve improved lung penetration in neonates [194], [201], [202]. Vibrating mesh nebulisers (e.g., AeroNeb by Aerogen®), in particular, were successful in producing aerosol particles with a median mass aerodynamic diameter (MMAD) of 2.8 μm and achieved better lung deposition in macaque monkeys than a jet nebuliser which produced particles with MMAD = 4.6 μm). Deposition was 14.0 % vs 0.5 % for the AeroNeb and jet nebuliser, respectively. Unfortunately, however, this improvement in lung deposition was insufficient, to improve efficacy significantly in clinical trials [161], [192]. In the present study, we explore an alternative strategy for altering aerosol particle characteristics to improve delivery, specifically using gas microbubble-laden aerosols (Figure 6.1). Our hypothesis is that microbubbles should substantially reduce the effective density of the aerosol particles, thus reducing inertial impaction and nasal deposition and improving delivery to the lungs.

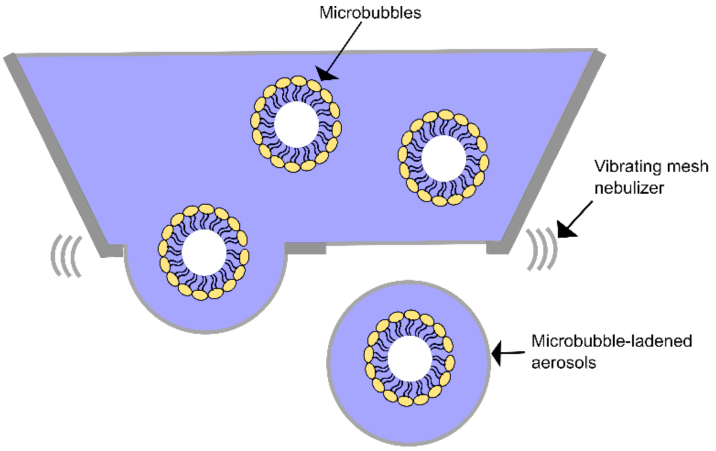

Figure 6.1. It shows the process of making microbubble-laden aerosols. Microbubble suspension is placed in the vibrating mesh nebuliser reservoir. The nebuliser produces aerosols containing microbubble(s).

6.2 Methods and materials

6.2.1 Materials

Dipalmitoylphosphatidylcholine (DPPC) and 1,2-Dipalmitoyl-sn-glycero-3-phosphoglycerol (DPPG) sodium salts were purchased from Avanti Polar Lipids, Inc. (Alabaster, AL, USA) as 25 mg/mL solutions in chloroform. Palmitic acid, sodium chloride, and chloroform were purchased from Sigma-Aldrich Company Ltd. (Dorset, UK). 8mL glass vials were purchased from VWR. Perfluorobutane was purchased from BOC Group plc, Woking, UK.

6.2.2 Lipid and microbubble suspension preparation

The microbubble formulation comprised DPPC, DPPG, and palmitic acid in 0.9 % w/v NaCl aqueous solution. The lipid film was first prepared. 8mg of DPPC (Avanti Polar Lipids, USA), 8mg of DPPG (Avanti Polar Lipids, USA), and 2mg of palmitic acid (Sigma Aldrich, UK) in chloroform (Sigma Aldrich, UK) were mixed in an 8 mL glass vial. The mixture was subsequently dried using a vacuum evaporator at 30 °C for 3 hours to allow chloroform to evaporate. The obtained dry lipid film was suspended in 8 mL of 0.9 % w/v NaCl aqueous solution (i.e., the lipid suspension has a DPPC concentration of 1 mg/mL or a total lipid concentration of 2.25 mg/mL) for 1 hour in a temperature-controlled shaker at 40 °C and 800 rpm. Lipids were then homogeneously dispersed for 180 seconds using a sonicator (Q125, QSonica, Newtown, CT, USA) at a power setting of 50 %, with the tip completely immersed in the lipid solution.

The resulting lipid suspension was then used to make microbubbles as follows: the sonicator tip was placed at the air-water interface under constant perfluorobutane (PFB) flow (The BOC Group plc, UK) and sonicated for 30 s at a power setting of 90 %. Immediately after the production, the headspace of the microbubble suspension vial was filled with PFB, capped and placed in ice.

The microbubble suspension was nebulised using Aerogen Pro (Aerogen®, Ireland) and collected into a vial via AAA-1 adapter (Vapotherm®, USA). The microbubble size characteristics were measured after nebulisation. For microbubble sizing and counting, the microbubble suspension was swirled, and 10 μL of the suspension was put onto a Neubauer-enhanced cell counting chamber (Hausser Scientific Company, USA) under a 24 mm by 24 mm glass coverslip (VWR International, USA). A CCD camera (MicroPublisher 3.3 RTV, QImaging, Canada) and a Leica DM500 microscope (Leica Microsystems GmbH, Germany) were used to image MBs at a magnification of 40. MATLAB® code, built explicitly for microbubble sizing and counting, was used (The Mathworks Inc., USA) [203].

6.2.3 HPLC method development for DPPC quantification

High-performance liquid chromatography (HPLC) was developed to quantify DPPC. DPPC was chosen because it is one of the major components of lung surfactant and is responsible for the highly ordered packing of lipids at the gas-liquid interface during the compression phase of the breathing cycle. The column temperature was kept at 30 °C (Column Oven, G7130A, Agilent Technologies, Inc., UK). The samples were kept at 4 °C. The injection volume was 1 µL (Sampler, G7129B, Agilent Technologies, Inc., UK). The column used was Luna C18 Column, 5 µm, 100 Å (Phenomenex®). The samples were dissolved in 50 % hexane and 50 % isopropanol. Mobile Phase A was 99.9 % methanol (Sigma Aldrich, UK) and 0.1 % formic acid (Sigma Aldrich, UK). Mobile Phase B was 99.9 % isopropanol (Sigma Aldrich, UK) and 0.1 % formic acid (Sigma Aldrich, UK). 1 mL/min flow was used (Pump, G7104A, Agilent Technologies, Inc., UK). 80 % Mobile Phase A and 20 % Mobile Phase B were used. A constant gradient was used, and the run finished at 5 min. The eluted components were detected by Evaporator Light Scattering Detection (ELSD - G4260B, Agilent Technologies, Inc., UK). The operational parameters were as follows: evaporator temperature = 85 °C, nebuliser temperature = 40 °C, and gas flow rate = 1.00 litres per minute. The output was processed: data acquisition rate = 80 Hz, smoothing = 30, and PMT Gain = 1.0.

6.2.4 Aerosol size characterisation

The droplet diameters of nebulised lipid suspension and microbubble suspensions were measured using an optical particle counter (OPC) called Alphasense N3 (Alphasense Ltd., 2019). The OPC was incorporated in Praxis Urban sensor system provided by South Coast Science Ltd. Measurement was made throughout the nebulisation of lipid suspension or microbubble suspension at 10-second intervals by the sensor system. The sensor (i.e., Alphasense N3) assumed that droplets are spheres and have a homogenous refractive index (RI) of 1.5. This closely matches the refractive index of DPPC monolayer on an air-water interface (RI = 1.485) [204].

Laser diffraction technique is commonly used in particle size analysis equipment that is used to measure particle sizes of pressurised metered-dose inhalers (pMDI), dry powder inhalers (DPI), and soft mist inhalers [205], [206]. This technique is highly effective in measuring droplet sizes of nebulised lipid suspension. Aerodynamic diameter, which is defined in the equation below, for the nebulised lipid suspension was then calculated.

$$D_a = D_g \times \sqrt{\frac{\rho_p}{\rho_0 \chi}} \qquad \text{Equation 6.1}$$

D_a is the aerodynamic diameter. D_g is the geometric diameter, which is the measurement from the OPC. ρ_p is the density of the nebulised aerosol (or particle). ρ_0 is the unit density. χ is the shape factor, which, in the case of nebulised lipid suspension, is assumed to be spherical and thus has a value of 1.

However, it should be noted that OPC may not provide precise measurements for aerosols containing microbubbles because of their non-uniform refractive index, resulting in multiple interfaces where the refractive index fluctuates. As a result, the aerodynamic diameter of microbubbles was calculated based on the particle size distribution of nebulised lipid suspension and the microbubble size distribution of nebulised microbubble-laden aerosols.

The calculation of the aerodynamic diameter of microbubble-laden aerosols was conducted according to the following process. Initially, the proportion of aerosols containing microbubbles was determined. By utilising a light microscope (as referenced in section 6.2.2), the quantity of microbubbles present in 1 mL was measured. Based on the OPC measurements, the quantity of lipid aerosols in 1 mL was estimated to be 8.8×10^9. It was assumed that only a single microbubble was incorporated into each aerosol, if at all. This assumption was supported by the fact that there were more aerosols than microbubbles, and the aperture's size restriction (i.e., 2.5 μm) minimised the likelihood of more than one microbubble being incorporated into a single aperture.

Additionally, it was assumed that the geometric diameters (D_g) of microbubble-laden aerosols were equivalent to those of the nebulised lipid suspension. This assumption was based on the vibrating mesh nebuliser's characteristics, whereby the size of nebulised aerosols is predominantly determined by the mesh hole size [207]. Viscosity and ion concentration, which are factors that affect aerosol size, were found to be consistent between the lipid suspension and the microbubble suspension [208]. As a result, it was concluded that the microbubble-laden aerosols possess the same geometric diameter distribution as the lipid suspension aerosols.

In order to utilise the lipid aerosol's particle size distribution, it was initially fitted to a log-normal distribution. This distribution was then used to select a diameter at random for the microbubble-laden aerosol. This random selection process created particle sizes that had not existed in the dataset of the nebulised lipid suspension. In instances where the randomly selected particle diameter fell below 0.8 μm, it was disregarded. Similarly, the microbubble diameter data was also fitted to a log-normal distribution, and a microbubble diameter was randomly assigned based on the log-normal distribution of the microbubbles.

Next, the calculation of the mass of microbubble-laden aerosols was performed. The density of PFB gas is 11.78 kg/m3, and it was assumed that the interfacial tension between the DPPC monolayer and PFB is negligible, disregarding the effect of inward pressure on the density of PFB [209]. The mass and volume of the microbubble monolayer were excluded from the mass calculation as they are insignificant compared to the aerosol and microbubble size. The mass of the different components of the microbubble-laden system, such as the aqueous droplet and PFB gas core, was summed and divided by the geometric diameter of the aerosol to determine the particle density (ρ_p). Finally, the aerodynamic diameter of microbubble-laden aerosols was calculated using Equation 6.1.

6.2.5 Development of preterm neonate nose-throat model

A preterm simulator (Paul, Sim Characters GmbH) was used to build a preterm neonate nose-throat model. Paul is a highly realistic preterm simulator whose upper airways are a 3D printout of a three-planar magnetic resonance imaging (MRI) scan of a 27 gestational week baby. The baby was approximately 1,000 g in weight and 35 cm in length. The model has undergone smoothing of chonchae nasalis.

The preterm neonate airway 3D printout model for this study was developed in three phases: i) first, a high-resolution computed tomography (CT) scan was performed on Paul (Sim Characters GmbH) (imaging phase); ii) second, the nose-throat model was constructed using three dimensional (3D)-printing (ProJet MJP 2500, 3D Systems, Inc.) and a photopolymer termed VisiJet M2R (3D Systems, Inc.) (construction phase); iii) third, the nose-throat model is printed in halves and the heights of the airways are compared to the 3D image at different points.

A CT scan (Siemens SOMATOM Drive, John Radcliffe Hospital, Oxford University Hospital, Oxford, UK) was performed on the airway model (voltage: 100 kV, current: 225 mA) with a slice thickness of 0.5 mm. The Paul model was lying in a supine position. The volume of pixel (voxel) dimensions for the acquisition was 0.2246 mm by 0.2246 mm by 0.5 mm. Optimal negative and positive grayscale thresholds were selected for the original CT scans, stored as Neuroimaging Informatics Technology Initiative (NIfTI), to provide maximal accuracy of air-solid distinction. For the binary segmentation, the threshold of Hounsfield unit was set at 0 (where negative values represented the airways). The slices were joined together to compose a 3D reconstruction image using MATLAB (MathWorks, Inc.), which was stored in Standard Transformation Language (STL) format. The STL file underwent further surface smoothing using MeshLab (ISTI-CNR). Additional support and aerosol deposition parts were added using Autocad (Autodesk, Inc.). The preterm model was then printed using a 3D printer (ProJet MJP 2500, 3D Systems, Inc.) and a photopolymer named VisiJet M2R (3D Systems, Inc.).

The aerosol delivery efficiency to the lungs was evaluated by passing the nebulised aerosols through the preterm nose-throat airway model, which included the nose, pharynx, larynx, and about 3/4 of the trachea before a low-volume filter housing was connected. The resulting preterm airway, shown in Figure 6.2A, has a tracheal length and diameter of 23.45mm and 2.93mm, respectively. It agreed well with the literature, where tracheal length and diameter for 27 weeks gestational age are approximately 23mm and 3mm, respectively [210]. The measured dimensions fall within the range for “very” preterm neonates (i.e., 26 to 32 weeks of gestational age), and thus the 3D-printed cast was deemed acceptable [210].

MultiJet printing technology provided an accurate internal airway surface and the preterm model's middle passage and throat sections. Airway diameters of the 3D printed cast were measured using callipers and were compared to the computer 3D model. The difference between the cast and the computer model was always less than 0.1mm at any point in the airway.

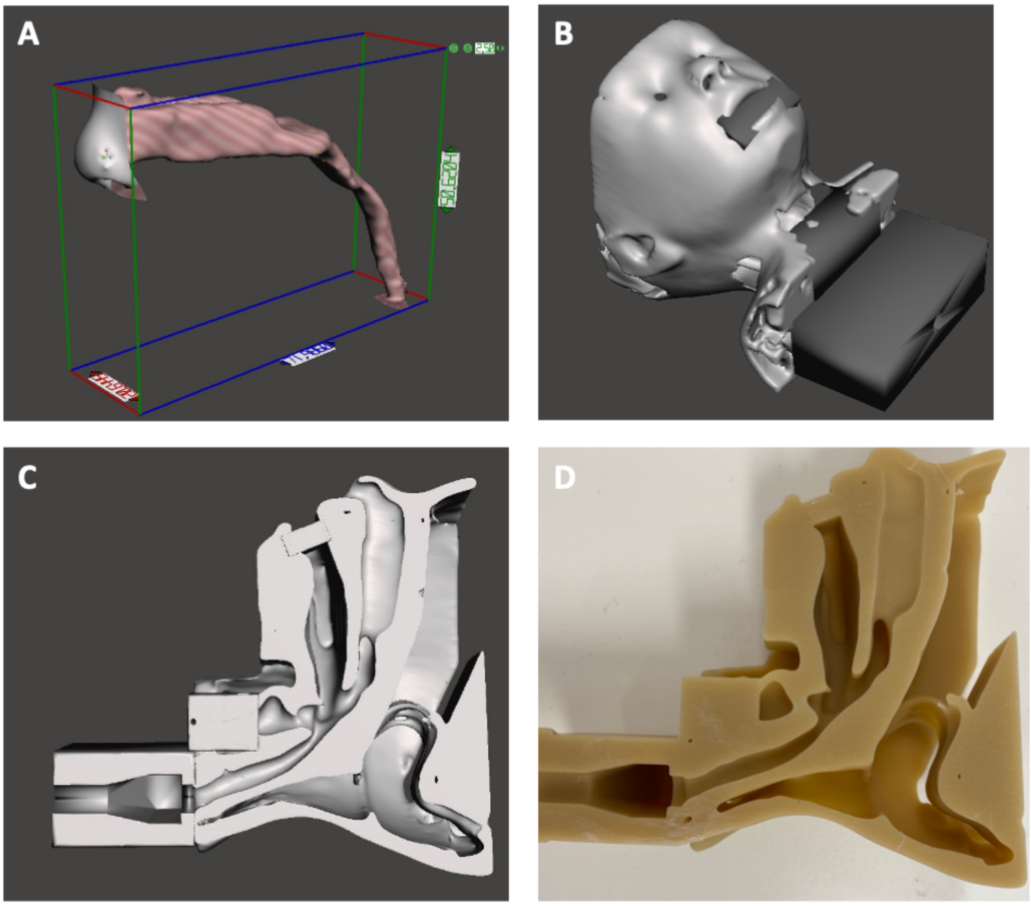

Figure 6.2. (A) Extracted air conducting parts of CT scan of the cast. (B) Side view of the complete upper airway model. (C) A selected sagittal cross-section through the upper airway model (B). (D) 3D Printed version of (C). The printout was made using 3D printing (ProJet MJP 2500, 3D Systems, Inc.).

6.2.6 Aerosol deposition in the preterm neonate nose-throat model

The in vitro set-up consisted of a high-flow nasal cannula (HFNC) system (Vapotherm Precision Flow, Vapotherm®), a cast of a premature infant's upper airways (nose and throat), a premature nasal cannula (MN1100A, Vapotherm®), and surfactant collection filters (PARI Filter PAD). This simulated the clinical setting in which surfactants are nebulised and delivered to preterm neonates. The nose-throat cast for the preterm neonate was positioned between the outlet from the Vapotherm Precision Flow (Vapotherm®) and the nasal prongs. The connection to the airflow was made using an AeroNeb Aerosol Adaptor (FDD 5631, Vapotherm®). The prongs were wrapped with PTFE tapes to ensure a tight connection between the cast and the prongs. The apparatus was thoroughly examined for air leaks. The HFNC system's temperature was 37 °C, and the relative humidity was 100%. Aerosol deposition in the 3Dprinted cast was studied at three different flow rates (4, 6, and 8 L/min).

A volume of 2 mL of either the lipid or the microbubble suspension (equivalent to 1 mg/mL of DPPC) was loaded into the nebuliser reservoir and was continuously nebulised. Surfactant collection filters were placed at the distal airway of the model ("aerosol collector" in Figure 6.3). Any nebulised suspension material that did not reach the 3D-printed model was collected in a vial and re-nebulized. This step was repeated until all the suspension was nebulised and reached the 3D-printed model. Re-nebulization ensured that the suspensions were not wasted in the nebuliser connector. In the clinical setting, the re-nebulization of the wasted lipid or microbubble suspension in the connection is not feasible, thereby necessitating the implementation of improved nebuliser connection designs to minimise wastage.

The lung penetration efficiency of the aerosol or post-nasal aerosol penetration was defined as the percentage of aerosol particles collected in the filter placed at the distal airway of the preterm neonate upper airway cast (In-Filter) divided by the total amount of surfactant that was nebulised. A backup trap (i.e., liquid collector) was attached to the cast to collect the aerosols deposited in the cast. 3 mL of distilled water was used as the rinsing solvent to recover deposited aerosols in the 3D printed preterm model. This was repeated four times, and a total of 12 mL of distilled water was used to rinse out deposited aerosols on the 3D-printed cast. 3 mL of isopropanol was used to recover the surfactant from the aerosol collector compartment of the set-up. This was repeated four times, and a total of 15 mL of isopropanol was used to rinse out DPPC deposited on the filter. The filter held on to approximately 1 mL of isopropanol, and thus, 14 mL of isopropanol was collected in total. The rinsed samples were dried and then reconstituted with 50 % v/v hexane and 50 % v/v isopropanol mixture.

The dried samples from the aerosol collector were dissolved in 0.5 mL of the organic solvent mixture, and the samples from the 3D printed model were dissolved in 2 mL of the organic solvent mixture. The amount of the main active constituent, i.e., DPPC, was determined as a lead compound to quantify deposition in the nasal airway region. The retrieval efficiency of the rinsing method was measured by adding a known amount of the lipid suspension (i.e., 1 mL of 1 mg/mL), and the amount of DPPC retrieved during the rinsing step was measured using HPLC.

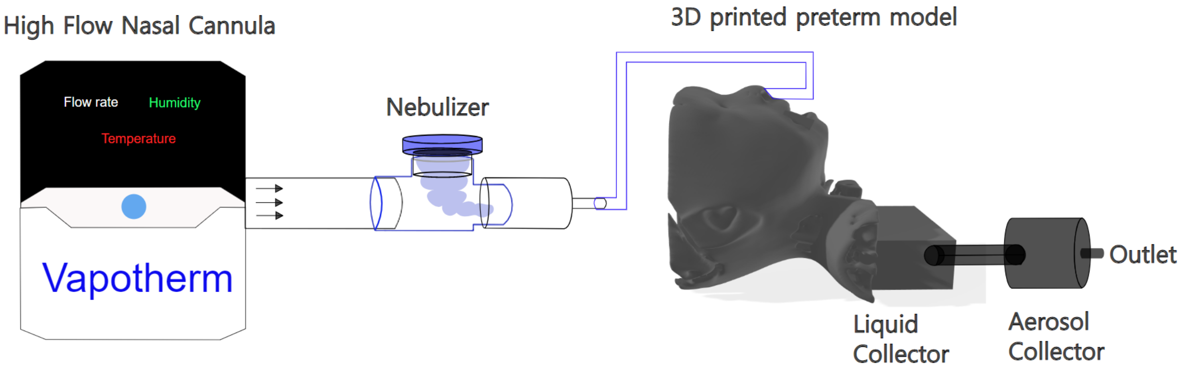

Figure 6.3. The in vitro set-up replicates the clinical setting, where a high-flow nasal cannula (HFNC) delivers oxygen/air into preterm neonates via the nose, and a nebuliser produces aerosols, which are then delivered to the preterm neonates. The preterm model is 3D printed from a CT scan of a preterm neonate with 27 weeks gestational age. The liquid collector collects any aerosol particles deposited in the nose-throat region, and the aerosol collector collects particles entering the lungs.

6.3 Results and discussion

6.3.1 HPLC method development for DPPC quantification

The formulation used in this study comprises DPPC, DPPG, and palmitic acid. An HPLC method was developed to separate DPPC from palmitic acid and DPPG and then quantify the proportion of DPPC. It was found that DPPG, palmitic acid and DPPC eluted at 0.65 (± 0.1) min, 2.1 (± 0.1) min, and 3.6 (± 0.1) min (Figure 6.4). Peaks did not overlap in the concentration range of interest in this study (i.e., 0.2 to 1.0 mg/mL of DPPC). No peaks were found in blank samples, and no carryover was detected. The calibration curve showed good linearity (i.e., $R^2 = 0.9951$) in the 0.2 – 1.0 mg/mL range when injecting 1 μL Figure 6.4 (A).

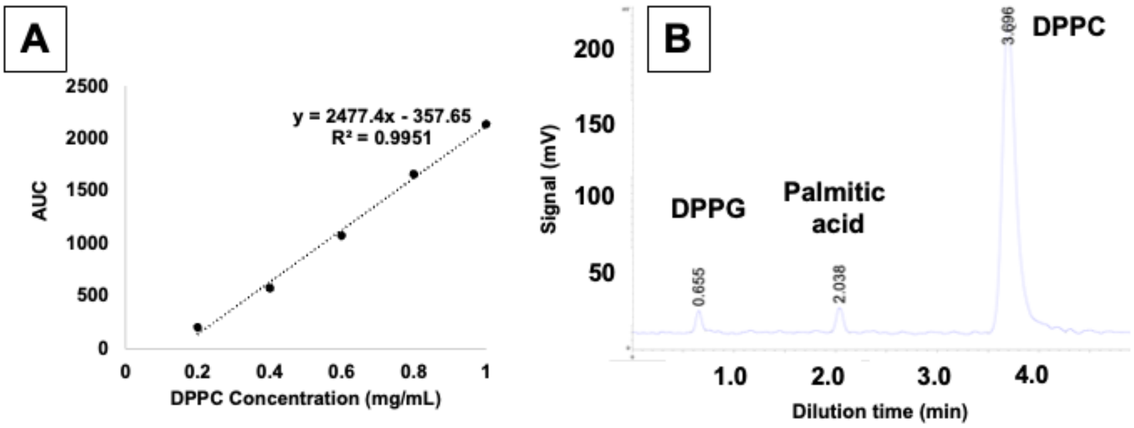

Figure 6.4. (A) Linearity Curve for DPPC. (B) Chromatograms of DPPC:DPPG:Palmitic acid (1:1:0.25 mg/mL, respectively) dissolved in hexane/isopropanol solvent mixture.

6.3.2 Characterisation of microbubble-laden aerosols and nebulised lipid suspension aerosols

The Aerogen Pro (Aerogen®) was used to nebulise microbubbles, which were then collected in a vial for microbubble sizing. The bubble size distribution and number were measured (Figure 6.5). The microbubbles had a concentration of 3.32×10^9 MBs/mL and a median diameter of 1.52 μm. The data was subsequently used to calculate the aerodynamic diameter of microbubble-laden aerosols.

Using OPC measurements, we calculated the aerodynamic diameter of microbubble-laden aerosols and nebulised lipid suspension. The resulting histogram (shown below) was fitted to a log-normal distribution (Figure 6.6). The solid red line represents the log-normal distribution of microbubble-laden aerosols, which peaked at 1.25 μm. The log-normal distribution of nebulised lipid suspension peaked at 1.75 µm. These findings suggest that incorporating microbubbles in the aerosols reduced the aerodynamic diameter. Additionally, we observed a significant increase in the number of aerosols with an aerodynamic diameter of less than 1 µm in microbubble-laden aerosols.

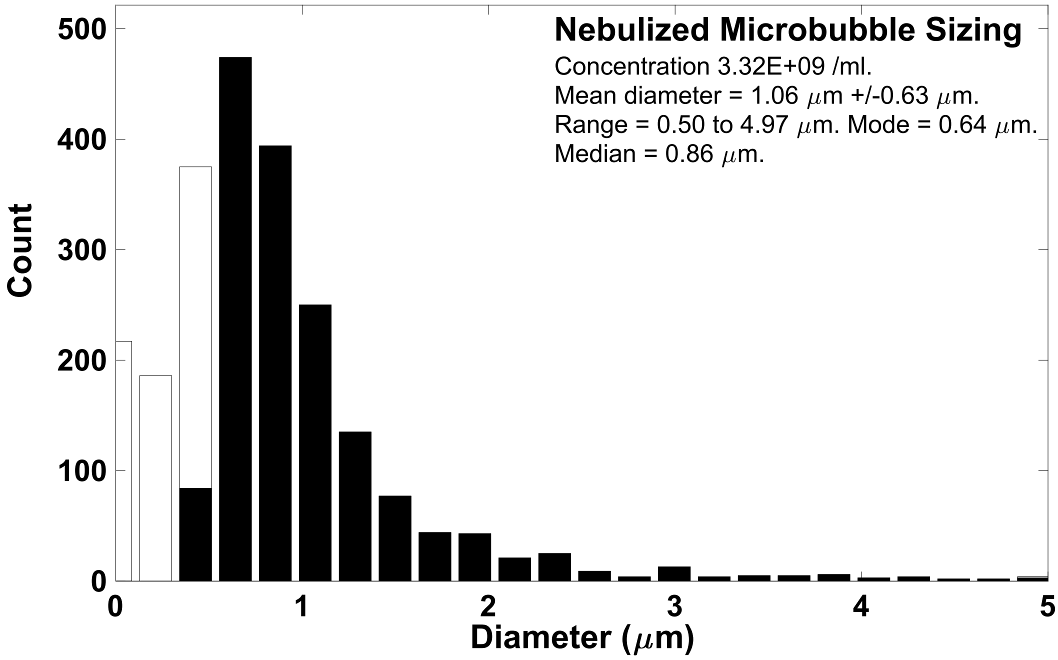

Figure 6.5. The size of microbubbles in the nebulised microbubble suspension. The white boxes in the image indicate microbubbles smaller than 0.5 µm. These were excluded from the count due to the light microscope's inability to measure them [203]. The black boxes show the histogram of microbubble counts in the haematocytometer.

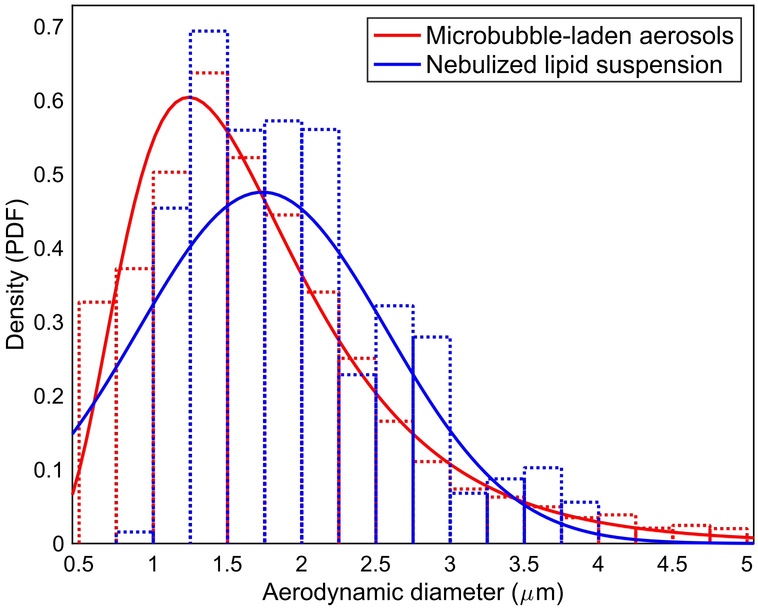

Figure 6.6. The aerodynamic diameters of microbubble-laden aerosols (red) and aerosolised lipid suspension (blue) are shown. Dotted lines represent the histogram, and the solid line represents the log-normal distribution that is fitted to the data. The x-axis represents the aerodynamic diameter (µm), and the y-axis is probability density. Each bin has a width of 0.25 µm.

6.3.3 Post-nasal aerosol penetration efficiency

The rinsing method for the 3D-printed cast retrieved 100.0 % of the DPPC that was used in the experiment, and the method had a standard deviation of 4.6 %. The retrieval efficiency for the aerosol collector was 46.7 %, with a standard deviation of 7.3 %. This suggested that DPPC strongly adsorbed to the filter in the aerosol collector. Due to a lack of alternative materials for the filter, it was decided that the retrieval efficiency of the rinsing method would be considered when calculating the amount of DPPC deposited in the aerosol filter.

Microbubble-laden aerosols were found to have greater lung penetration efficiency than nebulised lipid suspension (Figure 6.7). 0.05 mg/mL (or 0.025 mg for the aerosols collected in the filter) was the limit of detection (LoD) for the HPLC method used in this study. Lung penetration below 1.25 % of the aerosolised DPPC was not detected by the HPLC. It was found that the lung penetration for the aerosolised lipid suspension was less than 1.25% at all three flow rates (4, 6, and 8 L/min). On the other hand, the amount of DPPC collected in the filter for microbubble-laden aerosol was significantly higher than that of aerosolised lipid suspension. They were 30.0 %, 25.5 %, and 17.5 % at 4 L/min, 6 L/min, and 8 L/min, respectively (Figure 6.7).

It is widely recognised that aerosols with smaller aerodynamic diameters can reduce nasal deposition in preterm infants and improve lung penetration [211], [212], [213]. Previously, it was believed that aerosols with an aerodynamic diameter of 2 μm or less were necessary for them to penetrate the nasal airways and enter the lungs of preterm neonates [213]. However, increasing evidence suggests that the critical maximum threshold may be less than 2 μm [211], [214]. Clinical studies that administered nebulised lung surfactants with a median mass aerodynamic diameter (MMAD) of 1.9 μm did not show clinical efficacy in treating nRDS [161], [192]. In 2022, Dani et al. [161] suggested that a lower aerodynamic diameter of 1.4 μm is required to reach the lungs of preterm infants. This conclusion was based on the observation that the exhaled aerosols from preterm infants had an MMAD of 1.4 μm, indicating that the aerosols had entered the lungs and that the fraction that had not deposited in the lungs was exhaled.

It appears that post-extrathoracic aerosol penetration is determined by the number of aerosols that are less than 1 μm in aerodynamic diameter. For flow rates that are clinically relevant (4 – 8 L/min), 1 μm may be the critical maximum threshold for preterm neonate lung delivery. In this experiment on the 3D-printed preterm model, nebulised lipid suspension, which had a minuscule number of aerosols that were less than 1 μm, failed to penetrate, whereas microbubble-laden aerosols, which contained a dramatically higher number of aerosols that are less than 1 μm, showed higher penetration in the 3D-print model. This is in line with other in vitro and in silico studies, which suggest that aerosols with aerodynamic diameters less than 1 μm are less likely to deposit in the preterm nasal-throat model [211], [214].

The flow rate range was selected from 4 L/min to 8 L/min to reflect the flow rate used in the clinics. 8L/min is the initial flow rate when the lung surfactants are administered, and it gradually decreases to 4 L/min with an improvement in blood oxygen saturation. Thus, three different flow rates (4, 6, and 8L/min) were studied. It was found that deposition decreases with an increase in flow rate. This was expected because the increase in flow rate increases inertial impaction in the nose-throat airways, reducing lung delivery efficiency.

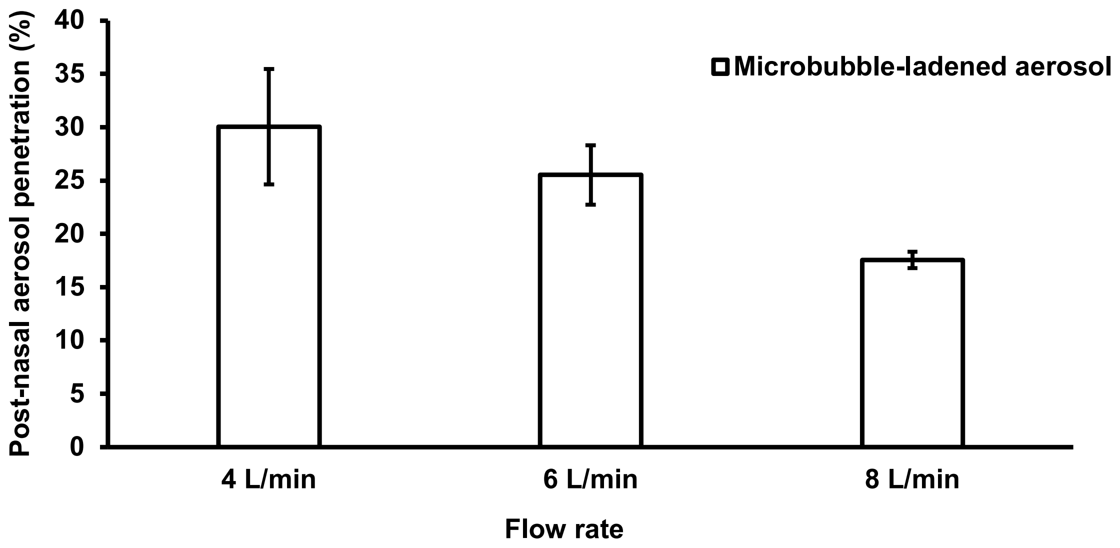

Figure 6.7. The percentage of DPPC that penetrated the extrathoracic region and entered the collector is shown. Three different rates were studied (4, 6, and 8 L/min). The limit of detection (LoD) for the HPLC method was 0.05 mg/mL (or 1.25 % of the aerosolised lipid suspension). Post-natal aerosol penetration for nebulised lipid suspension was all below LoD and thus was not included in the figure.

6.3.4 Limitations

Surface smoothing occurs as a result of surface irregularities caused by low-resolution CT or MRI scans and poor interpolation between consecutive cross-sections in sectional anatomic data. This, in turn, reduces particle deposition in the 3D-printed nasal cavity models [215]. However, the 3D-printed nasal casts have an increased wall roughness compared to the human nasal cavity, which is lined with nasal fluid. This roughness leads to an increase in particle deposition in the nasal cavity [216], thus counteracting the reduction in particle deposition due to surface smoothing. Therefore, there may be some margin of error with the 3D-printed model compared to the human preterm nasal deposition. Nonetheless, for the purposes of this study that compares the relative change in nasal deposition after incorporating microbubbles in aerosols, the 3D-printed model is deemed appropriate.

Due to the limited availability of clinical scans of preterm neonates, this study only used a single preterm nose-throat model, so the effects of inter-subject variability in the upper airway dimension and the change in airway size with the gestational period could not be investigated.

6.4 Conclusion

In conclusion, a microbubble-laden aerosol was compared to conventionally aerosolised lipid suspension for lung delivery efficiency in a 27 gestational weeks-old preterm neonate model. Microbubble-laden aerosols had higher lung delivery efficiency than conventionally nebulised aerosols. Microbubble-laden aerosols may improve lung delivery of nebulised lung surfactant in preterm neonates, thus potentially improving treatment outcomes in nRDS.

Chapter 7 Microbubbles for lung surfactant therapy

7.1 Introduction

11% of neonates are born before 37 weeks of gestation, resulting in an estimated 13 – 15 million premature babies per year globally. Preterm birth, despite improvements in management, is the leading cause of infant morbidity and mortality, and neonatal respiratory distress syndrome (nRDS) remains one of the main challenges in neonatology.

Neonates with nRDS are characterised by poor lung function, such as low functional residual capacity (FRC) and low lung compliance [217]. Poor lung function creates poorly ventilated lung regions and subsequently activates a compensatory mechanism to shunt blood perfusion from poorly ventilated regions of the lungs to well-ventilated regions. In nRDS, however, vasoconstriction of the compensatory mechanism increases the risk of cerebral and pulmonary haemorrhage and ventilation-perfusion mismatch due to increased blood pressure in the upstream pulmonary arteries [133]. The ventilation-perfusion mismatch increases the risk of hypoxemia and may cause developmental disabilities such as cerebral palsy.

High surface tension in the air-aqueous interface in alveoli and small airways is the leading factor causing nRDS [218]. High surface tension in these regions means that higher air pressure is required to increase lung volume. High air pressure, in turn, increases the recoil pressure of airways and increases the risk of airway collapse upon exhalation. Histological studies in surfactant-deficient rabbits have shown that the amount of damage is related to the magnitude of changes in airway pressure [219]. Poorly supported respiratory bronchioles and alveolar ducts in preterm neonates are particularly vulnerable to collapse [220]. Higher pressures can also cause over-distension of well-ventilated regions of the lungs, which further decreases lung compliance. Furthermore, airway closures can cause infiltration of proteins and/or a build-up of fluid, resulting in low functional residual capacity (FRC).

Less-invasive surfactant administration (LISA) is increasingly becoming the main standard of treatment for the early onset of nRDS [221]. LISA was developed to avoid the use of mechanical ventilation and to administer lung surfactant while preterm neonates are spontaneously breathing. It involves laryngoscopy and introducing a thin, soft catheter into the larynx and the trachea. LISA has been shown to reduce the need for mechanical ventilation, but it is a high-risk procedure requiring neonatologists experienced in airway management and still carries a high rate of side effects and complications [222]. Without correct manipulation, it leads to complications such as surfactant reflux, acute desaturations, uneven delivery of surfactant, and pneumothorax, eventually leading to the need for mechanical ventilation.

Inhalation of lung surfactant at birth could hypothetically circumvent the main complications of intratracheal surfactant administration, such as uneven distribution of lung surfactants and surfactant reflux. It can potentially deliver surfactants directly to the respiratory bronchioles and alveolar ducts, improving short and long-term outcomes of preterm babies [223]. Conventionally nebulised surfactants fail to reach the lungs and deposit on the narrow airways in the extrathoracic region [194], [199]. In a recently terminated Phase II study (NCT03235986), nebulised poractant alfa failed to show efficacy [161]. This was attributed to an insufficient amount of surfactant reaching the lungs. Poor lung delivery appears to be an inherent drug delivery barrier in preterm neonates because of narrow extrathoracic airways and the high flow rate required to achieve oxygenation (approximately at 8L/min) [198].

Microbubbles, consisting of a gas core surrounded by a surfactant or lipid coating, may offer a potential solution to this problem. As discussed in Chapter 6, microbubbles have been found to significantly enhance lung penetration of aerosols in preterm neonates, as demonstrated in the 3D-printed preterm neonate model. Microbubbles may also be effective in reducing the surface tension of the air-aqueous interface. The ability of microbubbles to transfer lipids to other lipid membranes (e.g., cellular lipid bilayer and artificial lipid layers) has previously been reported [224], [225]. The exact mechanism of the transfer is unknown, but the published results suggest that microbubbles may have the ability to improve the adsorption of phospholipids on the air-aqueous interface and thus achieve low surface tension even with small amounts of phospholipids.

In this study, we hypothesised that incorporating microbubbles into aerosols used for nRDS treatment could improve phospholipid deposition as follows: first, aerosol droplets with aerodynamic diameters below 2 μm [194] will deposit onto the lower side of the airways by sedimentation due to gravity (Figure 7.1A). Microbubbles, which have a lower density than water, will float to the upper air-aqueous interface of the deposited droplets (Figure 7.1B). This subsequently results in clusters of microbubbles resting near the phospholipid monolayer on the air-aqueous interface (Figure 7.1C). The inherent instability of microbubbles was speculated to facilitate better transfer of phospholipids and reduction of air-aqueous surface tension. To test this hypothesis, the effect of phospholipid-coated microbubbles on the surface tension of air-aqueous interfaces was studied.

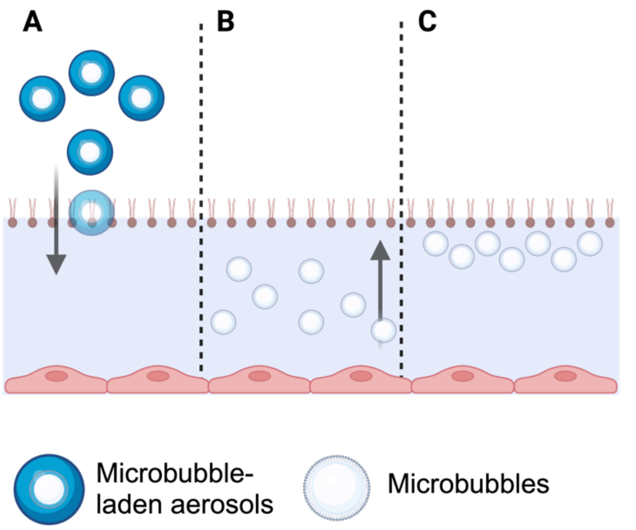

Figure 7.1. A schematic diagram depicts the hypothesised process by which microbubbles interact with the phospholipid monolayer at the air-aqueous interface. (A) Microbubble-laden aerosols deposit in the lung lining fluid by sedimentation. Microbubbles float to the air-aqueous interface of deposited droplets (B), resulting in clusters that may reduce surface tension (C). The effect of phospholipid-coated microbubbles on air-aqueous interface surface tension was studied. The diagram is not drawn to scale.

7.2 Methods and Materials

7.2.1 Materials

Dipalmitoylphosphatidylcholine (DPPC), 1,2-Dipalmitoyl-sn-glycero-3-phosphoglycerol, sodium salt (DPPG) was purchased from Avanti Polar Lipids, Inc. (Alabaster, AL, USA) as a 25 mg/mL solution in chloroform. Polyoxyethylene (40) stearate (PEG-40S), sodium chloride, palmitic acid, propylene glycol, and chloroform were purchased from Sigma-Aldrich Company Ltd. (Dorset, UK) as a powder. Poractant alfa (Curosurf®) was purchased from Chiesi Limited, Manchester, UK. An 8mL glass vial was purchased from VWR. Perfluorobutane was purchased from BOC Group plc, Woking, UK.

7.2.2 Microbubble preparations

Three different types of microbubbles were produced (Figure *7.2*). The first microbubble, shown in Figure *7.2*A, was formulated with PEGylated lipid (i.e., PEG40-S), and this is referred to as PEGylated microbubbles. PEGylated microbubbles were formulated and prepared based on previous literature [226] and were known to produce stable microbubbles. In a feasibility study on a clean air-aqueous interface, PEGylated microbubbles were employed to investigate their influence on the surface tension of the interface.

Poractant alfa, which failed to show clinical efficacy at low concentrations [161], was formulated into microbubbles (Figure *7.2*B). A study on a clean air-aqueous interface was conducted to examine how the surface tension-lowering ability of poractant alfa could be enhanced by formulating it in microbubbles. Lastly, a microbubble formulation without PEGylated lipids was made and is referred to as PEG-free microbubbles (Figure *7.2*C). PEG-free microbubbles were formulated to avoid potential hypersensitivity to PEG [227] and the use of excipients that are not naturally present in preterm neonates. PEG-free microbubbles were tested for their surface activity in a simulated lung condition.

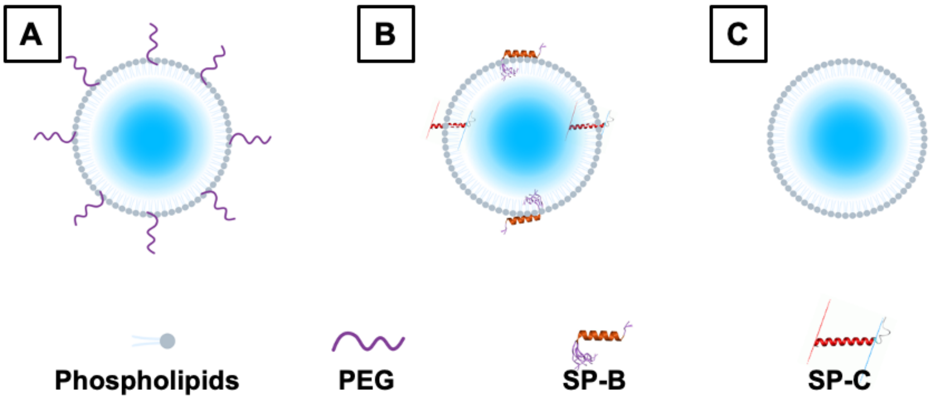

Figure 7.2. Three different types of microbubbles were produced. The first on the left (A) is a PEGylated microbubble consisting of phospholipids, PEGylated lipids, and a gas core. In the middle (B) is a microbubble composed of poractant alfa, which may contain SP-B and SP-C proteins. Lastly, (C) represents a PEG-free microbubble composed of phospholipids, lipids, and a gas core.

The PEGylated microbubble was composed of DPPC (Avanti Polar Lipids, USA) and PEG40-S (Sigma Aldrich, UK), dissolved in chloroform (Sigma Aldrich, UK). They were mixed in an 8 mL glass vial at a molar ratio of 9:1 (DPPC:PEG40-S). Six milligrams of DPPC (or 240 μL of 25 mg/mL) and 1.86 mg of PEG40-S (or 74.4 μL of 25 mg/mL) were measured into the vial. The mixture was subsequently dried using a vacuum evaporator at 30 ºC for 3 hours to allow for chloroform to evaporate. The obtained dry lipid film was suspended in 3 mL of 0.9 % w/v NaCl aqueous solution for one hour in a temperature-controlled shaker at 60 ºC and at 800 rpm. Lipids were then homogeneously dispersed for 60 s using a sonicator (Q125, QSonica, Newtown, CT, USA) at a power setting of 50 % with the tip completely immersed in the lipid solution. This was the DPPC/PEG40-S lipid suspension.

The DPPC/PEG40-S lipid suspension was subsequently used to make microbubbles. The sonicator tip was placed at the air-aqueous interface under constant perfluorobutane (PFB) flow (The BOC Group plc, UK) and sonicated for 30 s at a power setting of 90 %. Immediately after production, the vial containing the MB suspension was capped and placed on ice until use. Microbubbles were used within 15 minutes of production.

For the 'washed' DPPC/PEG40-S microbubbles, the microbubble suspension was centrifuged at 500 g for 15 mins and the subnatant was discarded and the microbubble cake was re-suspended in 3 mL of 0.9 % w/v NaCl aqueous solution. This process was repeated three times, and the final suspension was re-suspended in 3 mL of 0.9 % w/v NaCl aqueous solution.

To manufacture poractant alfa containing microbubbles, poractant alfa was diluted to 5.3 mg/mL using 0.9 % w/v NaCl aqueous solution up to 3 mL in an 8 mL vial. Lipids were then homogeneously dispersed for 20 s using a sonicator (Q125, QSonica, Newtown, CT, USA) at a power setting of 50 % with the tip completely immersed in the lipid solution. The obtained solution was placed in a temperature-controlled shaker at 35 ºC and at 800 rpm. The sonicator tip was placed at the air-aqueous interface and sonicated for 30 s at a power setting of 90 %. The headspace of the 8 mL vial was filled with air. Immediately after production, the vial containing the MB suspension was capped and placed on ice.

The PEG-free microbubble formulation was composed of DPPC, DPPG, and palmitic acid in 20 % w/w propylene glycol in 0.9 % w/v NaCl aqueous solution. This formulation was developed to exclude PEGylated lipids from the formulation. The lipid film was first prepared. 8 mg of DPPC (Avanti Polar Lipids, USA), 8 mg of DPPG (Avanti Polar Lipids, USA), and 2mg of palmitic acid (Sigma Aldrich, UK) in chloroform (Sigma Aldrich, UK) were mixed in an 8 mL glass vial. The mixture was subsequently dried using a vacuum evaporator at 30 ºC for 3 hours to allow for chloroform to evaporate. The obtained dry lipid film was suspended in 4 mL of 20 % w/v propylene glycol in 0.9 % w/v NaCl aqueous solution (i.e., the lipid suspension has a DPPC concentration of 2 mg/mL or a total lipid concentration of 4.5 mg/mL) for 1 h in a temperature-controlled shaker at 60 ºC and at 800 rpm. Lipids were then homogeneously dispersed for 60 s using a sonicator (Q125, QSonica, Newtown, CT, USA) at a power setting of 50 % with the tip completely immersed in the lipid solution. The lipid suspension was further diluted by 8 times using 20 % w/w propylene glycol in 0.9 % w/v NaCl aqueous solution to make a DPPC concentration of 0.25 mg/mL or a total lipid concentration of 0.5625 mg/mL. This is referred to as PEG-free lipid suspension.

The PEG-free lipid suspension was subsequently used to make microbubbles. The lipid suspension was first de-gassed, and then PFB gas was added to the headspace. CapMix (3M, UK) was used to make the microbubbles by shaking method. The speed was set at 4,300 rpm and was shaken for 15 seconds. Immediately after production, the vial containing the microbubble suspension was capped and placed on ice.

For microbubble sizing and counting, 10 µL of the microbubble suspensions were put onto a Neubauer-enhanced cell counting chamber (Hausser Scientific Company, USA) under a 24 mm by 24 mm glass coverslip (VWR International, USA). A CCD camera (MicroPublisher 3.3 RTV, QImaging, Canada) and a Leica DM500 microscope (Leica Microsystems GmbH, Germany) were used to image MBs at a magnification of 40. MATLAB® code that was built explicitly for microbubble sizing and counting was used (The Mathworks Inc., USA) [203].

7.2.3 Creating a physiologically relevant air-aqueous interface to model nRDS

Lung lining fluid comprises various salts, surfactants, cells, and proteins. Out of the numerous components, salt composition, surfactants, and surfactant proteins play crucial roles in determining the surface tension of the air-aqueous interface. In this study, a physiologically relevant air-aqueous interface for nRDS was created. Gamble's solution [228] was used as the aqueous subphase to replicate the salt composition. Poractant alfa was used to replicate the amount of surfactant and surfactant proteins and the surface tension on the air-aqueous interface.

The quantity of poractant alfa added to the air-aqueous interface was selected based on previous studies. Stichtenoth et al., 2014 reported that the amount of phosphatidylcholine for preterm neonates born before 32 weeks of gestation could be as low as 0.04 mg/mL, and the surface tension at the initial adsorption was approximately 50 mN/m [229]. Merrill et al., 2004 found in a separate study that minimum surface tension was above 5 mN/m in preterm neonates and increased significantly when the percentage of SP-B/PC ratio was below 1 % [230]. To create a conservative in vitro model for nRDS, 26.6 µg/mL of poractant alfa (i.e., equivalent to

13.25 μg/mL of phosphatidylcholine, 10 μg/mL of DPPC, 0.14 μg of SP-B) was added to the subphase.

7.2.4 Equilibrium and dynamic surface tension measurements

The surface tension was measured using the Wilhelmy plate method in a computer-controlled Langmuir–Blodgett instrument (MicroTrough XS, Kibron, Malminkaari, Helsinki, Finland). The tip of the plate was submerged in the subphase (i.e., aqueous solution), and the force of surface tension pulling the tip downwards was measured.

For the clean air-aqueous interface study, the subphase was filled with 67 mL of 0.9 % w/v NaCl aqueous solution. The subphase temperature was heated to 37 °C using a temperature-controlled water bath. Samples were injected into the subphase, and the equilibrium surface tension was deemed to have been reached when fluctuations were smaller than 0.1 mN/m over a minute. The initial area was 12,000 mm^2. Dynamic surface tension measurements were started after the surface tension had equilibrated. The barriers on the Langmuir-Blodgett trough compress from 12,000 mm^2 to 2,500 mm^2 and vice versa for expansion. The compression and expansion rates were both 140 mm^2/sec, and the measurements from the second cycle are presented in the results.

For the simulated lung fluid study, the subphase was filled with 67 mL of the simulated lung fluid (as described in Section 7.2.3) in the Langmuir-Blodgett Trough. The surfactants were slowly added to the air-aqueous interface directly, and the equilibrium surface tension was measured. For the dynamic surface tension, the surface area was reduced from 6,000 mm^2 to 2,700 mm^2 during the compression phase and expanded back to 6,000 mm^2 during the expansion phase.

The behaviour of microbubbles on the Langmuir-Blodgett trough was also observed using a CCD camera (MicroPublisher 3.3 RTV, QImaging, Canada) and a Leica DM500 microscope (Leica Microsystems GmbH, Germany) at a magnification of 4 or/and 10.

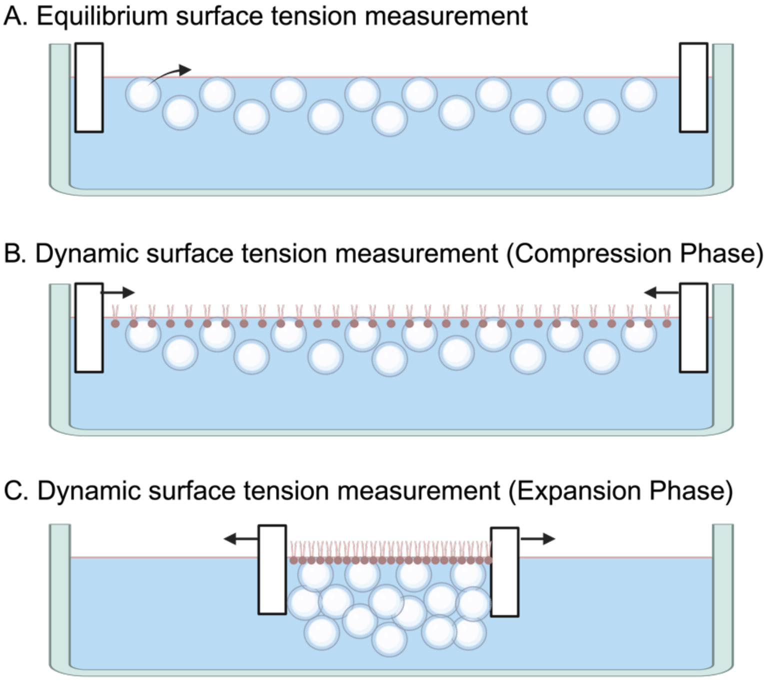

A. Equilibrium surface tension measurement

B. Dynamic surface tension measurement (Compression Phase)

C. Dynamic surface tension measurement (Expansion Phase)

Figure 7.3. The schematic shows the method of equilibrium and dynamic surface tension measurement using Langmuir-Blodgett Trough. (A) shows equilibrium surface tension measurement. Microbubble suspensions were added to the Langmuir-Blodgett trough, and the change in surface tension of the air-aqueous interface was measured. Microbubbles were found adjacent to the air-aqueous interface because of the flotation effect. The black arrow represents the transfer of surfactants from microbubble suspension to the air-aqueous interface. (B) and (C) shows dynamic surface tension measurement. (B) and (C) shows the microbubbles adjacent to the surfactants on the air-aqueous interface, and the effect of microbubbles on the air-aqueous surface tension is measured for the compression phase (B) and for the expansion phase (C).

7.3 Results and Discussion

7.3.1 Effect of PEGylated microbubbles on the surface tension of a clean air-aqueous interface

The behaviour of microbubbles on a clean air-aqueous interface and its subsequent effect on the surface tension was studied. PEGylated microbubbles were washed to remove as much of the other macromolecular structures (e.g., liposomes, micelles, and potentially multi-lamellar structures) in the microbubble suspension, and it produced a microbubble population that is shown in Figure 4F.

The change in surface tension of a clean air-aqueous interface by washed microbubbles was compared to a lipid suspension with the same composition. Figure 7.4C shows the microbubbles achieved a lower air-aqueous surface tension than the lipid suspension (48.2 vs 57.0 mN/m, respectively), and the rate of the decrease is faster with the microbubbles. This is partly due to the flotation effect. A large proportion of the microbubbles have sufficiently large size (> 1.0 μm) that buoyancy determined their movement [231] (Figure 7.4F). The flotation of microbubbles created a greater surfactant concentration gradient between the air-aqueous interface and the adjacent aqueous subphase than that by the lipid suspension and thus could explain the increased rate of reduction in surface tension.

It was found that there is mechanism(s) other than the increased concentration gradient that contributed to the faster reduction in surface tension. Critical micelle concentration (CMC) for DPPC/PEG40-S lipid suspension was characterized (Figure 7.4E), and it was found that the air-aqueous surface tension at CMC (50.0 mN/m) was higher than the surface tension achieved by the washed microbubbles (48.2 mN/m). This suggested that microbubbles have a different mechanism(s) of transferring the surfactants (i.e., DPPC and PEG-40S) to the air-aqueous interface than that of lipid suspension.

One possible mechanism is foam and/or bubble rupture (as described in the schematic in Figure 7.4A). When observed under the microscope, microbubbles were found to coalesce into large bubbles (in hundreds of micrometer size range), and the large bubbles floated to the air-aqueous interface (Figure 7.4B). Large bubbles are known to collide with the interface, leading to either a bubble rupture or the formation of a foam (which then ruptures with time) [231], [232]. Bubble rupture has been shown to deposit bubble film material directly onto an air-water interface [232]. Similarly, foam film rupture creates regions of densely packed surfactants [233]. Foam/bubble rupture explains the increased surfactant adsorption and reduction in surface tension below CMC.

The behaviour of microbubbles during compression and expansion and their effect the dynamic surface tension was studied (Figure 7.4D). Dynamic surface tension measurements with the DPPC/PEG40-S unwashed microbubble suspension were compared to those with the corresponding DPPC/PEG40-S lipid suspension. The difference in the dynamic surface tension between the two formulations was striking below the air-aqueous surface tension of 20 mN/m. DPPC monolayer on an air-aqueous interface is known to enter a collapsing state at around 20 mN/m of surface tension [24]. The collapsing state is inherently unstable and results in the desorption of DPPC into the subphase in the form of vesicles [25]. The rate of collapse, thus, limits the minimum surface tension that can be reached during compression [24]. The microbubble suspension with the final subphase DPPC concentration of 100 µM achieved air-aqueous surface tension near 0 mN/m, while the lipid suspension, with the same concentration, achieved minimum surface tension of around 10 mN/m.

Foam and bubble rupture could again explain how microbubbles achieved a lower air-aqueous surface tension than that achieved by lipid suspension during compression. The foams ruptured during the compression phase of the cycle, leaving no foams by the end of the compression phase (Figure 7.4B). Some fragments from the foam rupture end up on the air-aqueous interface, thus transferring the surfactant molecules to the air-aqueous interface [23]. In addition to the foam rupture, coalesced bubble rupture may concurrently transfer their surfactant molecules to the air-aqueous interface [22]. It is deduced that the foam and bubble rupture act as the source of phospholipid transfer to the air-aqueous interface, replenishing the lost phospholipids from monolayer collapse and desorption during the compression of the air-aqueous surface area.

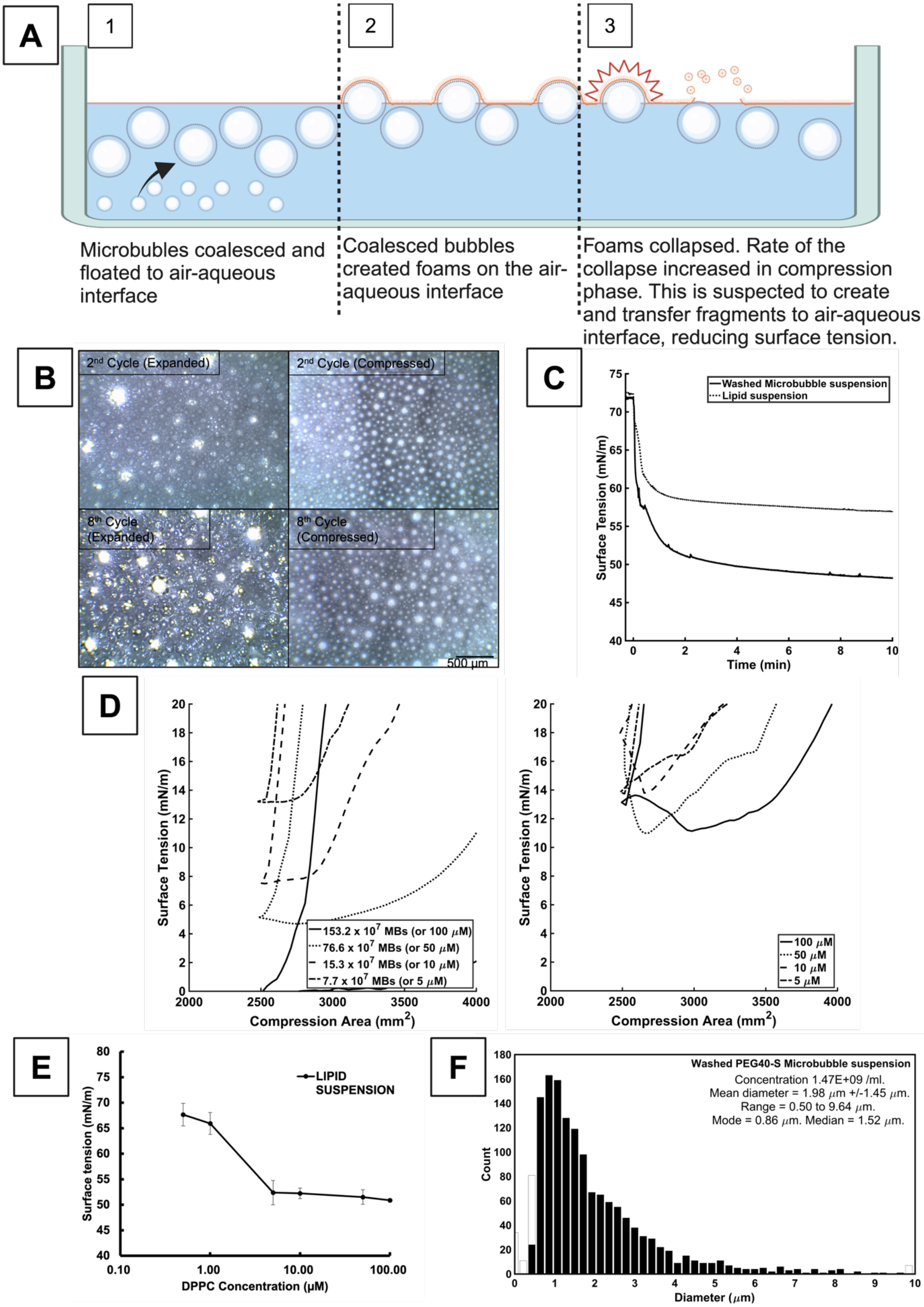
A
1
2
3
Microbubles coalesced and floated to air-aqueous interface
Coalesced bubbles created foams on the air-aqueous interface
Foams collapsed. Rate of the collapse increased in compression phase. This is suspected to create and transfer fragments to air-aqueous interface, reducing surface tension.
B
2nd Cycle (Expanded)
2nd Cycle (Compressed)
8th Cycle (Expanded)
8th Cycle (Compressed)
500 µm
C
Washed Microbubble suspension
Lipid suspension
Surface Tension (mN/m)
Time (min)
75
70
65
60
55
50
45
40
0
2
4
6
8
10
D
Surface Tension (mN/m)
Compression Area (mm²)
20
18
16
14
12
10
8
6
4
2
0
2000
2500
3000
3500
4000
153.2 x 10⁷ MBs (or 100 µM)
76.6 x 10⁷ MBs (or 50 µM)
15.3 x 10⁷ MBs (or 10 µM)
7.7 x 10⁷ MBs (or 5 µM)
100 µM
50 µM
10 µM
5 µM
E
LIPID SUSPENSION
Surface tension (mN/m)
DPPC Concentration (µM)
80
75
70
65
60
55
50
45
40
0.10
1.00
10.00
100.00
F
Washed PEG40-S Microbubble suspension
Concentration 1.47E+09 /ml.
Mean diameter = 1.98 µm +/-1.45 µm.
Range = 0.50 to 9.64 µm.
Mode = 0.86 µm. Median = 1.52 µm.
Count
Diameter (µm)
180
160
140
120
100
80
60
40
20
0
0
1
2
3
4
5
6
7
8
9
10

Figure 7.4. (A) A schematic that shows the behaviour of PEGylated microbubbles in a clean air-aqueous interface. Microbubbles coalesced to form larger bubbles, which floated towards and rested adjacent to air-aqueous interface. Some of the bubbles became foams. Bubbles and foams ruptured. The rupture, which is known to create surfactant fragments, is suspected to transfer the surfactants onto the interface, reducing the surface tension. (B) The images were taken with a magnification objective of 4. The expanded images were taken when barriers were fully expanded (creating a surface area of 12,000 mm^2), and the compressed images were taken when barriers were fully compressed (surface area of 2,500 mm^2). Coalesced microbubbles are characterised by circular boundaries without a bright white colour. The foams, on the other hand, do not have clear boundaries and have a bright white colour on the images, which suggests light reflection on their surface. The foams were only present in the expanded phase of the compression/expansion cycle, and their numbers increased with the rounds of the cycle. Compression of the surface area destroyed the foams, thus leaving no foams at the end of the compressed phase. Foams are replenished during the expansion phase of the cycle. (C) The surface tension of the air-aqueous interface created by washed microbubbles was compared to that created by lipid suspension. The lipid suspension and the microbubbles had the same lipid composition and concentration. The volume of suspension equivalent to 62.11 μg of DPPC was added to 67 mL of 0.9 % w/v sodium chloride aqueous solution. (D) Dynamic surface tension of DPPC/PEG40-S microbubbles and lipid suspension were measured at various concentrations of DPPC. The micromolar concentration represents the concentration of DPPC in 67 mL of 0.9 % w/v NaCl aqueous subphase. The area was compressed from 12,000 mm^2 to 2,500 mm^2 and then expanded back to 12,000 mm^2. The right line of the hysteresis represents the compression phase, and the left line (which has a steeper gradient at around 2,500 mm^2) represents the expansion phase. The minimum surface tensions reached by microbubble and lipid suspension at 100 μM were statistically compared using a t-test ($n = 3$), and the p-value was less than 0.01, suggesting that they were significantly different. (E) Relationship between the concentration of lipid suspension and the air-aqueous surface tension ($n=3$). The subphase is 67 mL of 0.9 % w/v NaCl aqueous solution. Error bars indicate a standard deviation. Increasing the concentration of lipid suspension reduced the surface tension down to 50.0 mN/m where the plateau reached at 10 μM. This suggested that the critical micelle concentration (CMC), or the concentration above which the air-aqueous surface tension no longer reduces, is achieved at around 10 μM. (F) Size distribution of washed PEGylated microbubbles as measured using light microscopy (three batches of samples were measured with twenty images for each sample). The microbubbles used in this study had a concentration of 1.47 x 10^9 microbubbles/ml and a median diameter of 1.52 μm.

7.3.2 [234]Microbubbles improve the surface activity of poractant alfa during compression

Microbubbles were manufactured with diluted poractant alfa and an air gas core (PaMBs), and had a lower concentration (6.66 x 10^6 /ml), larger diameter (i.e., mean diameter was 13.1 μm), and broader size distribution (i.e., the range of diameter was 0.9 to 31.3 μm) than the PEGylated microbubbles.

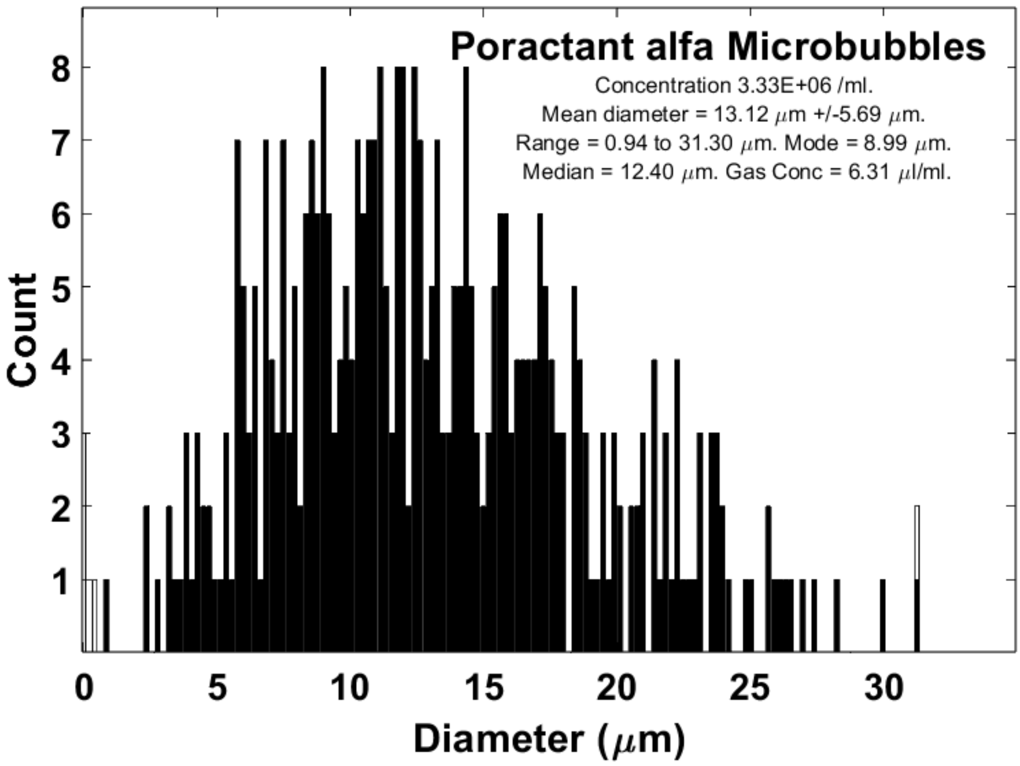

Figure 7.5. Size characteristics of the poractant alfa microbubbles (PaMBs) are presented (three batches of samples were measured with twenty images for each sample).

PaMBs achieved similar equilibrium surface tension as poractant alfa (Figure 7.6A), but the dynamic surface tension during the compression and expansion cycle dramatically differed between the PaMBs and poractant alfa (Figure 7.6B). During the compression phase, PaMBs achieved lower air-aqueous surface tension than poractant alfa (8.91 vs 17.18 mN/m). PaMBs, however, had unfavourable characteristics for use in nebulized lung surfactant therapy. They could not be nebulised using a vibrating mesh nebuliser because the majority of PaMBs were larger than 3 μm in diameter (mesh holes have diameters below 3 μm). Additionally, PaMBs had poor stability and disappeared within 15 minutes at 37 °C. This partly explained the increase in the air-aqueous surface tension at the end of the compression/expansion cycle (Figure 7.6B). Microbubbles with smaller diameters, higher concentration and better stability were required for nebulised lung surfactant therapy. Poractant alfa, an animal-derived product, also has other disadvantages, such as a high cost, low availability, and difficulty in manufacturing.

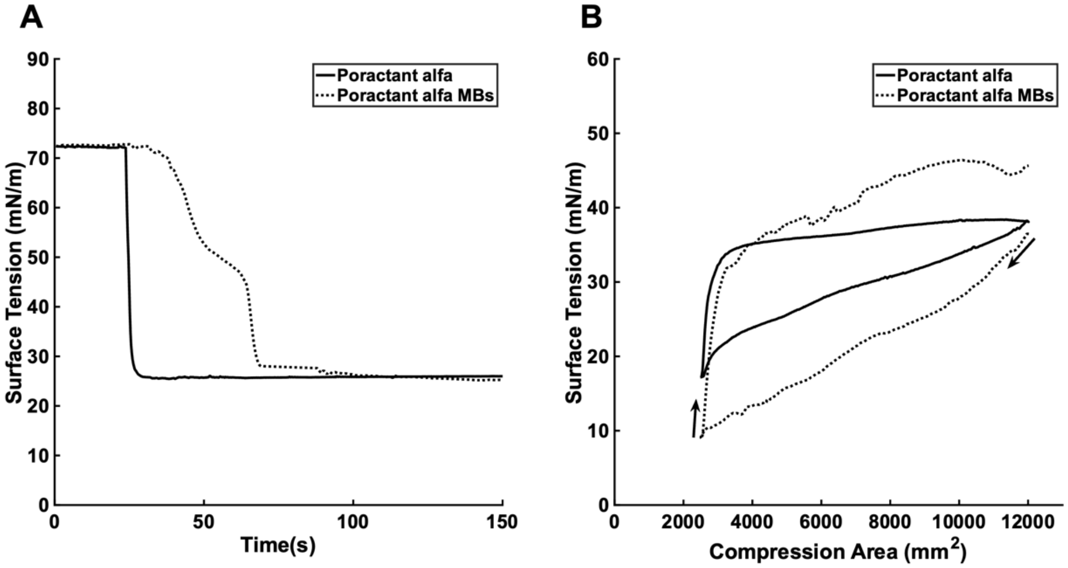

Figure 7.6. (A) The effect of poractant alfa or PaMBs on equilibrium surface tension was measured at a DPPC concentration of 195.75 mg/mL (equivalent to 10 µM of DPPC). (B) The effect of poractant alfa or PaMBs on dynamic surface tension was measured at a DPPC concentration of 195.75 µg/mL. The subphase was 0.9 % w/v NaCl aqueous solution. The area was compressed from 12,000 mm^2 to 2,500 mm^2 and then expanded back to 12,000 mm^2. The black arrows indicate the compression/expansion phase.

7.3.3 Creating an nRDS-model air-aqueous interface

The equilibrium and dynamic surface tension of the more physiologically relevant air-aqueous interface were measured (Figure 7.7). The equilibrium surface tension appear to be lower than the literature value [229] (27 mN/m vs ~ 50 mN/m). Poractant alfa, being a potent surface tension-reducing agent, reduced the equilibrium surface tension to 27 mN/m even at very low concentrations (down to 226 ng/mL of poractant alfa). The minimum surface tension of lung aspirates from nRDS patients ranged from 5 to 22 mN/m [230]. The minimum surface tension of the simulated air-aqueous interface was on the higher end of the range (22 mN/m), suggesting that the model interface represents more clinically challenging cases.

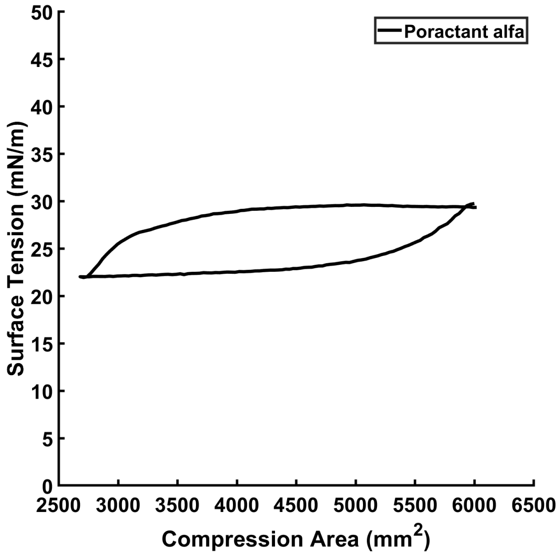

Figure 7.7. The dynamic surface tension of the simulated lung air-aqueous interface was measured. The subphase was 0.9 % w/v NaCl aqueous solution. The area was compressed from 6,000 mm2 to 2,700 mm^2 and then expanded back to 6,000 mm^2. The concentration of poractant alfa on the simulated interface was 26.6 µg/mL (i.e., equivalent to 10 µg/mL of DPPC and 0.14 µg of SP-B).

7.3.4 Behaviour of microbubbles on the nRDS-relevant model air-aqueous interface

In the experiment, equal amounts of DPPC were added to the simulated air-aqueous interface by directly spreading them onto the surface. This was done for PEG-free microbubbles, PEG-free lipid suspension, and poractant alfa to facilitate a comparison of their surface activities (Figure 7.8). Additional poractant alfa on the simulated air-aqueous interface did not further reduce the surface tension at the air-aqueous interface (27 mN/m). The fluctuations in the readings were caused by the movement in the probe whilst spreading. The addition of either lipid suspension or microbubbles reduced the surface tension to 25 mN/m. This suggested that the surfactant molecules lowered the surface tension, and microbubbles did not have an additional effect of changing the surface tension on an air-aqueous interface [234].

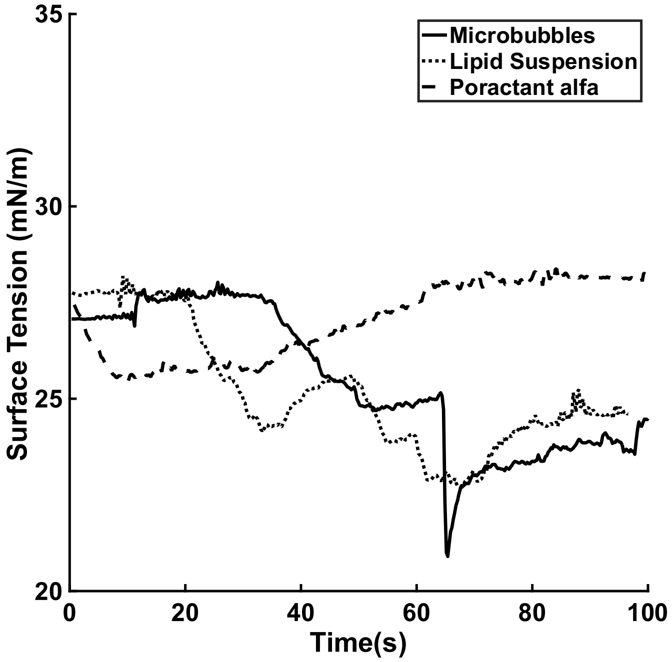

Figure 7.8. The change in the surface tension of the nRDS-relevant air-aqueous is measured after adding poractant alfa, PEG-free lipid suspension, or PEG-free microbubble suspension. Volumes that are equivalent to 670 μg of DPPC were added for the three groups. A total lipid mass of 1.53 mg was added for lipid suspension and for microbubble suspension, and a total lipid mass of 1.78 mg was added for poractant alfa.

The effects of the three treatments (PEG-free microbubbles, PEG-free lipid suspension, and poractant alfa) on the dynamic surface tension of the model air-aqueous interface were then studied (Figure 7.9). Microbubbles reduced surface tension below 5 mN/m, whereas the lipid suspension and poractant alfa produced a minimum surface tension above 20 mN/m at the same DPPC concentration (in fact, the poractant alfa had a higher total lipid concentration). This suggested that microbubbles interact differently with the phospholipid monolayer from the other structures present in lipid suspension (e.g., liposomes and micelles). This was expected because surfactants in bilayers (e.g., in liposomes and lamellar structures) are known to be more stable and thus are difficult to fuse with another surfactant layer as compared to surfactants in monolayers (e.g., microbubbles) [235].

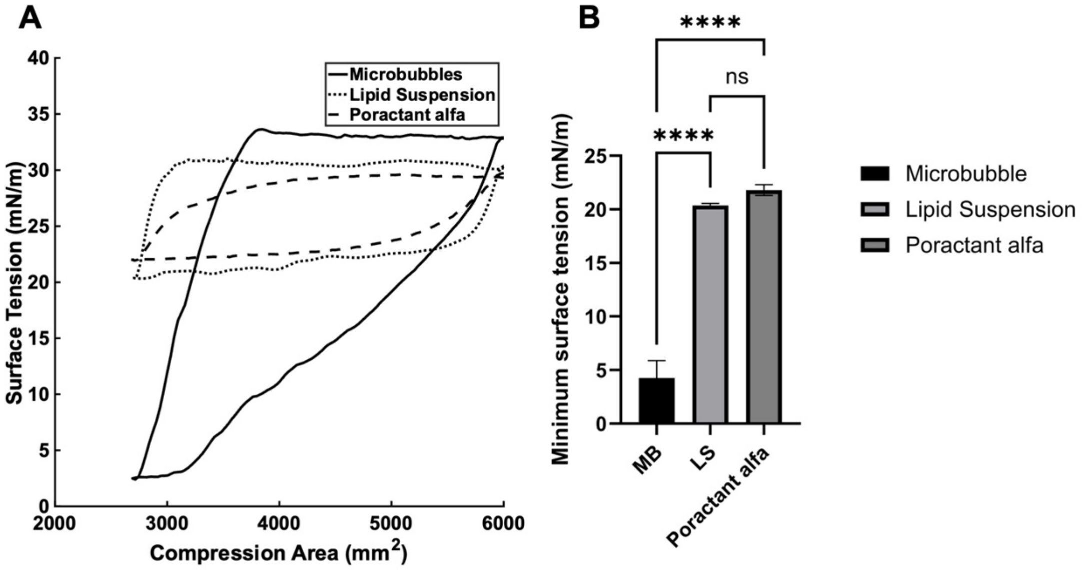

Figure 7.9. (A) The effect of poractant alfa, PEG-free lipid suspension, or PEG-free microbubbles on dynamic surface tension was measured. Volume equivalent to 670 μg of DPPC (or an additional 10 μg/mL in the subphase) was added to the subphase. The subphase was the nRDS-relevant air-aqueous solution. The area was compressed from 6,000 mm^2 to 2,700 mm^2 and then expanded back to 6,000 mm^2. (B) The minimum surface tensions of the air-aqueous interface achieved by microbubbles, lipid suspension, and poractant alfa were compared (n=3). ** represents $p \leq 0.01$, *** represents $p \leq 0.001$, and **** represents $p \leq 0.0001$.

7.3.5 Possible mechanism of microbubbles at the nRDS-relevant model air-aqueous interface

The mechanism(s) by which the microbubbles reduced the air-aqueous surface tension in the nRDS-model interface appeared to be related to the clusters of microbubbles below the air-aqueous interface. The microbubbles were seen to be floating near the air-aqueous interface and to form clusters upon compression of the air-aqueous surface area. Each compression cycle created new or increased the size of clusters of microbubbles near the interface. The cluster(s) of microbubbles at the end of the 50th cycle were dramatically larger than the clusters in the 2nd compression cycle (Figure 7.10C-E).

The following pieces of evidence suggest that the microbubbles are instrumental for the low minimum surface tension and are expended to reduce the minimum surface tension. They, therefore, indirectly substantiated that the microbubble-phospholipid monolayer interaction exists. The number of microbubbles directly determined the minimum surface tension reached during the compression phase (Figure 7.10A). This suggested that the microbubbles are instrumental for low air-aqueous interfacial tension. Compression and expansion cycles reduced the number of microbubbles. The number of microbubbles per mm^2 of the air-aqueous interface was reduced from 2.96×10^8 MBs/ mm^2 at the end of the 2nd cycle to 7.18×10^7 MBs/mm^2 at the end of the 50th cycle (Figure 7.10C-E). Reduction in the number of microbubbles led to an increase in the minimum surface tension reached during the compression phase of the cycle after the first five cycles (Figure 7.10B). This indirectly proves that the microbubbles are transferring phospholipids onto the air-aqueous interface, but the exact mechanism of the transfer is yet to be found and needs further investigation.

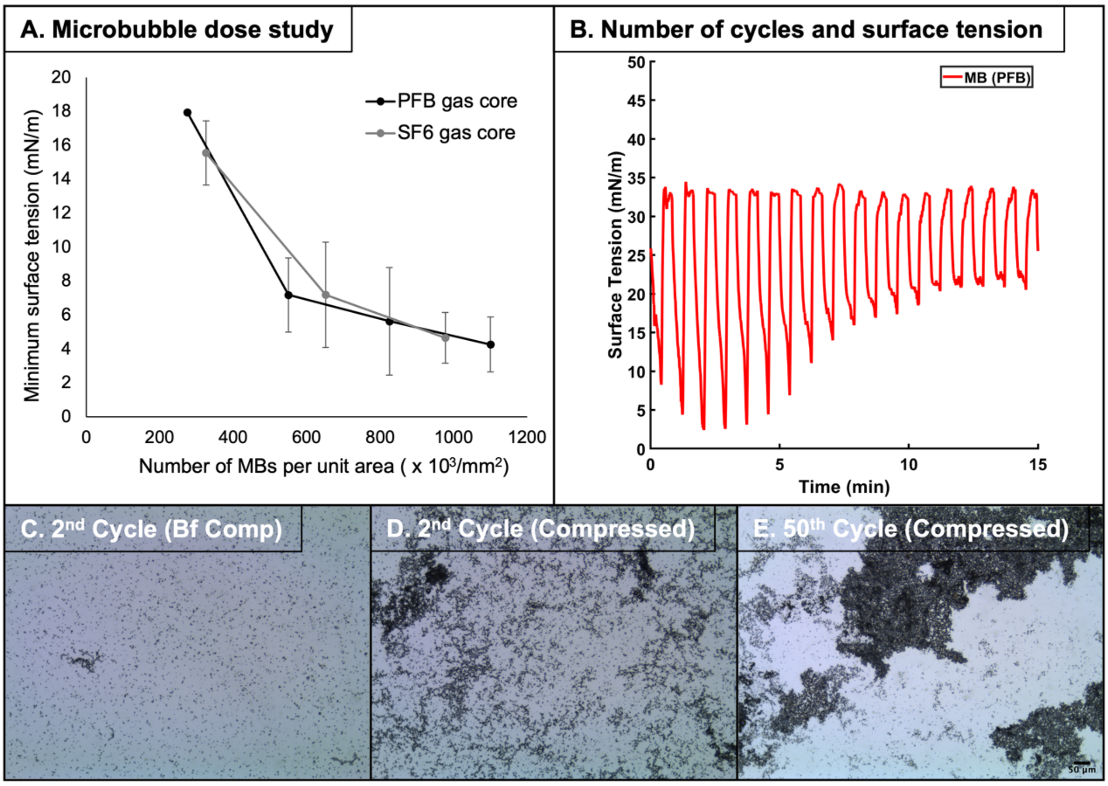

Figure 7.10. (A) The number of microbubbles determined the minimum surface tension reached during the compression phase of the cycle (n=3). The compression area was reduced from 6,000 to 2,700 mm^2. (B) The change in surface tension with cycles of compression and expansion is shown. The area was again reduced from 6,000 to 2,700 mm^2 and expanded vice versa. The experiment has been repeated three times. C-E show images of microbubbles during compression and expansion cycles. The magnification is 10. (C) is an image of microbubbles on the air-aqueous interface taken at the end of 1st expansion phase and just before the 2nd compression. (D) is taken after the 2nd compression. (E) is taken after 50 cycles of compression and expansion cycles and taken at the compressed state. Clustering of microbubbles is speculated to hinder microbubbles' ability to reduce surface tension during the compression phase because the microbubbles cover less surface area on the air-aqueous interface and thus exert less of their effect on the phospholipid monolayer during the compression phase.

7.3.6 Clinical considerations for microbubbles as a replacement for lung surfactant therapy

A minimum surface tension below 5 mN/m is the in vitro marker for the efficacy of surfactants [222], [229], [230], [236]. The minimum surface tension is instrumental in predicting the likelihood of airway or alveoli collapse because low surface tension prevents over-extension of the lung airways, and its recoil effect leads to the collapse. The collapsed airway is also more likely to re-open with low surface tension on the air-aqueous interface. The minimum surface tension of the air-aqueous interface achieved by microbubbles was comparable to that of healthy neonates. Air-aqueous surface tension achieved by the lung aspirates from healthy neonates was below 5 mN/m, and ranged from 0.4 to 4.7 mN/m [236], and microbubbles achieved the minimum surface tension of 4.2 mN/m during the compression phase of the cycle. This is strikingly low compared to air-aqueous surface tension in preterm neonates with nRDS [229], [230] whose minimum surface tension ranges from 26.8 to 44.4 mN/m. With the same DPPC concentration, microbubbles were able to achieve substantially lower surface tension during compression than poractant alfa (4.2 mN/m vs 21.8 mN/m, $p \leq 0.0001$).

The change in surface area during tidal breathing (assuming 5 mL/kg of tidal volume) in preterm neonates (< 32 weeks of gestational period) is calculated to be approximately 20 %. The change in air-water interface tension under 20% area compression was studied. It was found that microbubbles were able to achieve lower surface tension than poractant alfa, and thus would likely improve lung compliance and oxygenation in tidal breathing.

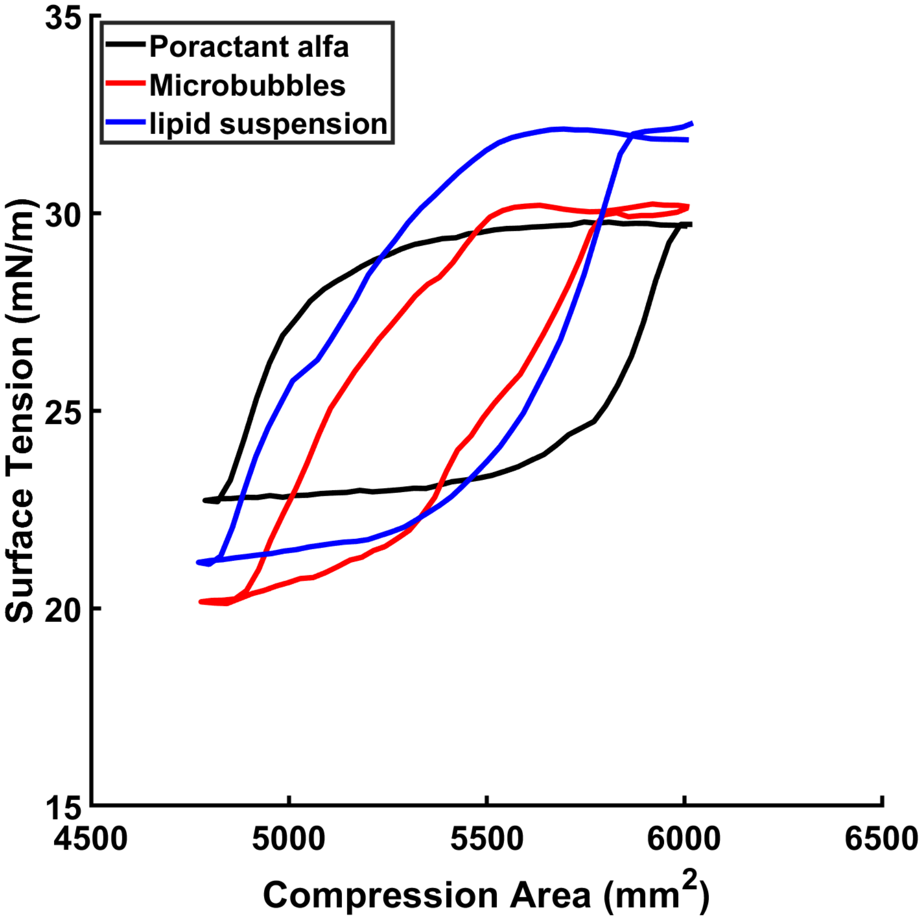

Figure 7.11. The effect of poractant alfa, PEG-free lipid suspension, or PEG-free microbubbles on dynamic surface tension was measured. Volume equivalent to 670 µg of DPPC (or an additional 10 µg/mL in the subphase) was added to the subphase. The subphase was the nRDS-relevant air-aqueous solution. The area was compressed from 6,000 mm^2 to 4,800 mm^2 (i.e., 20% reduction in area) and then expanded back to 6,000 mm^2.

7.3.7 Practical considerations for nebulised lung surfactant therapy

The lack of efficacy reported in a recently terminated clinical Phase 2 trial of nebulised lung surfactant therapy in preterm neonates was attributed to an insufficient amount of surfactant entering the lungs [161]. Poor lung delivery is an inherent problem for pulmonary administration, and the problem is accentuated in preterm neonates because of their narrow airways. Lung deposition of inhaled aerosols in 4-week-old babies was found to be 4.5 % at 2 L/min flow rate and 2 % at 3 L/min [199]. Given that preterm babies have narrower airways, and 8 L/min is the flow rate used for nRDS, it is expected that lung deposition would be considerably lower than 2 % in preterm neonates.

Preterm neonates with less than 32 weeks gestation have yet to form alveolar sacs, and thus, the surface area in their lungs is much smaller than in healthy neonates. It is estimated that the lung surface area in these extreme preterm neonates is around 637.7 cm^2 (or 63770 mm^2) [237]. In the present study, it was found that 800,000 MBs/mm^2 were required to achieve a minimum surface tension below 5 mN/m, and therefore, approximately 51 x 10^9 microbubbles would need to be delivered to the lungs. Assuming that lung deposition is 5 % for microbubble-ladened aerosols, 255 mL of microbubble suspension would be required, and it would take 1020 minutes (or 17 hours) to administer a sufficient dose (assuming a concentration of microbubbles is 4 x 10^9 MBs/mL and an output rate of the vibrating mesh nebuliser of 0.25 mL/min). The current formulation is, therefore, not likely to be suitable for clinical use. Improvements in the surface activity of the microbubbles, microbubble concentration, and lung deposition efficiency will be required.

7.4 Conclusion

This study investigated whether microbubbles could be used to improve surfactant delivery to an air-water interface and, hence, potentially offer a more efficient treatment method for nRDS. It was found that phospholipid-coated microbubbles did improve air-water interface adsorption of phospholipids compared with the equivalent liquid suspension and achieved a surface tension close to zero at lower molecular concentrations during compression of air-aqueous surface area. Further study is required to 1) understand the mechanism(s) in which microbubbles reduce air-aqueous surface tension during compression and 2) to confirm improvement in lung compliance or/and oxygenation with microbubble surfactant therapy in vivo.

Chapter 8 Immunomodulatory action of microbubbles in LPS-induced RAW264.7 macrophages

8.1 Introduction

Neonatal respiratory distress syndrome (nRDS) is the most common respiratory disorder in preterm births and is caused by a combination of poorly developed alveolar sacs and insufficient lung surfactants [182]. Lung surfactants are crucial in maintaining healthy breathing mechanisms. They increase pulmonary compliance, prevent atelectasis at the end of expiration, and facilitate the recruitment of collapsed airways. In addition, lung surfactants act as the first line of defence against foreign bodies and pathogens entering the lung alveoli [132], [238].

A lack of lung surfactants increases the risk of pneumonia [239]. Pneumonia commonly involves inflammation in the alveoli, which is deadly because it further aggravates nRDS and oxygen saturation. Pneumonia causes pulmonary oedema and leakage of proteins in the alveoli [240], [241], which further inactivates already poorly performing lung surfactants. This further increases the surface tension of air-alveoli lining fluid (up to around 20-35 mN/m) and reduces blood oxygen saturation [242]. In the case of bacterial pneumonia, lipopolysaccharides (LPS) can further disturb the function of the lung surfactants on the air-alveolar fluid interface.

Lung surfactant replacement therapy has been suggested as a treatment for pneumonia [243] to improve blood oxygenation. In a clinical study, lung surfactant replacement therapy improved blood oxygenation for a prolonged period in preterm and term neonates with pneumonia, and over 90 % of the neonates survived [243]. The innate defence role of lung surfactants may also be partly responsible for improving survivability in neonates with pneumonia. Approximately 10 % of lung surfactants are composed of lung surfactant proteins (SP), of which SP-A, SP-B, SP-C, and SP-D have been identified. In particular, SP-A and SP-D play important roles in preventing endotoxin shock [244], [245], [246]. SP-A and SP-D bind and reduce the biological activity of LPS. The binding of SP-A to LPS has been shown to induce conformational changes in LPS aggregates, leading to biologically less potent structures [247]. SP-D attenuates LPS binding to TLR4/MD-2 receptors and reduces the subsequent release of inflammatory mediators [248].

Another mechanism that may contribute to preventing endotoxin shock is the regulation of receptor expressions on the host cellular membrane [246]. Under LPS exposure, SP-A was found to lower TLR4 expression levels on the cellular membrane [249], [250]. Survanta, a clinical surfactant extracted from animal lungs, was shown to inhibit LPS signalling by blocking TLR4 translocation to lipid rafts in A549 lung cancer cells, providing the first evidence for specifically coordinated TLR4 positioning and SP-mediated alterations in membrane trafficking [251]. These mechanisms would be expected to reduce the risk of endotoxin shock due to pneumonia and may explain the improved survivability in preterm neonates with pneumonia.

In Chapter 7 of this thesis, microbubbles were suggested as a treatment for nRDS because of their ability to reduce air-aqueous interfacial tension at physiologically relevant conditions. By formulating microbubbles from synthetic phospholipids, they can potentially offer benefits over animal-derived lung surfactants, such as the manufacturability and cost. As mentioned above, however, lung surfactant proteins do more than just reduce the surface tension, so ideally, microbubbles would also be able to fulfil multiple functions. In this chapter, therefore, the immunomodulatory function of microbubbles to reduce LPS-induced inflammation is compared against poractant alfa (i.e., animal-derived lung surfactant) using the RAW264.7 cell line.

8.2 Methodology

8.2.1 Materials

Lipopolysaccharide (LPS) from Escherichia coli was purchased from Sigma-Aldrich (UK). It was prepared as a stock solution at 400 mg/ml in sterile phosphate-buffered saline with vortex mixing and kept in dehydrogenated glass vials at – 20 °C.

Curosurf® (Chiesi Farmaceutici, Parma, Italy), or poractant alfa, is a modified porcine surfactant that contains only 30 – 50 % SP-B and SP-C of the natural porcine surfactant. Poractant alfa was used as the positive control for the study because it is the most commonly used worldwide for nRDS treatment [252].

DPPC (Avanti Polar Lipids, USA), DPPG (Avanti Polar Lipids, USA), and palmitic acid (Sigma Aldrich, UK) were used for lipid suspension and microbubble suspension. Sodium Chloride (NaCl) and propylene glycol were purchased from Sigma-Aldrich (UK). Perfluorobutane (PFB), perfluoropropane (PFP), and sulphur hexafluoride (SF6) were purchased from BOC Group plc, Woking, UK.

8.2.2 RAW264.7 transfection with NF-kB reporter plasmid

RAW264.7 is a macrophage cell line that was established from a tumour in a male mouse induced with the Abelson murine leukaemia virus. The cell line was purchased from ATCC

(Manassas, Virginia, USA). The cell line was routinely maintained in DMEM + GlutaMaxTM-I medium containing 10 % fetal bovine serum (D10). The medium was purchased from Gibco, Thermo Fisher (UK). The cell line was cultured at 37°C in an atmosphere of 5% CO2 in humidified air.

RAW264.7 cell line was transfected with NF-kB reporter plasmid using a transfection reagent called FuGene® HD Transfection Reagent (Promega Corporation, USA). The plasmid produces luciferase (NanoLuc) when NF-kB is expressed. The cell line was routinely maintained in DMEM + GlutaMaxTM-I medium containing 10 % fetal bovine serum and 5 μg/ml hygromycin B (Roche, Germany). Hygromycin B was used to select out for cells transfected with the NF-kB reporter plasmid. The cells were cultured at 37 °C in an atmosphere of 5 % CO_2 in air. The transfected cell line was used for all the experiments.

8.2.3 RAW264.7 transfection with NF-kB reporter plasmid and NF-kB measurement

Confluent cells in a culture flask were first detached from the flask, using 0.25 % w/v trypsin and 0.2 % w/v EDTA solution was equilibrated to room temperature before use. The cell culture medium was first removed from the flask, and DPBS was used to wash out the remaining culture medium. The trypsin/EDTA solution was added to the flask, and the flask was returned to the incubator. After 5 minutes of incubation, an equal volume of the cell culture medium to the trypsin/EDTA solution was added to the flask to deactivate trypsin. The cell suspension in the flask was moved to a 15 mL falcon tube, and was centrifuged for 5 min at 500 g. The supernatant was removed, and the subnatant cells were resuspended in 1 mL of D10 (+ 5 μg/ml hygromycin B). Cell number in the suspension was counted using an automated cell counter after adding an equal volume of trypan blue and the cell suspension. A volume of suspension that is equivalent to 20,000 cells was added to each well in a black-walled 96-well plate, and D10 (+ 5 μg/mL hygromycin B) was added to the well to make it up to a final volume of 100 μL per well. The cells were left at 37 °C in an atmosphere of 5 % CO_2 in air overnight until each well became confluent.

Nano-Glo® Luciferase Assay System (Promega Corporation, USA) was used to measure the concentration of Nanoluc produced from the transfected cells. The cells produced Nanoluc when NF-kB was expressed, and thus, NF-kB expression was indirectly measured using the method. Cells and the reagents were equilibrated to room temperature. 100 μl of the reagent was added to each well that contained cells grown in 100 μl of the medium. After waiting for 3 minutes, luminescence was measured using a plate reader (CLARIOstar Plus, BMG Labtech, Germany).

8.2.4 Microbubble and lipid suspension preparation

The lipid film was first prepared. 8mg of DPPC (Avanti Polar Lipids, USA), 8 mg of DPPG (Avanti Polar Lipids, USA), and 2 mg of palmitic acid (Sigma Aldrich, UK) in chloroform (Sigma Aldrich, UK) were mixed in an 8 mL glass vial. The mixture was subsequently dried using a vacuum evaporator at 30 °C for 3 hours to allow for chloroform to evaporate. The obtained dry lipid film was suspended in 4 mL of 20 % w/v propylene glycol in 0.9 % w/v NaCl aqueous solution (i.e., the lipid suspension had a DPPC concentration of 2 mg/mL or a total lipid concentration of 4.5 mg/mL) for 1 h in a temperature-controlled shaker at 60 °C and at 800 rpm. Lipids were then homogeneously dispersed for 60 s using a sonicator (Q125, QSonica, Newtown, CT, USA) at a power setting of 50 % with the tip completely immersed in the lipid suspension. This is the lipid suspension.

The lipid suspension was subsequently used to make microbubbles. The lipid suspension was first de-gassed, and then gas was added to the headspace. Three different gases were tested; namely, perfluorobutane (PFB), perfluoropropane (PFP), and sulphur hexafluoride (SF_6). A mechanical shaker, CapMix (3M, UK), was used to make the microbubbles by agitation. The speed was set at 4,300 rpm and was shaken for 15 seconds. Immediately after production, the vial containing the microbubble suspension was capped and placed on ice.

8.2.5 Quantification of inflammatory mediators (IFN-α, IFN-b, and TNF-α)

Release of IFN-α, IFN-b, and TNF-α were quantified using Luminex® (Luminex Corporations, TX, USA). After the exposure of LPS, the cells were centrifuged for 5 mins at 500 g, the supernatant was removed, and the concentrations of IFN-α, IFN-b, and TNF-α in the transfected RAW264.7 cells were determined with a Luminex instrument according to the manufacturer's instructions. For IFN-α and IFN-b measurement, IFN-alpha/IFN-beta 2-Plex Mouse ProcartaPlex™ Panel (Fisher Scientific, UK) was used. For TNF-α measurement, Luminex® Multiplex Assay was used. Briefly, the detection antibodies bind to the relevant inflammatory mediators in the samples and standards given in the kit. A standard curve was generated using the standards given in the kit, and the mean fluorescent intensity data was analysed using a 5-parameter logistic or spline curve-fitting method to calculate the IFN-α, IFN-b, and TNF-α concentrations in the samples.

8.2.6 Effect of LPS concentration and exposure time on NF-kB expression in RAW264.7

LPS induces inflammatory response via TLR4 receptor binding, and NF-kB is one of the main upstream inflammatory mediators of the TLR4 pathway. The degree of NF-kB expression was used to determine the optimal LPS concentration and exposure time. Optimal LPS concentration for the purposes of this study was defined as the concentration that can reliably give high levels of NF-kB expression while avoiding excessive amounts of LPS in the extracellular fluid. Excessive amounts of LPS can mask the binding effect of the surfactants and thus are undesirable.

In a 96-well plate with overnight-grown cells, the following concentrations of LPS were added: 0.025, 0.05, 0.1, 0.25, 0.5, 1, 2.5, 5, 10, 20 mg/mL. The cells were exposed to LPS for 5 hours, and then each well was evaluated using NanoLuc® luciferase assay. Luminescence (i.e., NF-kB) was measured using a plate reader (CLARIOstar Plus, BMG Labtech, Germany).

Followingly, the effect of the duration of exposure on NF-kB expression was studied. 1 mg/mL of LPS was added to each well that contained overnight-grown cells. The cells were exposed to the LPS for 2, 8, 12, and 24 hours, and then each well was treated with NanoLuc® luciferase assay. Luminescence was measured using a plate reader (CLARIOstar Plus, BMG Labtech, Germany).

8.2.7 Microbubble size distribution and its change over time at the bottom of a well

Microbubbles, due to their lower density than the aqueous environment, will eventually rise to the top of a container in which they are placed. Thus, depending on the orientation of the cell culture chamber, flotation may drive microbubbles away from adhered cells. The speed of flotation is dependent on the microbubble size, with larger microbubbles rising more quickly. To assess the effect of flotation, changes in the microbubble population at the bottom of the well (i.e., where the cells were) were measured by characterising the microbubble size distribution at different time points.

Microbubble suspensions were manufactured as described above. As the size distribution was expected to be broad, two different instruments were used. The larger bubbles were characterised using a Coulter-counter (Multisizer III, Beckman Coulter, Opa Locka, FI). 10 μL of microbubble suspension was added to 90 μL of D10 in a 96-well plate, and an up-and-down motion of the pipette was repeated 10 times to ensure thorough mixing. The plate was placed in an incubator that was at 37 °C in a humid atmosphere of 5 % CO_2, and the measurement was taken at 0, 5, 15, and 30 minutes. 2 μL was slowly drawn from the bottom of the well, and the outer walls of the pipette tip was wiped. The drawn 2 μL sample was evaluated using the Coulter Multisizer III.

Nanoparticle tracking analysis using a Videodrop system (Paris, France) was used to measure microbubbles sized less than 1000 nm. The parameters were as follows: minimum number of particles to track was 300, max number of videos was 10, the number of frames was 100, exposure time was 0.90 ms, LED intensity was 94 %, and the detection threshold was 4.20.

All samples were measured at least three times by each instrument and analysed for both number- and volume-weighted size distribution. The number of microbubbles was counted by subtracting the number of particles in lipid suspension to the number of particles in the unwashed microbubble suspension (which is composed of lipids and microbubbles). The microbubble washing (i.e., centrifugation and re-constitution of microbubble cake) induced loss of microbubbles and bias selection of microbubbles. Thus, the difference in the particle size distribution between the lipid suspension and microbubble suspension was used to deduce the particle size distribution of the microbubbles). An average of 1 % of DPPC of lipid suspensions was used to form microbubbles. The change in lipid concentration that is not used to form microbubbles was assumed to be negligible in this study and thus assumed not to change the number of lipid particles in the unwashed microbubble suspension.

8.2.8 The effect of pre-incubation with microbubbles on LPS-induced inflammation in RAW264.7 macrophages

The release of IFN-α, IFN-β, TNF-α, IL-6, and IL-12, which are downstream inflammatory mediators of NF-kB, was quantified after RAW264.7 macrophages were stimulated by LPS. When these inflammatory mediators are released extracellularly, an acute inflammatory response is initiated that helps to clear pathogens. However, when these mediators are overproduced, they can harm the host, leading to multiple organ failure (i.e., sepsis) and possibly death (which preterm neonates are susceptible to). It is important to modulate inflammatory mediators, which is one of the roles of lung surfactants. The release of these mediators was utilised as a metric to evaluate the potential of microbubbles to reduce the probability of sepsis.

Lung surfactant proteins were found to block the translocation of TLR4 receptors and regulate the receptor expression on the host cellular membrane. The mechanism helped to reduce the release of inflammatory mediators and prevent endotoxin shock [251]. To evaluate the effect of the cell-microbubble interaction on inflammatory mediator release in LPS-induced RAW264.7 macrophages, the effect of phospholipids and/or lung surfactant proteins binding to LPS was removed. The treatment groups (i.e., poractant alfa as the positive control, DPBS as the negative control, lipid suspension, and microbubble suspension) were pre-incubated with the cells for 30 minutes and then were washed three times with warmed DPBS to remove phospholipids and/or surfactant proteins[251].

Three different microbubble formulations were tested for their immunomodulatory action (i.e., to reduce NF-kB expression) in LPS-induced RAW264.7. The formulations had the same lipid composition (e.g., DPPC, DPPG, and palmitic acid concentration of 2 mg/mL, 2mg/mL, and 0.5 mg/mL) and different gas cores (e.g., PFB, PFP, and SF_6).

The stability of microbubbles in the cell culture environment was studied. The study was performed in 96-well plates. 90 μL of D10 with 5 mg/mL hygromycin B was added to each well. 10 μL of microbubbles were added to the well containing the medium. The plate was placed in a cell incubator at 37 °C in a humid atmosphere of 5 % CO_2 in air. Samples were measured at 0, 5, 15, and 30 min, and all samples were measured at least three times per time point using a method described below. Approximately 2000 microbubbles were imaged per sample.

For microbubble sizing and counting, 10 μL of the microbubble suspensions were placed onto a Neubauer enhanced cell counting chamber (Hausser Scientific Company, USA) under a 24 mm by 24 mm glass coverslip (VWR International, USA). A CCD camera (MicroPublisher 3.3 RTV, QImaging, Canada) and a Leica DM500 microscope (Leica Microsystems GmbH, Germany) were used to image MBs at a magnification of 40. MATLAB® code that was specifically built for MB sizing and counting was used (The Mathworks Inc., USA).

Confluent monolayers of cells were stimulated with LPS (1 mg/ml) for 8 hours for NF-kB assay and 12 hours for IFN-a, IFN-b, and TNF-a LUMINEX assay. In an unpublished experiment conducted by the author of this thesis, the amount of IFN-a released by the cells was compared for 8 hours and 12 hours of LPS exposure and it was observed that 12 hours of incubation led to a greater expression of IFN-a. This was speculated to be due to a time delay from the upstream mediator, NF-kB, to produce the downstream inflammatory mediators.

To investigate the effect of microbubbles on NF-kB, IFN-a, IFN-b, and TNF-a, cells were preincubated with microbubble suspension (concentrations of DPPC, DPPG, palmitic acid were 200 μg/mL, 200 μg/mL, and 50 μg/mL with PFB gas core), lipid suspension (at the same concentrations as the microbubble), poractant alfa (concentrations of DPPC was 200 μg/mL and the concentration of poractant alfa was 533 μg/mL), or DPBS (no phospholipids and surfactant proteins) for 30 minutes. This was followed by the washing step. It involved discarding the cell medium from each well, adding 200 μL of DPBS to each well, and pipetting up and down five times, and discarding the DPBS. This was repeated three times. 95 mL of warmed D10 with 5 μg/mL of hygromycin B and 5 mL of LPS (20 μg/mL) was added to each well, making 1 mg/mL final concentration of LPS. The exposure time before the measurement of NF-kB was 8 hours, and that for IFN-a, IFN-b, and TNF-a was 12 hours.

The study assessed the effect of LPS exposure on the release of other inflammatory mediators (e.g., IL-6 and IL-12), but they were not released and were not further studied.

8.2.9 Increasing proximity of microbubbles to RAW264.7 macrophages and its effect on NF-kB expression upon LPS stimulation.

Flipping the 96-well plate upside-down facilitated the microbubbles to float towards the bottom wall of the well where macrophages adhered. This increased the contact between the cells and the microbubbles, and the effect of increasing the contact between the cells and the microbubbles on NF-kB expression was studied.

Cells were cultured overnight in a 96-well plate as described above. Each well, which contained the cell culture media (i.e., D10), was emptied and then was filled with 300 μL of warmed DPBS. 40 μL of the microbubble suspension, 40 μL of the lipid suspension, 2.67 μL of poractant alfa, or 100 μL of DPBS is added to each designated well. Each well was then filled up to 400 μL with warmed DPBS. The 96-well plate was then flipped upside-down and was put in a cell incubator for 30 minutes. The incubator was at 37 ºC in an atmosphere of 5 % CO_2. This was followed by the washing step. The DPBS was discarded, and then 200 μL of clean DPBS was added to each well. The clean DPBS was pipetted up and down five times and then the DPBS was discarded. This was repeated three times. 95 mL of warmed D10 with 5 mg/mL hygromycin B and 5 μL of LPS (20 μg/mL) were added to each well, making 1 μg/mL final concentration of LPS. The exposure time before the measurement of NF-kB expression was 8 hours.

8.2.10 The effect of co-incubation with microbubbles and LPS on inflammatory mediator expressions in RAW264.7 macrophages

Phospholipids and lung surfactants directly bind to LPS and reduce its activity. This reduces the release of inflammatory mediators by host cells and helps to prevent septic shock. This set of experiments studied how the presence of microbubbles or surfactants influences LPS-induced inflammation in RAW264.7 cells. The effect of the surfactants was a mixed effect of the surfactants directly binding to the LPS molecules, surfactant-cell interaction (e.g., reducing translocation of TLR4 receptors to the cellular membrane), and unknown factors.

Cells were co-incubated with LPS (1 mg/mL) and a treatment group (one of poractant alfa, DPBS, lipid suspension, or microbubbles) at the same concentration mentioned in Section 2.9. There was no washing step. The exposure time before the measurement of NF-kB was 8 hours, and that for IFN-a, IFN-b, and TNF-a was 12 hours.

8.2.11 Data presentation and statistics

Comparisons were made using a paired or unpaired Student’s t-test or analysis of variance with post-hoc testing where appropriate. Differences were considered significant when the p-value was < 0.05.

8.3 Results and Discussion

8.3.1 Determining the optimal LPS exposure duration and concentration in RAW264.7 macrophages

As shown in Figure 8.1, the luminescence peaked at 8 hours of LPS exposure and dropped at 12 and 24 hours. NanoLuc luciferase has an intracellular half-life of approximately 6 hours (according to the manufacturer’s manual), and thus, the luminance was found to reduce when luminance measurement was taken long after the initial LPS exposure. It was determined that the luminance readings would be measured following an 8-hour period of LPS exposure. This approach was taken in order to ensure that the results obtained would be able to differentiate between the various treatment groups being studied.

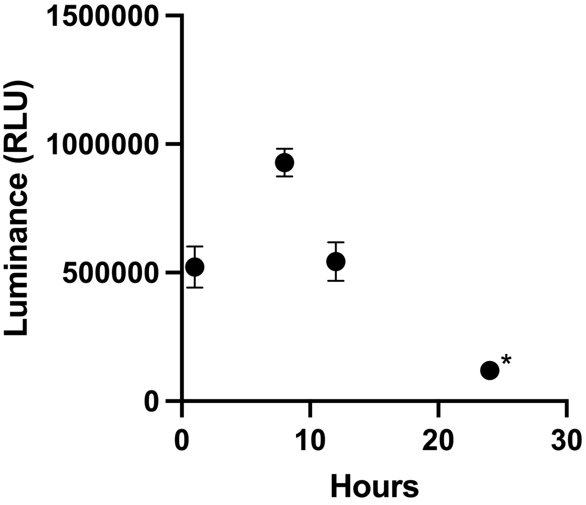

Figure 8.1. The graph shows the effect of LPS exposure time on NF-κB expression in the transfected RAW264.7 cells. It shows that luminance readings peak at 8 hours of exposure, and thus, 8 hours of LPS exposure was deemed to be the optimal duration. The black dots are a mean of 6 readings, and the error bars represent one standard deviation. * The error bar is masked by the black dot. The standard deviation for the 24-hour exposure time was 9664.76.

The effect of LPS concentration on NF-kB expression was subsequently studied (Figure 8.2). The NF-kB expression was found to be positively correlated with the concentration of LPS, ranging from 0.025 mg/mL to 0.5 mg/mL, with a plateau observed at 0.5 mg/mL. These results suggest that TLR4 receptors become saturated with LPS molecules at 0.5 mg/mL. In order to maintain consistency and accuracy in the study, a concentration of 1.0 mg/mL of LPS was chosen as it has been demonstrated to elicit high levels of NF-κB expression while avoiding the introduction of excessive LPS into the cell culture medium. This concentration has been utilised in numerous other studies [253], [254], [255], allowing for appropriate comparisons to be made. The decision to use this concentration was motivated by concerns regarding potential random errors that could lead to variations in LPS concentration.

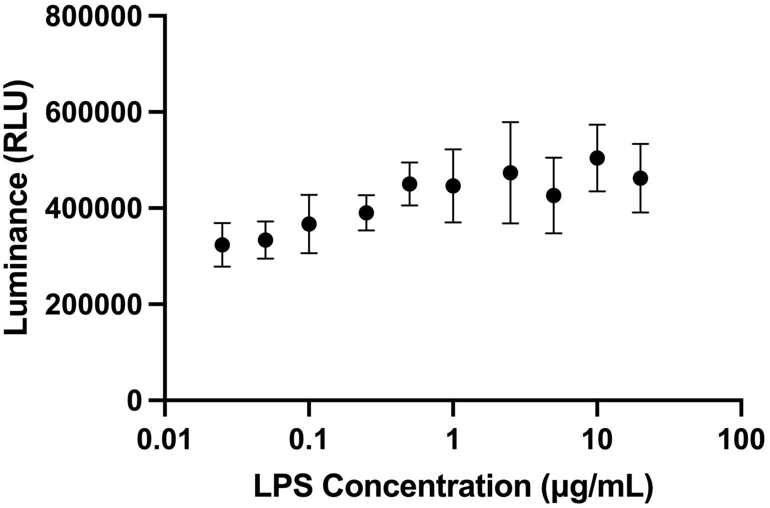

Figure 8.2. The effect of LPS concentration on luminance (or NF-kB expression) is shown. The transfected RAW264.7 cells were exposed to different concentrations of LPS for 8 hours. The optimal concentration of LPS was determined to be 1.0 mg/mL, as it reliably induced high levels of NF-kB expression while minimising excessive LPS in the cell culture medium.

8.3.2 Bubble size distribution at the bottom of a well and its change over time

Videodrop measurements revealed a population of sub-micrometre diameter bubbles, as shown in Figure 8.3. This observation was further supported by the Coulter Multisizer III measurement, which indicated the presence of bubbles in the range of 400 – 800 nm (Figure 8.4). The Coulter Multisizer III was used to measure the change in the bubble population at the bottom of a well over a given period of time (Figure 8.4). As expected, the number of bubbles reduced over time, with larger bubbles being lost more quickly. There was, however, an exception for bubbles sized 400 – 500 nm, whose rate of reduction was higher than for larger bubbles. The study, nevertheless, revealed that bubbles were present at the bottom of the well for the duration of the pre-incubation treatment (i.e., 30 minutes) and thus were in proximity to the adhered cells.

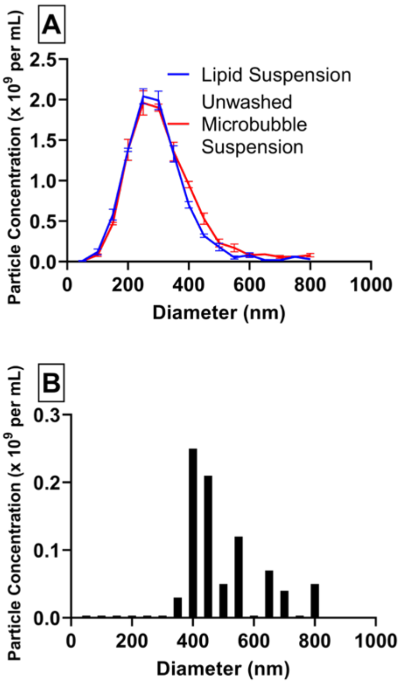

Figure 8.3. A population of sub-micrometre bubbles was sized using Videodrop. (A) the lipid suspension and unwashed bubble suspension were measured (n=3). (B) The microbubble size distribution, which was the difference in particle size distribution between the lipid suspension and the unwashed microbubble suspensions, is shown.

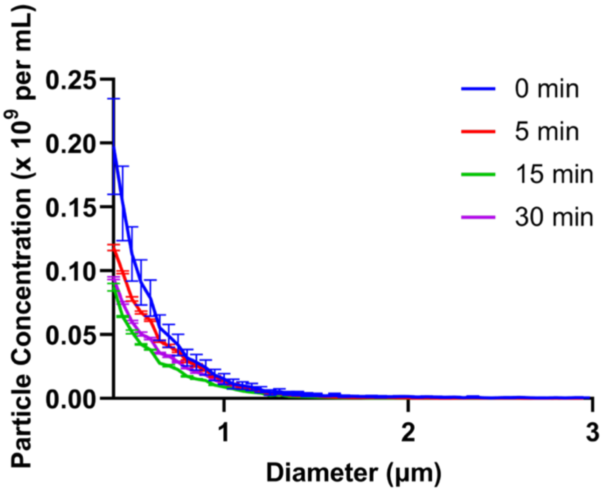

Figure 8.4. A sub-population of microbubbles at the bottom of the well was measured using Coulter Multisizer III. The well plate was kept at 37 ºC and in atmospheric air with 5 % CO_2. The number of bubbles tended to decreased over the first 15 minutes, and no further reduction was observed between 15 and 30 minutes.

8.3.3 Pre-incubation with microbubbles reduces NF-kB expression in LPS-induced RAW264.7 cells

Microbubbles with different gas cores (i.e., PFB, PFP, or SF_6) were tested for their ability to reduce NF-kB expression in RAW264.7 cells (Figure 8.5). It was found that microbubbles with PFB or PFP gas cores had significantly reduced NF-kB expressions, while microbubbles with SF_6 gas cores did not show a significant difference ($p < 0.05$). The lack of reduction in NF-kB expression in the SF_6 gas-cored microbubbles was attributed to the poor stability of the SF_6-core microbubbles (Figure 8.5D). The number of microbubbles with SF_6 gas core had dropped to 25 % and 0 % in the first 5 and 30 minutes, respectively. On the other hand, microbubbles with PFB or PFP gas core, after 30 minutes of incubation, reduced to 71 % or 44 %, respectively. The poor stability of SF_6 microbubbles suggested that fewer microbubbles were available to interact with the cells, and this correlated with the insignificant reduction in NF-kB expression compared to the negative control.

The lipid suspension showed an no significant difference in NF-kB expression compared to the negative control (Figure 8.5A, B, and C). The lipid suspension was deduced to be composed of lipidic supramolecular (e.g., liposomes, micelles, and/or multilamellar structures) and free lipid molecules, and the difference to the microbubble suspension, which was unwashed in this experiment, was suspected to be the presence of microbubbles. In other words, microbubble suspension had a very similar chemical composition as the lipid suspension except for the presence of microbubbles. This suggested that the presence of microbubbles was crucial to reduce NF-kB expression in LPS-induced RAW264.7 macrophages and could further argue that supramolecular presentation of the lipid components (i.e., DPPC, DPPG, and palmitic acid) is important in reducing NF-kB expression in LPS-induced RAW264.7 macrophages.

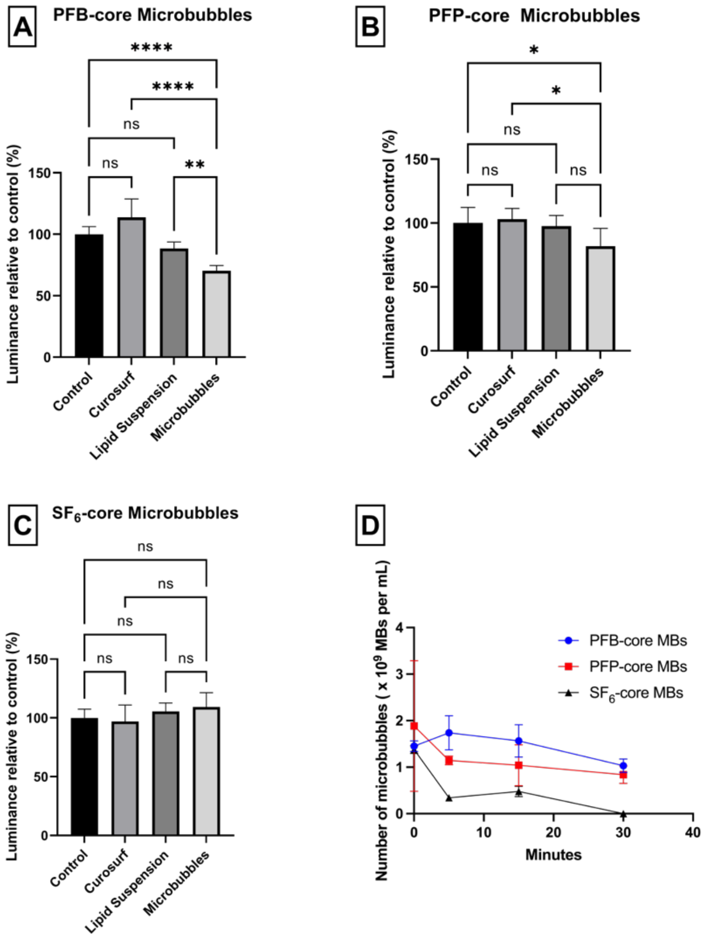

Figure 8.5. NF-kB expression was indirectly measured by quantifying luciferase (NanoLuc) produced by the transfected RAW264.7 macrophages. The macrophages were pre-incubated for 30 minutes with one of the four treatment groups, namely, control (DPBS), Curosurf (poractant alfa, which is the positive control), lipid suspension, and microbubbles. The cells were then washed three times with DPBS, and then were exposed to LPS for 8 hours. (A) Microbubbles with PFB gas core showed significant reduction of NF-kB expression compared to the lipid suspension, poractant alfa, and control ($p < 0.001$). (B) Microbubbles with PFP gas core showed significant difference compared to DPBS and poractant alfa ($p < 0.05$), but not against the lipid suspension. This was because the degree of reduction by the microbubbles with PFP gas core was not as large as the microbubbles with PFB gas core. This may be attributed to the stability and availability of the microbubbles. (C) Lastly, microbubbles with SF_6 gas core did not show a significant reduction in NF-kB expression. (D) Changes in the number of microbubbles were measured for three different microbubbles with different gas cores, namely, PFB, PFP, and SF_6. The microbubbles in the D10 cell culture medium were placed in an incubator, which was at 37 °C in an atmosphere of 5 % CO2 in the air. The number of microbubbles was used as a measure of the stability of the microbubbles. Microbubbles with SF_6 core had the poorest stability, followed by PFP core and then PFB.

8.3.4 Increasing proximity between microbubbles and cells further reduced NF-kB expression

Flipping the 96-well plate upside-down allowed microbubbles to be in closer proximity with the adhered RAW264.7 cells, and thus increasing the likelihood of microbubble-cell interactions. As shown in Figure 8.6, NF-kB expression was significantly lower in RAW264.7 cells that were exposed to microbubbles in the upside-down manner than that in the upright position ($p < 0.05$). This suggested that increasing the proximity of microbubbles to cells had a significant effect on reducing NF-kB expression in LPS-induced RAW264.7 cells.

Increasing the proximity of microbubbles to cells, however, also increases the local lipid concentration near the cells. The significant reduction in NF-kB expression in the upside-down microbubble group may be attributed to the increased lipid concentration near the cell surface. Although this is a possibility, it is unlikely because NF-kB expression did not change when exposed to the lipid suspension (Figure 8.5, Figure 8.6). As discussed above, it was deduced that the supramolecular structures of the lipids determine the immune-modulating effect (Figure 8.5). Thus, increasing the concentrations of supramolecular structures in the lipid suspension (e.g., micelles and/or liposomes) is not anticipated to further reduce NF-kB expression. On the other hand, increasing the exposure of microbubbles to cells by flipping upside-down further reduced NF-kB expression (Figure 8.6), suggesting that microbubble-cell interaction plays a role in reducing NF-kB expression in LPS-induced RAW264.7 cells.

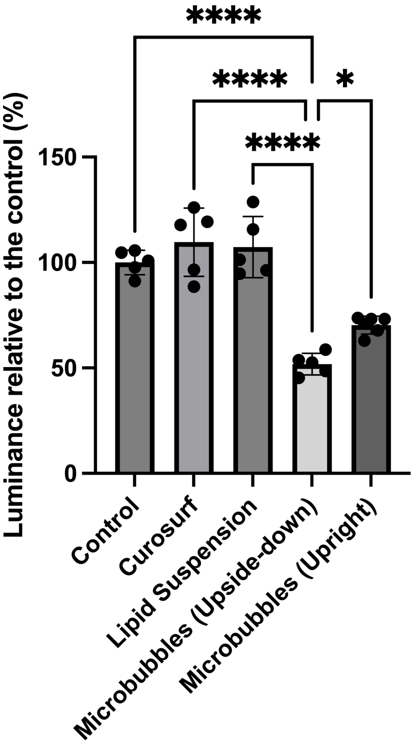

Figure 8.6. NF-kB expression was indirectly measured by quantifying luciferase (NanoLuc). The first four treatment groups from the left (namely, Control, Curosurf, Lipid Suspension, and Microbubbles (Upside-down)) were tested on the same 96-well plate in an upside-down manner. The last treatment group (i.e., Microbubbles (Upright)) was conducted on a separate 96-well plate but on the same day. Microbubbles (Upside-down) showed significantly lower NF-kB expression than the Control (negative control), Curosurf (poractant alfa, positive control), or Lipid Suspension ($p < 0.0001$). Microbubbles (Upside-down) had significantly lower NF-kB expression than Microbubble (Upright) group ($p < 0.05$).

8.3.5 Correlation between the number of microbubbles and NF-kB expression

An increase in the number of microbubbles produced a clear reduction in NF-kB expression in the LPS-induced RAW264.7 cells (Figure 8.7). However, fitting the data to a three-parameter dose-response curve showed a low coefficient of determination ($R^2 = 0.33$). A dose-response curve of a strong anti-inflammatory drug would show a dramatic immunosuppressive action against LPS and would usually have a higher coefficient of determination for the dose-response curve ([256], [257]). The results, thus, suggest: 1) microbubbles, despite their immuno-modulatory effect against LPS, are not comparable to strong anti-inflammatory drugs such as corticosteroids, and 2) the mechanism of action by which microbubbles produce an immunomodulatory effect is suspected to only partially reduce inflammation in LPS-induced RAW264.7 cells.

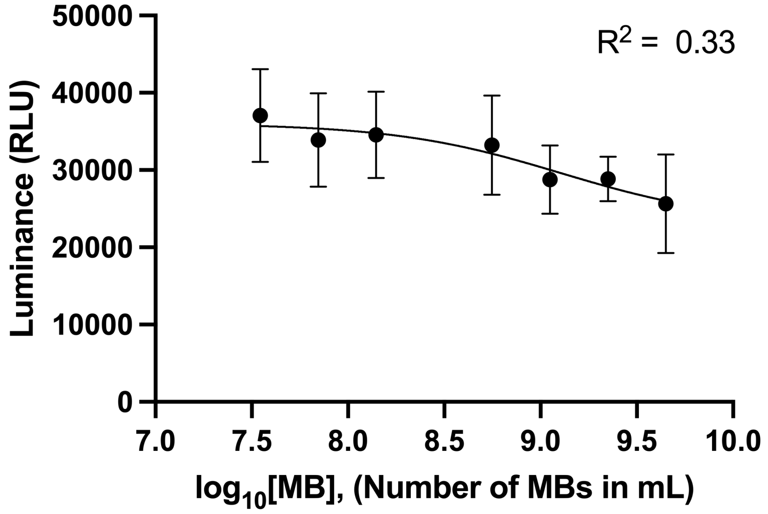

Figure 8.7. The correlation between the number of microbubbles and NF-kB expression in LPS-exposed RAW264.7 cells is shown. Although NF-kB expression was reduced with the increases in the number of microbubbles, the coefficient of determination (R^2) of the dose-response curve was low ($R^2 = 0.33$).

8.3.6 Pre-treatment with microbubbles led to a reduction in the release of some inflammatory mediators

The release of IFN-α, IFN-β, TNF-α, IL-6, and IL-12, which are downstream inflammatory mediators of NF-kB, were quantified after RAW264.7 macrophages were stimulated by LPS. IFN-α, IL-6, and IL-12 were not detected and were excluded from the study. TNF-α and IFN-β were released, and thus, the two mediators were used to examine the effect of surfactants (i.e., poractant alfa, lipid suspension, or microbubbles) on the release of TNF-α and IFN-β after LPS exposure.

IFN-β release by RAW264.7 cells was significantly reduced by pre-incubation with poractant alfa ($p < 0.01$) and the microbubbles ($p < 0.05$). Microbubbles reduced the NF-kB expression (Figure 8.8A), which correlated with the reduction of IFN-β expression (Figure 8.8B). On the other hand, poractant alfa did not reduce NF-kB expression but still reduced the amount of IFN-β release. This implied that the lung surfactant proteins in poractant alfa may be inhibiting the production of the cytokines by suppressing a pathway(s) that is independent of NF-kB and has been reported in previous studies [258], [259], [260], [261].

Pre-incubation of cells with the surfactants (i.e., poractant alfa, lipid suspension, or microbubbles) had no significant effect on TNF-α expression. It was surprising to find that the microbubbles did not reduce TNF-α expression in RAW264.7 macrophages, given that they reduced NF-kB expression.

The clinical translatability of the results is challenging to predict. The immunomodulatory impact of microbubbles was similar to that of poractant alfa, which is considered the benchmark therapy for nRDS and is also employed as a preventive measure for pneumonia. However, the interplay between granulocytes and lymphocytes can lead to diverse outcomes. In vivo studies would be needed to fully explore the immunomodulatory potential of microbubbles.

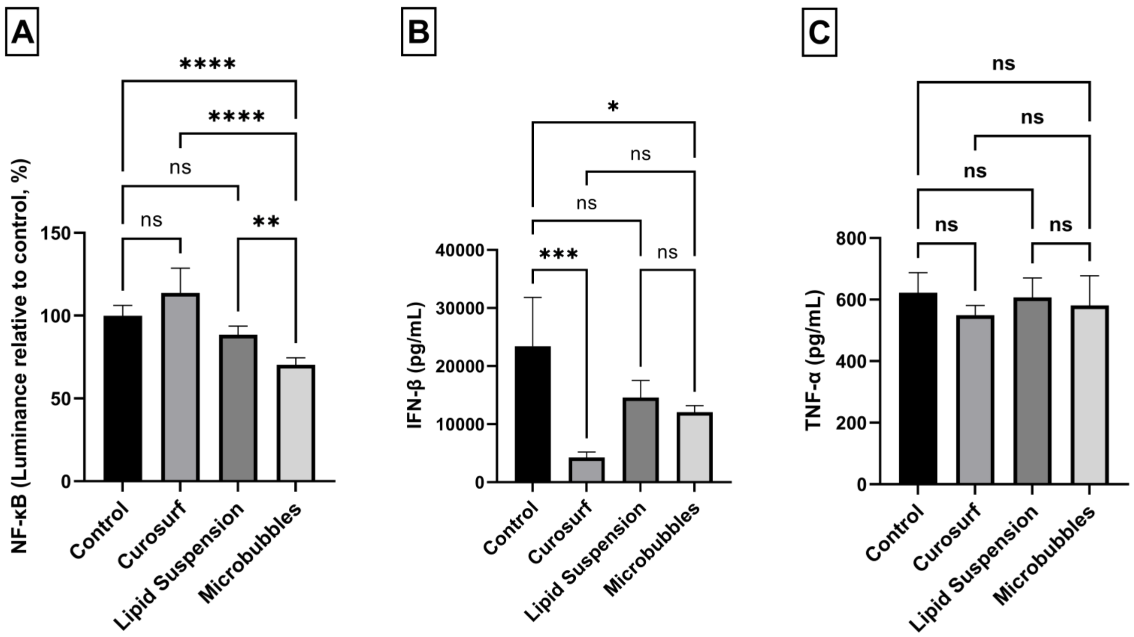

Figure 8.8. Inflammatory mediators released by LPS-induced RAW264.7 cells after pre-incubation were quantified. Four treatment groups were DPBS (i.e., Control), poractant alfa (i.e., Curosurf), lipid suspension, and microbubbles. Duration of the exposure was 8 hours for NF-kB, and 12 hours for IFN-b and TNF-α. The RAW264.7 cells did not release IFN-α, IL-6, and IL-12 after 8 hours of LPS exposure, and thus, these inflammatory mediators were not included in the figures. (A) The degree of NF-kB expression was measured. (B) IFN-β was quantified. (C) TNF-α was quantified.

8.3.7 The effect of co-incubation of microbubbles and LPS on LPS-induced inflammation in RAW264.7 macrophages

RAW264.7 macrophages were co-incubated with LPS and one of poractant alfa, lipid suspension, or microbubbles, and their effect on LPS-induced inflammation in RAW264.7 cells was quantified. Co-incubation of cells with microbubbles and LPS significantly reduced NF-kB and IFN-β expressions ($p < 0.01$) but did not significantly change TNF-α expression. This was consistent with the results observed in the pre-incubation study (Figure 8.8).

On the other hand, co-incubation of RAW264.7 macrophages with lipid suspension significantly reduced NF-kB, IFN-β, and TNF-α expressions ($p < 0.01$), while pre-incubation of RAW264.7 macrophages with lipid suspension did not affect NF-kB, IFN-β, and TNF-α expressions. There are a number of possible explanations. The first of which is the binding of supramolecular structures in the lipid suspension (e.g., liposomes, micelles, and/or etc.) to LPS, which decreases the number of free or active LPS molecules [262]. The second possible explanation is that the lipid supramolecular structures interact with the cell membranes and reduce the translocation of TLR4 receptors [263], but its effect is only observed in the co-incubation group because the interaction is momentary and is reversed when washed with DPBS in the pre-incubation group. The mechanism of the immunomodulatory action against LPS could be further investigated in future studies.

Poractant alfa did not significantly affect NF-kB expression, but significantly reduced IFN-β and TNF-α expressions ($p < 0.01$) in LPS-induced RAW264.7. This again suggested that the mechanism of immunomodulatory effect by poractant alfa may be independent of NF-kB pathway. NF-kB is expressed when LPS molecules bind to TLR4 receptors, and no significant reduction in NF-kB expression suggests that the degree of LPS binding to TLR4 receptors did not significantly change when poractant alfa was present in the culture media. Poractant alfa contains very little to no SP-A and SP-D, which play important roles in opsonising LPS molecules [258], [261], [264]. The lack of SP-A and SP-D in poractant alfa helps to explain the lack of significant reduction in NF-kB expression.

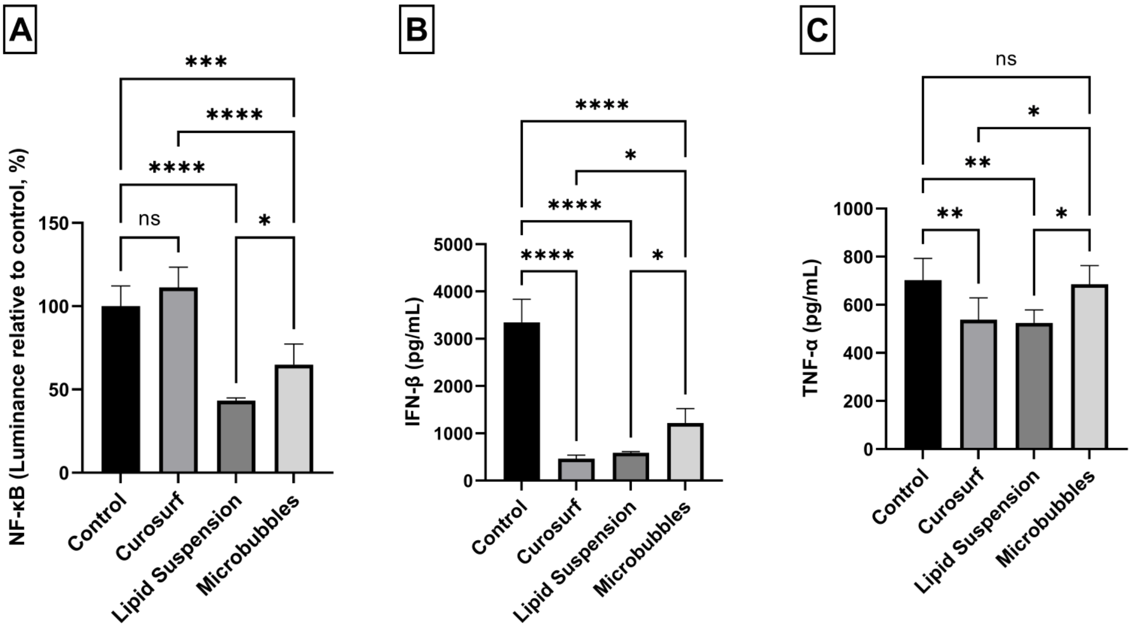

Figure 8.9. Inflammatory mediators released by LPS-induced RAW264.7 cells after pre-incubation were quantified. Four treatment groups were DPBS (i.e., Control), poractant alfa (i.e., Curosurf), lipid suspension, and microbubbles. The duration of exposure was 8 hours for NF-kB, and 12 hours for IFN-α and TNF-α. (A) The degree of NF-kB expression was measured. (B) IFN-β was quantified. (C) TNF-α was quantified.

8.4 Limitations and Future Studies

The hypothesis that microbubbles may reduce LPS-induced inflammation was based on studies that have shown that lung surfactant proteins reduced the translocation of TLR4 receptors [263]. Although this study has shown that microbubbles have immunomodulatory action against LPS in RAW264.7, the underlying mechanism is unknown. Future investigations will aim to elucidate this mechanism by exploring the interaction between cells and microbubbles through imaging techniques. Specifically, the effect of this interaction on cell membrane fluidity and subsequent changes in TLR4 receptor translocation will be studied. Such research may contribute to the development of novel therapies for inflammatory diseases.

8.5 Conclusion

The results of this study indicate that pre-incubation or co-incubation with microbubbles can effectively reduce the amount of inflammatory mediators released by LPS-induced RAW264.7 macrophages. The degree of reduction in NF-kB expression was observed to depend on the proximity of microbubbles and cells, and the stability and the number of microbubbles. This suggests that the interaction between cells and microbubbles may be responsible for the observed immunomodulatory effect. However, the exact mechanism was not investigated in this study, and further studies are required to determine this.

Chapter 9 Conclusions and future work

9.1 Discussion and Conclusions

The aim of this thesis was to explore the potential applications of microbubbles in the context of drug delivery for the treatment of respiratory conditions. Notably, microbubbles have been extensively used as ultrasound contrast agents and have exhibited promising results for clinical applications, particularly in cancer therapy, biofilm disruption, and heart diseases. However, their potential as a therapy for respiratory conditions has not been extensively discussed in the literature. This lack of discussion can be attributed to the inherent difficulty in targeting ultrasound on the lungs due to strong reflection at the air-tissue interface caused by the air sacs in the lungs.

Central to this project is the fact that microbubbles are not exclusively reliant on ultrasound to facilitate their therapeutic effects. It has been observed that microbubbles can be efficacious in their own right, prompting the exploration of their potential applications in the realm of therapeutics [224], [265], [266].

The initial application investigated in Chapters 2-4 was the use of microbubbles for the treatment of asthma and COPD. In Chapter 3, an *in silico* whole lung particle deposition model was developed. Using this model, it was shown in Chapter 4 that the breathing profile is, in fact, the key factor in achieving drug targeting to the small conducting airways and that a means of manipulating this would be a more effective solution than microbubbles. Therefore, the research on the use of inhalable microbubbles for the treatment of asthma/COPD treatment was terminated.

In the second half of the thesis, a different application was investigated. Following a thorough literature review, the use of nebulised lung surfactant therapy in nRDS was identified as a potentially appropriate application. Despite being tried for several decades, the therapy has been largely unsuccessful due to poor lung drug delivery to preterm infants. The consensus among experts was that improving the delivery of lung surfactants to the lungs of preterm infants is essential for the success of nebulised treatments. Microbubbles, due to their low density, were speculated to minimise extrathoracic deposition in adults. This low density reduces the aerodynamic diameter, which in turn is known to improve lung drug delivery to preterm neonates' lungs [194]. In Chapter 6, this hypothesis was tested by measuring the change in aerodynamic diameter when microbubbles were included inside particles and then measuring extrathoracic deposition in preterm neonates. The results showed that incorporating microbubbles in an aerosol significantly improved airway penetration.

Chapter 7 discusses the use of phospholipid-shelled microbubbles as a potential replacement for animal-extracted lung surfactants in the treatment of nRDS. Studies have shown that microbubbles can significantly reduce dynamic surface tension in both clean air-aqueous interfaces and simulated lung fluid under compression. The effect of microbubbles on surface tension was observed in various experiments. Three different formulations of microbubbles (DPPC/PEG40-S, poractant alfa, and PEG-free formulation) were tested, and they all reduced the minimum surface tension of an air-aqueous interface during compression compared to the corresponding lipid suspension. The minimum surface tension reached during the compression phase was found to be dependent on the concentration of the number of microbubbles in the subphase.

The efficacy of microbubbles in reducing air-liquid interfacial surface tension and their potential for improving lung compliance and restoring healthy lung alveolar function requires further investigation. In the context of a healthy adult lung, a 15% reduction in surface area results in an air-liquid interfacial surface tension of approximately 3 mN/m [139], which suggests the presence of high concentrations of lung surfactants in the alveoli. In Chapters 6 and 7, microbubbles were found to reduce the minimum surface tension to nearly 0 mN/m after a 55% reduction in surface area, while the minimum surface tension after a 20% reduction in surface area was found to be 20 mN/m. This finding suggests that very high concentrations of microbubbles may be required to achieve therapeutic efficacy. This would pose a challenge for delivery. However, it is possible that even moderate concentrations of microbubbles could be sufficient to prevent atelectasis in preterm infants' airways, ultimately improving the survival rate in preterm neonates.

In Chapter 8, an investigation was carried out to explore the potential of microbubbles as a modulator of inflammation against Lipopolysaccharide (LPS). The hypothesis that microbubbles could modulate immune response was based on the observation that microbubbles can fuse with cell membranes, thereby altering their fluidity and potentially leading to a reduction in the translocation of TLR4 receptors. This would be expected to lead to a reduction in the binding of LPS molecules to the TLR4 receptors, resulting in a decrease in the production of inflammatory mediators by macrophages, consequently reducing the risk of sepsis. The results revealed that microbubbles did have an immunomodulatory effect against LPS in RAW 264.7 macrophages, which was found to be correlated to the proximity of the microbubbles to the cells and their concentration.

9.2 Future work

The findings presented in this thesis suggest that microbubbles do have the potential to enhance drug delivery to the lungs, in particular, the delivery of nebulised lung surfactants for treating nRDS. However, further work is needed to understand the detailed mechanisms underpinning the observed effects:

The experiments described in Chapter 6 have shown that microbubble-laden aerosols, characterised by lower particle aerodynamic diameters, exhibit enhanced lung penetration in 3D-printed preterm neonate models compared to conventional aerosols. However, accurately quantifying the DPPC content in each aerosol size group could provide valuable insights into the aerosol cut-off diameter beyond which lung deposition is hindered.

Chapter 7 revealed that microbubbles were effective in reducing the surface tension of the air-liquid interface in simulated lung fluid under compression. This effect is crucial for preventing the collapse of the airway or alveoli. The microscopic examination and literature review suggested that the reduction in surface tension during compression was due to the rupture of foam. However, a study that involves the transfer of fluorescently labelled phospholipids from microbubbles to the air-liquid interfacial monolayer upon foam rupture would provide further evidence to support this claim.

Chapter 8 demonstrated microbubbles' immunomodulating ability in LPS-induced macrophages but did not investigate the underlying mechanisms. The current hypothesis is that microbubbles fuse with the cell membrane and alter its fluidity, thereby impeding the translocation of TLR4 receptors on the cell membrane. Light sheet microscopy and spectroscopy using dyes such as C-Laurdan have been employed previously to visualise microbubble-cell membrane fusion and to quantify changes in membrane fluidity [224], [225], [265], [266]. These techniques could be utilised in combination with fluorescently labelled TLR4 antibodies to monitor the temporal variation in TLR4 concentration on the cell membrane and thus test the hypothesis.

Upon elucidation of the underlying mechanisms, a proof-of-concept study could be conducted utilising SP-B deficient mice models. These models exhibit a deficiency in SP-B proteins, which results in elevated surface tension at the air-water interface of the lungs, consequently leading to compromised lung compliance and impaired blood oxygenation. Microbubble-laden aerosols would need to be compared with intratracheal administration of poractant alfa to assess their efficacy in improving oxygenation, lung compliance, and median survival duration following treatment. Secondary outcomes would include inflammation markers in the lungs via bronchoalveolar lavage and lung histology to evaluate the structure of alveoli.

An ideal in vivo model for lung surfactant aerosol delivery to spontaneously breathing preterm infants should possess certain characteristics of an immature respiratory system, such as surfactant deficiency, immature lung structure, low lung compliance, high tissue resistance, and periodic breathing. Studies should be conducted using non-invasive ventilators, ideally with devices used at the neonatal intensive care unit (NICU), and the same nebulizers intended for human use. With such a model and preclinical facility, researchers can test the efficacy, as well as the lung deposition and pulmonary distribution of aerosolized drugs. While an idealized animal model is not currently available, several animal models with distinct features must be used to address different aspects of therapy feasibility, pharmacology, and lung deposition and distribution of a given aerosolized drug.

Lambs and rabbits delivered prematurely by caesarean-section are commonly used animal models to study lung development. The premature lamb model, specifically, has played a crucial role in the development of surfactant therapy and is considered the gold standard for mimicking the initial pathophysiological steps of respiratory distress syndrome (RDS) [267], [268], [269]. This model has been used for various purposes, such as comparing the efficacy of different surfactant types, testing anti-inflammatory drugs, gaining insights into the inflammatory process of RDS, and investigating the effects of intratracheally delivered drugs [270], [271], [272]. Spontaneously breathing premature lambs can also be supported with non-invasive ventilation, monitored with NICU equipment, and integrated with nebulizer devices within the ventilation circuit [273]. However, despite its usefulness, the preterm lamb model is not without limitations. One of the main challenges is the significant inter-subject variability, which can lead to the need for larger sample sizes and make the model less cost-effective.

In certain settings, such as preclinical research or academic environments, conducting expensive experiments with a large sample number of preterm lambs may not be practical. However, there are additional methods to demonstrate proof of concept that can be more effective (without having to increase the sample size). For instance, imaging particle distribution in animal lungs can be used to show the efficacy of microbubble-laden aerosols for improving lung delivery. Gamma scintigraphy following nebulization of 99m-technetium (99mTc)-labelled phospholipids can help in studying lung deposition in preterm lambs. By utilizing imaging techniques, it will be possible to provide additional evidence supporting the effectiveness of microbubble-laden aerosols for improving lung delivery and treatment of nRDS.

Chapter 10 References

[1] R. Sanwal, K. Joshi, M. Ditmans, S. S. H. Tsai, and W. L. Lee, "Ultrasound and microbubbles for targeted drug delivery to the lung endothelium in ARDS: cellular mechanisms and therapeutic opportunities," *Biomedicines*, vol. 9, no. 7, p. 803, 2021.

[2] M. G. Sugiyama *et al.*, "Lung ultrasound and microbubbles enhance aminoglycoside efficacy and delivery to the lung in Escherichia coli–induced pneumonia and acute respiratory distress syndrome," *Am J Respir Crit Care Med*, vol. 198, no. 3, pp. 404–408, 2018.

[3] M. Yanai, K. Sekizawa, T. Ohrui, H. Sasaki, and T. Takishima, "Site of airway obstruction in pulmonary disease: direct measurement of intrabronchial pressure," *J Appl Physiol*, vol. 72, no. 3, pp. 1016–1023, 1992.

[4] M. Kraft, R. Djukanovic, S. Wilson, S. T. Holgate, and R. J. Martin, "Alveolar tissue inflammation in asthma.," *Am J Respir Crit Care Med*, vol. 154, no. 5, pp. 1505–1510, 1996.

[5] N. Carroll, C. Cooke, and A. James, "The distribution of eosinophils and lymphocytes in the large and small airways of asthmatics," *European respiratory journal*, vol. 10, no. 2, pp. 292–300, 1997.

[6] M. Yanai, K. Sekizawa, T. Ohrui, H. Sasaki, and T. Takishima, "Site of airway obstruction in pulmonary disease: direct measurement of intrabronchial pressure," *J Appl Physiol*, vol. 72, no. 3, pp. 1016–1023, 1992, doi: 10.1152/jappl.1992.72.3.1016.

[7] J. E. McDonough *et al.*, "Small-airway obstruction and emphysema in chronic obstructive pulmonary disease," *New England Journal of Medicine*, vol. 365, no. 17, pp. 1567–1575, 2011, doi: 10.1056/NEJMoa1106955.

[8] N. T. Tgavalekos *et al.*, "Identifying airways responsible for heterogeneous ventilation and mechanical dysfunction in asthma: an image functional modeling approach," *J Appl Physiol*, vol. 99, no. 6, pp. 2388–2397, 2005.

[9] N. T. Tgavalekos *et al.*, "Identifying airways responsible for heterogeneous ventilation and mechanical dysfunction in asthma: an image functional modeling approach," *J Appl Physiol*, vol. 99, no. 6, pp. 2388–2397, 2005.

[10] D. P. Tashkin, "The role of small airway inflammation in asthma," in *Allergy and asthma proceedings*, OceanSide Publications, 2002, p. 233.

[11] O. S. Usmani, "Small-airway disease in asthma: pharmacological considerations," *Curr Opin Pulm Med*, vol. 21, no. 1, pp. 55–67, 2015.

[12] R. L. Walenga and P. W. Longest, "Current inhalers deliver very small doses to the lower tracheobronchial airways: assessment of healthy and constricted lungs," *J Pharm Sci*, vol. 105, no. 1, pp. 147–159, 2016.

[13] M. Hoshino, “Comparison of effectiveness in ciclesonide and fluticasone propionate on small airway function in mild asthma,” *Allergology International*, vol. 59, no. 1, pp. 59–66, 2010.

[14] E. F. Juniper, D. B. Price, P. A. Stampone, J. P. H. M. Creemers, S. J. M. Mol, and P. Fireman, “Clinically important improvements in asthma-specific quality of life, but no difference in conventional clinical indexes in patients changed from conventional beclomethasone dipropionate to approximately half the dose of extrafine beclomethasone dipropion,” *Chest*, vol. 121, no. 6, pp. 1824–1832, 2002.

[15] M. G. Levitzky, *Pulmonary physiology*, no. 1. : McGraw-Hill Education, 2018.

[16] E. R. Weibel and D. M. Gomez, “A principle for counting tissue structures on random sections,” *J Appl Physiol*, vol. 17, no. 2, pp. 343–348, 1962.

[17] E. R. Weibel, “Morphometry of the human lung.” Springer, Berlin, pp. xi, 151 p., 1963.

[18] F. Rohrer, “Flow resistance in human air passages and the effect of irregular branching of the bronchial system on the respiratory process in various regions of the lungs,” *Arch Ges Physiol*, vol. 162, pp. 225–299, 1915.

[19] R. Otto G., H. Yeh, G. M. Schum, and R. F. Phalen, “Tracheobronchial Geometry: Human, Dog, Rat, Hamster - A Compilation of Selected Data from the Project Respiratory Tract Deposition Models,” *U.S. Government Printing Office*, 1976.

[20] H.-C. Yeh and G. M. Schum, “Models of human lung airways and their application to inhaled particle deposition,” *Bull Math Biol*, vol. 42, no. 3, pp. 461–480, 1980.

[21] L. Koblinger and W. Hofmann, “Monte Carlo modeling of aerosol deposition in human lungs. Part I: Simulation of particle transport in a stochastic lung structure,” *J Aerosol Sci*, vol. 21, no. 5, pp. 661–674, 1990.

[22] W. Hofmann, B. Asgharian, and R. Winkler-Heil, “Modeling intersubject variability of particle deposition in human lungs,” *J Aerosol Sci*, vol. 33, no. 2, pp. 219–235, 2002.

[23] L. Koblinger, “Analysis of human lung morphometric data for stochastic aerosol deposition calculations,” *Phys Med Biol*, vol. 30, no. 6, p. 541, 1985.

[24] S. Anjilvel and B. Asgharian, “A multiple-path model of particle deposition in the rat lung,” *Fundamental and Applied Toxicology*, vol. 28, no. 1, pp. 41–50, 1995.

[25] S. Montesantos *et al.*, “Airway morphology from high resolution computed tomography in healthy subjects and patients with moderate persistent asthma,” *Anat Rec*, vol. 296, no. 6, pp. 852–866, 2013.

[26] Y. Kim, S. S. Narayanan, and K. S. Nayak, “Accelerated three-dimensional upper airway MRI using compressed sensing,” *Magnetic Resonance in Medicine: An Official Journal of the International Society for Magnetic Resonance in Medicine*, vol. 61, no. 6, pp. 1434–1440, 2009.

[27] K. Pirilä-Parkkinen, H. Löppönen, P. Nieminen, U. Tolonen, E. Pääkkö, and P. Pirttiniemi, “Validity of upper airway assessment in children: a clinical, cephalometric, and MRI study,” *Angle Orthod*, vol. 81, no. 3, pp. 433–439, 2011.

[28] K. Horsfield and G. Cumming, “Morphology of the bronchial tree in man.,” *J Appl Physiol*, vol. 24, no. 3, pp. 373–383, 1968.

[29] S. Montesantos, I. Katz, M. Pichelin, and G. Caillibotte, “The creation and statistical evaluation of a deterministic model of the human bronchial tree from HRCT images,” *PLoS One*, vol. 11, no. 12, pp. 18–21, 2016, doi: 10.1371/journal.pone.0168026.

[30] J. P. Schreider and O. G. Raabe, “Structure of the human respiratory acinus,” *American Journal of Anatomy*, vol. 162, no. 3, pp. 221–232, 1981.

[31] B. Haefeli-Bleuer and E. R. Weibel, “Morphometry of the human pulmonary acinus,” *Anat Rec*, vol. 220, no. 4, pp. 401–414, 1988.

[32] J. E. Hansen and E. P. Ampaya, “Human air space shapes, sizes, areas, and volumes,” *J Appl Physiol*, vol. 38, no. 6, pp. 990–995, 1975.

[33] M. Ochs *et al.*, “The number of alveoli in the human lung,” *Am J Respir Crit Care Med*, vol. 169, no. 1, pp. 120–124, 2004.

[34] P. G. Koullapis, S. C. Kassinos, M. P. Bivolarova, and A. K. Melikov, “Particle deposition in a realistic geometry of the human conducting airways: Effects of inlet velocity profile, inhalation flowrate and electrostatic charge,” *J Biomech*, vol. 49, no. 11, pp. 2201–2212, 2016.

[35] Y. Xie, P. W. Longest, Y. H. Xu, J. P. Wang, and T. S. Wiedmann, “In vitro and in vivo lung deposition of coated magnetic aerosol particles,” *J Pharm Sci*, vol. 99, no. 11, pp. 4658–4668, 2010.

[36] A. V Kolanjiyil and C. Kleinstreuer, “Nanoparticle mass transfer from lung airways to systemic regions—part I: Whole-lung aerosol dynamics,” *J Biomech Eng*, vol. 135, no. 12, 2013.

[37] B. Asgharian, W. Hofmann, and R. Bergmann, “Particle deposition in a multiple-path model of the human lung,” *Aerosol Science and Technology*, vol. 34, no. 4, pp. 332–339, 2001, doi: 10.1080/02786820119122.

[38] Q. Deng, L. Deng, Y. Miao, X. Guo, and Y. Li, “Particle deposition in the human lung: Health implications of particulate matter from different sources,” *Environ Res*, vol. 169, pp. 237–245, 2019.

[39] H. D. Landahl, “On the removal of air-borne droplets by the human respiratory tract: I. The lung,” *Bull Math Biophys*, vol. 12, no. 1, pp. 43–56, 1950.

[40] F. S. Cai and C. P. Yu, “Inertial and interceptional deposition of spherical particles and fibers in a bifurcating airway,” *J Aerosol Sci*, vol. 19, no. 6, pp. 679–688, 1988.

[41] H.-C. Yeh, “Use of a heat transfer analogy for a mathematical model of respiratory tract deposition,” *Bull Math Biol*, vol. 36, pp. 105–116, 1974.

[42] C. S. KIM and A. J. IGLESIAS, “Deposition of inhaled particles in bifurcating airway models: I. Inspiratory deposition,” *Journal of Aerosol Medicine*, vol. 2, no. 1, pp. 1–14, 1989.

[43] J. Pich, “Theory of gravitational deposition of particles from laminar flows in channels,” *J Aerosol Sci*, vol. 3, no. 5, pp. 351–361, 1972.

[44] C.-S. Wang, "Gravitational deposition of particles from laminar flows in inclined channels," *J Aerosol Sci*, vol. 6, no. 3–4, pp. 191–204, 1975.

[45] J. M. Beeckmans, "The deposition of aerosols in the respiratory tract: I. Mathematical analysis and comparison with experimental data," *Can J Physiol Pharmacol*, vol. 43, no. 1, pp. 157–172, 1965.

[46] D. B. Ingham, "Diffusion of aerosols from a stream flowing through a cylindrical tube," *J Aerosol Sci*, vol. 6, no. 2, pp. 125–132, 1975.

[47] W. Nusselt, "The dependence of the heat transfer coefficient on tube length," *Zeit. VDI*, vol. 54, pp. 1154–1158, 1910.

[48] Z. Zhang, C. Kleinstreuer, and C. S. Kim, "Comparison of analytical and CFD models with regard to micron particle deposition in a human 16-generation tracheobronchial airway model," *J Aerosol Sci*, vol. 40, no. 1, pp. 16–28, 2009.

[49] D. O'Connor *et al.*, "Role of pharmacokinetics in establishing bioequivalence for orally inhaled drug products: workshop summary report," *J Aerosol Med Pulm Drug Deliv*, vol. 24, no. 3, pp. 119–135, 2011.

[50] J. Conway, "Lung imaging—two dimensional gamma scintigraphy, SPECT, CT and PET," *Adv Drug Deliv Rev*, vol. 64, no. 4, pp. 357–368, 2012.

[51] W. Stahlhofen, R. Koebrich, G. Rudolf, and G. Scheuch, "Short-term and long-term clearance of particles from the upper human respiratory tract as function of particle size," *J Aerosol Sci*, vol. 21, pp. S407–S410, 1990.

[52] A. Livraghi and S. H. Randell, "Cystic fibrosis and other respiratory diseases of impaired mucus clearance," *Toxicol Pathol*, vol. 35, no. 1, pp. 116–129, 2007.

[53] J. Heyder, J. Gebhart, G. Rudolf, C. F. Schiller, and W. Stahlhofen, "Deposition of particles in the human respiratory tract in the size range 0.005–15 µm," *J Aerosol Sci*, vol. 17, no. 5, pp. 811–825, 1986.

[54] B. Asgharian, W. Hofmann, and R. Bergmann, "Particle deposition in a multiple-path model of the human lung," *Aerosol Science & Technology*, vol. 34, no. 4, pp. 332–339, 2001, doi: 10.1080/02786820119122.

[55] S. Montesantos, I. Katz, M. Pichelin, and G. Caillibotte, "The creation and statistical evaluation of a deterministic model of the human bronchial tree from HRCT images," *PLoS One*, vol. 11, no. 12, pp. 18–21, 2016, doi: 10.1371/journal.pone.0168026.

[56] S. Montesantos *et al.*, "Airway morphology from high resolution computed tomography in healthy subjects and patients with moderate persistent asthma," *Anat Rec*, vol. 296, no. 6, pp. 852–866, 2013, doi: 10.1002/ar.22695.

[57] O. G. Raabe, H. Yeh, G. M. Schum, and R. F. Phalen, "Tracheobronchial Geometry: Human, Dog, Rat, Hamster - A Compilation of Selected Data from the Project Respiratory Tract Deposition Models," 1976.

[58] M. Takahashi *et al.*, "How accurate is CT morphometry of airway? Phantom and clinical validation study," *Eur J Radiol*, vol. 80, no. 3, pp. e524–e530, 2011, doi: 10.1016/j.ejrad.2010.12.035.

[59] L. Koblinger, “Analysis of human lung morphometric data for stochastic aerosol deposition calculations,” *Phys Med Biol*, vol. 30, no. 6, p. 541, 1985, Accessed: Aug. 10, 2023. [Online]. Available: https://doi.org/10.1038/s41372-018-0302-9

[60] L. Koblinger and W. Hofmann, “Analysis of human lung morphometric data for stochastic aerosol deposition calculations,” *Phys Med Biol*, vol. 30, no. 6, p. 541, 1985, doi: 10.1088/0031-9155/30/6/004.

[61] B. Haefeli-Bleuer and E. R. Weibel, “Morphometry of the human pulmonary acinus,” *Anat Rec*, vol. 220, no. 4, pp. 401–414, 1988, doi: 10.1002/ar.1092200410.

[62] E. R. Weibel, A. F. Cournand, and W. R. Dickinson, *Morphometry of the human lung.* Berlin: Springer, 1963.

[63] H. D. Landahl, “On the removal of air-borne droplets by the human respiratory tract: I. The lung,” *Bull Math Biophys*, vol. 12, no. 1, pp. 43–56, 1950, doi: 10.1007/bf02477345.

[64] F. S. Cai and C. P. Yu, “Inertial and interceptional deposition of spherical particles and fibers in a bifurcating airway,” *J Aerosol Sci*, vol. 19, no. 6, pp. 679–688, 1988, doi: 10.1016/0021-8502(88)90003-1.

[65] C.-S. Wang, “Gravitational deposition of particles from laminar flows in inclined channels,” *J Aerosol Sci*, vol. 6, no. 3–4, pp. 191–204, 1975, doi: 10.1016/0021-8502(75)90088-9.

[66] J. M. Beeckmans, “The deposition of aerosols in the respiratory tract: I. Mathematical analysis and comparison with experimental data,” *Can J Physiol Pharmacol*, vol. 43, no. 1, pp. 157–172, 1965, doi: 10.1139/y65-015.

[67] D. B. Ingham, “Diffusion of aerosols from a stream flowing through a cylindrical tube,” *J Aerosol Sci*, vol. 6, no. 2, pp. 125–132, 1975, doi: 10.1016/0021-8502(75)90005-1.

[68] J. Heyder, J. Gebhart, G. Rudolf, C. F. Schiller, and W. Stahlhofen, “Deposition of particles in the human respiratory tract in the size range 0.005–15 µm,” *J Aerosol Sci*, vol. 17, no. 5, pp. 811–825, 1986, doi: 10.1016/0021-8502(86)90035-2.

[69] W. Hofmann, E. Pawlak, and R. Sturm, “Semi-empirical stochastic model of aerosol bolus dispersion in the human lung,” *Inhal Toxicol*, vol. 20, no. 12, pp. 1059–1073, 2008, doi: 10.1080/08958370802115081.

[70] P. Brand, C. Rieger, H. Schulz, T. Beinert, and J. Heyder, “Aerosol bolus dispersion in healthy subjects,” *European Respiratory Journal*, vol. 10, no. 2, pp. 460–467, 1997.

[71] R. F. Phalen, M. J. Oldham, C. B. Beaucage, T. T. Crocker, and J. Mortensen, “Postnatal enlargement of human tracheobronchial airways and implications for particle deposition,” *Anat Rec*, vol. 212, no. 4, pp. 368–380, 1985, doi: 10.1002/ar.1092120408.

[72] M. Montaudon, P. Desbarats, P. Berger, G. De Dietrich, R. Marthan, and F. Laurent, “Assessment of bronchial wall thickness and lumen diameter in human adults using multi-detector computed tomography: comparison with theoretical models,” *J Anat*, vol. 211, no. 5, pp. 579–588, 2007, doi: 10.1111/j.1469-7580.2007.00811.x.

[73] W. Hofmann, “Modelling inhaled particle deposition in the human lung — A review,” *J Aerosol Sci*, vol. 42, no. 10, pp. 693–724, 2011, doi: 10.1016/j.jaerosci.2011.05.007.

[74] M. Hussain, W.-H. Renate, and H. Werner, “Effect of intersubject variability of extrathoracic morphometry, lung airways dimensions and respiratory parameters on particle deposition,” *J Thorac Dis*, vol. 3, no. 3, p. 156, 2011, doi: 10.3978/j.issn.2072-1439.2011.04.03.

[75] H.-C. Yeh and G. M. Schum, “Models of human lung airways and their application to inhaled particle deposition,” *Bull Math Biol*, vol. 42, no. 3, pp. 461–480, 1980, doi: 10.1016/S0092-8240(80)80060-7.

[76] K. Horsfield, G. Dart, D. E. Olson, G. F. Filley, and G. Cumming, “Models of the human bronchial tree.,” *J Appl Physiol*, vol. 31, no. 2, pp. 207–217, 1971, doi: 10.1152/jappl.1971.31.2.207.

[77] H. Kitaoka, R. Takaki, and B. Suki, “A three-dimensional model of the human airway tree,” *J Appl Physiol*, vol. 87, no. 6, pp. 2207–2217, 1999, doi: 10.1152/jappl.1999.87.6.2207.

[78] M. H. Tawhai, A. J. Pullan, and P. J. Hunter, “Generation of an anatomically based three-dimensional model of the conducting airways,” *Ann Biomed Eng*, vol. 28, no. 7, pp. 793–802, 2000, doi: 10.1114/1.1289457.

[79] M. Florens, B. Sapoval, and M. Filoche, “An anatomical and functional model of the human tracheobronchial tree,” *J Appl Physiol*, vol. 110, no. 3, pp. 756–763, 2011, doi: 10.1152/japplphysiol.00984.2010.

[80] W. Hofmann, B. Asgharian, and R. Winkler-Heil, “Modeling intersubject variability of particle deposition in human lungs,” *J Aerosol Sci*, vol. 33, no. 2, pp. 219–235, 2002, doi: 10.1016/S0021-8502(01)00167-7.

[81] M. Ochs *et al.*, “The number of alveoli in the human lung,” *Am J Respir Crit Care Med*, vol. 169, no. 1, pp. 120–124, 2004, doi: 10.1164/rccm.200308-1107OC.

[82] B. J. Delgado and T. Bajaj, *Physiology, Lung Capacity*. Ross University School of Medicine: StatPearls Publishing, Treasure Island (FL), 2020. [Online]. Available: http://europepmc.org/abstract/MED/31082073

[83] L. Borgstrom, E. Bondesson, F. Moren, E. Trofast, and S. P. Newman, “Lung deposition of budesonide inhaled via Turbuhaler: a comparison with terbutaline sulphate in normal subjects,” *European Respiratory Journal*, vol. 7, no. 1, pp. 69–73, 1994, doi: 10.1183/09031936.94.07010069.

[84] S. P. Duddu *et al.*, “Improved lung delivery from a passive dry powder inhaler using an engineered PulmoSphere® powder,” *Pharm Res*, vol. 19, no. 5, pp. 689–695, 2002, doi: 10.1023/A:1015322616613.

[85] S. P. Newman *et al.*, “Scintigraphic comparison of budesonide deposition from two dry powder inhalers,” *European Respiratory Journal*, vol. 16, no. 1, pp. 178–183, 2000, doi: 10.1034/j.1399-3003.2000.16a29.x.

[86] P. T. Macklem and J. Mead, “Resistance of central and peripheral airways measured by a retrograde catheter,” *J Appl Physiol*, vol. 22, no. 3, pp. 395–401, 1967, doi: 10.1152/jappl.1967.22.3.395.

[87] J. C. Hogg, P. T. Macklem, and W. M. Thurlbeck, “Site and nature of airway obstruction in chronic obstructive lung disease,” *New England Journal of Medicine*, vol. 278, no. 25, pp. 1355–1360, 1968, doi: 10.1056/NEJM196806202782501.

[88] J. A. Stockley, B. G. Cooper, R. A. Stockley, and E. Sapey, “Small airways disease: time for a revisit?,” *Int J Chron Obstruct Pulmon Dis*, pp. 2343–2353, 2017, doi: 10.2147/COPD.S138540.

[89] J. C. Hogg *et al.*, “The nature of small-airway obstruction in chronic obstructive pulmonary disease,” *New England Journal of Medicine*, vol. 350, no. 26, pp. 2645–2653, 2004, doi: 10.1056/NEJMoa032158.

[90] P. R. Burgel *et al.*, “Update on the roles of distal airways in COPD,” *European Respiratory Review*, vol. 20, no. 119, pp. 7–22, 2011, doi: 10.1183/09059180.10010610.

[91] H.-K. Koo *et al.*, “Small airways disease in mild and moderate chronic obstructive pulmonary disease: a cross-sectional study,” *Lancet Respir Med*, vol. 6, no. 8, pp. 591–602, 2018, doi: 10.1016/S2213-2600(18)30196-6.

[92] R. L. Walenga and P. W. Longest, “Current inhalers deliver very small doses to the lower tracheobronchial airways: assessment of healthy and constricted lungs,” *J Pharm Sci*, vol. 105, no. 1, pp. 147–159, 2016, doi: 10.1016/j.xphs.2015.11.027.

[93] O. S. Usmani, M. F. Biddiscombe, and P. J. Barnes, “Regional lung deposition and bronchodilator response as a function of β2-agonist particle size,” *Am J Respir Crit Care Med*, vol. 172, no. 12, pp. 1497–1504, 2005, doi: 10.1164/rccm.200410-1414OC.

[94] A. H. De Boer, D. Gjaltema, P. Hagedoorn, and H. W. Frijlink, “Can ‘extrafine’dry powder aerosols improve lung deposition?,” *European Journal of Pharmaceutics and Biopharmaceutics*, vol. 96, pp. 143–151, 2015, doi: 10.1016/j.ejpb.2015.07.016.

[95] L. A. De Backer *et al.*, “Functional imaging using computer methods to compare the effect of salbutamol and ipratropium bromide in patient-specific airway models of COPD,” *Int J Chron Obstruct Pulmon Dis*, pp. 637–646, 2011, doi: 0.2147/COPD.S21917.

[96] D. Singh *et al.*, “Single inhaler triple therapy versus inhaled corticosteroid plus long-acting β2-agonist therapy for chronic obstructive pulmonary disease (TRILOGY): a double-blind, parallel group, randomised controlled trial,” *The Lancet*, vol. 388, no. 10048, pp. 963–973, 2016, doi: 10.1016/S0140-6736(16)31354-X.

[97] M. J. Mäkelä, V. Backer, M. Hedegaard, and K. Larsson, “Adherence to inhaled therapies, health outcomes and costs in patients with asthma and COPD,” *Respir Med*, vol. 107, no. 10, pp. 1481–1490, 2013, doi: 10.1016/j.rmed.2013.04.005.

[98] P. Santus *et al.*, “The relevance of targeting treatment to small airways in asthma and COPD,” *Respir Care*, vol. 65, no. 9, pp. 1392–1412, 2020, doi: 10.4187/respcare.07237.

[99] A. R. Martin, “Regional deposition: targeting,” *J Aerosol Med Pulm Drug Deliv*, vol. 34, no. 1, pp. 1–10, 2021.

[100] S. Häussermann, K. Sommerer, and G. Scheuch, “Regional Lung Deposition: In Vivo Data,” *J Aerosol Med Pulm Drug Deliv*, vol. 33, no. 6, pp. 291–299, 2020, doi: 10.1089/jamp.2020.29032.sh.

[101] M. Anderson, K. Philipson, M. Svartengren, and P. Camner, “Human deposition and clearance of 6-µm particles inhaled with an extremely low flow rate,” *Exp Lung Res*, vol. 21, no. 1, pp. 187–195, 1995.

[102] W. Moller *et al.*, “Deposition, retention, and translocation of ultrafine particles from the central airways and lung periphery,” *Am J Respir Crit Care Med*, vol. 177, no. 4, pp. 426–432, 2008.

[103] P. Brand *et al.*, “Optimum peripheral drug deposition in patients with cystic fibrosis,” *Journal of aerosol medicine*, vol. 18, no. 1, pp. 45–54, 2005.

[104] W. Stahlhofen, G. Rudolf, and A. C. James, “Intercomparison of experimental regional aerosol deposition data,” *Journal of Aerosol Medicine*, vol. 2, no. 3, pp. 285–308, 1989.

[105] A. J. Keane, “Wing optimization using design of experiment, response surface, and data fusion methods,” *J Aircr*, vol. 40, no. 4, pp. 741–750, 2003, doi: 10.2514/2.3153.

[106] O. W. Gooding, “Process optimization using combinatorial design principles: parallel synthesis and design of experiment methods,” *Curr Opin Chem Biol*, vol. 8, no. 3, pp. 297–304, 2004, doi: 10.1016/j.cbpa.2004.04.009.

[107] V. Singh, S. Haque, R. Niwas, A. Srivastava, M. Pasupuleti, and C. Tripathi, “Strategies for fermentation medium optimization: an in-depth review,” *Front Microbiol*, vol. 7, p. 2087, 2017, doi: 10.3389/fmicb.2016.02087.

[108] B. Y. Gajera, D. A. Shah, and R. H. Dave, “Development of an amorphous nanosuspension by sonoprecipitation-formulation and process optimization using design of experiment methodology,” *Int J Pharm*, vol. 559, pp. 348–359, 2019, doi: 10.1016/j.ijpharm.2019.01.054.

[109] J.-P. Charbonnier *et al.*, “Airway wall thickening on CT: relation to smoking status and severity of COPD,” *Respir Med*, vol. 146, pp. 36–41, 2019, doi: 10.1016/j.rmed.2018.11.014.

[110] H. J. Min, E. P. Stride, and S. J. Payne, “in silico investigation of the effect of particle diameter on deposition uniformity in pulmonary drug delivery,” *Aerosol Science and Technology*, no. just-accepted, pp. 1–14, 2023, doi: 10.1080/02786826.2023.2175640.

[111] C. P. Yu, “Exact analysis of aerosol deposition during steady breathing,” *Powder Technol*, vol. 21, no. 1, pp. 55–62, 1978, doi: 10.1016/0032-5910(78)80107-7.

[112] S. Anjilvel and B. Asgharian, “A multiple-path model of particle deposition in the rat lung,” *Fundamental and Applied Toxicology*, vol. 28, no. 1, pp. 41–50, 1995, doi: 10.1006/faat.1995.1144.

[113] L. Golshahi, M. L. Noga, R. Vehring, and W. H. Finlay, “An in vitro study on the deposition of micrometer-sized particles in the extrathoracic airways of adults during tidal oral breathing,” *Ann Biomed Eng*, vol. 41, no. 5, pp. 979–989, 2013, doi: 10.1007/s10439-013-0747-0.

[114] K. Kuga, R. Kizuka, N. D. Khoa, and K. Ito, “Effect of transient breathing cycle on the deposition of micro and nanoparticles on respiratory walls,” *Comput Methods Programs Biomed*, vol. 236, p. 107501, 2023, doi: 10.1016/j.cmpb.2023.107501.

[115] P. G. Mathews, *Design of Experiments with MINITAB*, vol. 446. ASQ Quality Press, 2005.

[116] P. Brand *et al.*, “Lung deposition of radiolabeled tiotropium in healthy subjects and patients with chronic obstructive pulmonary disease,” *The Journal of Clinical Pharmacology*, vol. 47, no. 10, pp. 1335–1341, 2007, doi: 10.1177/0091270006295788.

[117] W. De Backer *et al.*, “Lung deposition of BDP/formoterol HFA pMDI in healthy volunteers, asthmatic, and COPD patients,” *J Aerosol Med Pulm Drug Deliv*, vol. 23, no. 3, pp. 137–148, 2010, doi: 10.1089/jamp.2009.0772.

[118] E. Derom, K. Strandgården, V. Schelfhout, L. Borgström, and R. Pauwels, “Lung deposition and efficacy of inhaled formoterol in patients with moderate to severe COPD,” *Respir Med*, vol. 101, no. 9, pp. 1931–1941, 2007, doi: 10.1016/j.rmed.2007.04.013.

[119] P. Singh, V. Raghav, V. Padhmashali, G. Paul, M. S. Islam, and S. C. Saha, “Airflow and particle transport prediction through stenosis airways,” *Int J Environ Res Public Health*, vol. 17, no. 3, p. 1119, 2020, doi: 10.3390/ijerph17031119.

[120] O. S. Usmani *et al.*, “Seven pillars of small airways disease in asthma and COPD: supporting opportunities for novel therapies,” *Chest*, vol. 160, no. 1, pp. 114–134, 2021, doi: 10.1016/j.chest.2021.03.047.

[121] J. Cohen, W. R. Douma, N. H. T. ten Hacken, J. M. Vonk, M. Oudkerk, and D. S. Postma, “Ciclesonide improves measures of small airway involvement in asthma,” *European Respiratory Journal*, vol. 31, no. 6, pp. 1213–1220, 2008, doi: 10.1183/09031936.00082407.

[122] A. Fischer, J. Stegemann, G. Scheuch, and R. Siekmeier, “Novel devices for individualized controlled inhalation can optimize aerosol therapy in efficacy, patient care and power of clinical trials,” *Eur J Med Res*, vol. 14, no. 4, pp. 1–7, 2009, doi: 10.1186/2047-783X-14-S4-71.

[123] S. Stanojevic *et al.*, “ERS/ATS technical standard on interpretive strategies for routine lung function tests,” *European Respiratory Journal*, vol. 60, no. 1, 2022, doi: 10.1183/13993003.01499-2021.

[124] E. R. Weibel, B. Sapoval, and M. Filoche, “Design of peripheral airways for efficient gas exchange,” *Respir Physiol Neurobiol*, vol. 148, no. 1–2, pp. 3–21, 2005, doi: 10.1016/j.resp.2005.03.005.

[125] A. B. te Pas, C. Wong, C. O. F. Kamlin, J. A. Dawson, C. J. Morley, and P. G. Davis, “Breathing patterns in preterm and term infants immediately after birth,” *Pediatr Res*, vol. 65, no. 3, pp. 352–356, 2009, Accessed: Jan. 16, 2024. [Online]. Available: https://doi.org/10.1203/PDR.0b013e318193f117

[126] J. Perez-Gil and T. E. Weaver, “Pulmonary surfactant pathophysiology: current models and open questions,” *Physiology*, vol. 25, no. 3, pp. 132–141, 2010.

[127] E. Bancalari, “The Newborn Lung: Neonatology Questions and Controversies: Expert Consult.” Philadelphia: Saunders, 2012.

[128] F. Ricci *et al.*, “In Vivo evaluation of the acute pulmonary response to poractant alfa and bovactant treatments in lung-lavaged adult rabbits and in preterm lambs with respiratory distress syndrome,” *Front Pediatr*, vol. 5, p. 186, 2017, Accessed: Jan. 16, 2024. [Online]. Available: https://doi.org/10.3389/fped.2017.00186

[129] D. G. Sweet *et al.*, “European consensus guidelines on the management of respiratory distress syndrome–2019 update,” *Neonatology*, vol. 115, no. 4, pp. 432–450, 2019, Accessed: Jan. 16, 2024. [Online]. Available: https://doi.org/10.1159/000499361

[130] R. Raschetti, R. Centorrino, E. Letamendia, A. Benachi, A. Marfaing-Koka, and D. De Luca, “Estimation of early life endogenous surfactant pool and CPAP failure in preterm neonates

with RDS," *Respir Res*, vol. 20, no. 1, pp. 1–8, 2019, Accessed: Jan. 16, 2024. [Online]. Available: https://doi.org/10.1186/s12931-019-1040-z

[131] C. Papastamelos, H. B. Panitch, S. E. England, and J. L. Allen, "Developmental changes in chest wall compliance in infancy and early childhood," *J Appl Physiol*, vol. 78, no. 1, pp. 179–184, 1995, Accessed: Jan. 16, 2024. [Online]. Available: https://doi.org/10.1152/jappl.1995.78.1.179

[132] M. E. Avery and J. Mead, "Surface properties in relation to atelectasis and hyaline membrane disease," *AMA J Dis Child*, vol. 97, no. 5_PART_I, pp. 517–523, 1959, Accessed: Sep. 27, 2023. [Online]. Available: 10.1001/archpedi.1959.02070010519001

[133] S. B. Ainsworth, "Pathophysiology of neonatal respiratory distress syndrome," *Treat Respir Med*, vol. 4, no. 6, pp. 423–437, 2005, doi: 10.2165/00151829-200504060-00006.

[134] M. Chakraborty and S. Kotecha, "Pulmonary surfactant in newborn infants and children," *Breathe*, vol. 9, no. 6, pp. 476–488, 2013.

[135] S. B. Ainsworth and D. W. A. Milligan, "Surfactant therapy for respiratory distress syndrome in premature neonates: a comparative review," *American Journal of Respiratory Medicine*, vol. 1, pp. 417–433, 2002.

[136] E. Lopez-Rodriguez and J. Pérez-Gil, "Structure-function relationships in pulmonary surfactant membranes: from biophysics to therapy," *Biochimica et Biophysica Acta (BBA)-Biomembranes*, vol. 1838, no. 6, pp. 1568–1585, 2014.

[137] J. B. de la Serna, J. Perez-Gil, A. C. Simonsen, and L. A. Bagatolli, "Cholesterol rules: direct observation of the coexistence of two fluid phases in native pulmonary surfactant membranes at physiological temperatures," *Journal of Biological Chemistry*, vol. 279, no. 39, pp. 40715–40722, 2004.

[138] J. Pérez-Gil, "Structure of pulmonary surfactant membranes and films: the role of proteins and lipid–protein interactions," *Biochimica et Biophysica Acta (BBA)-Biomembranes*, vol. 1778, no. 7–8, pp. 1676–1695, 2008, doi: 10.1016/j.bbamem.2008.05.003.

[139] J. C. Castillo-Sánchez, A. Cruz, and J. Pérez-Gil, "Structural hallmarks of lung surfactant: Lipid-protein interactions, membrane structure and future challenges," *Arch Biochem Biophys*, p. 108850, 2021, doi: 10.1016/j.abb.2021.108850.

[140] B. Olmeda, B. García-Álvarez, and J. Pérez-Gil, "Structure–function correlations of pulmonary surfactant protein SP-B and the saposin-like family of proteins," *European Biophysics Journal*, vol. 42, pp. 209–222, 2013.

[141] J. Liekkinen, G. Enkavi, M. Javanainen, B. Olmeda, J. Pérez-Gil, and I. Vattulainen, "Pulmonary surfactant lipid reorganization induced by the adsorption of the oligomeric surfactant protein B complex," *J Mol Biol*, vol. 432, no. 10, pp. 3251–3268, 2020.

[142] B. Olmeda, B. García-Álvarez, M. J. Gómez, M. Martínez-Calle, A. Cruz, and J. Pérez-Gil, "A model for the structure and mechanism of action of pulmonary surfactant protein B," *The FASEB Journal*, vol. 29, no. 10, pp. 4236–4247, 2015.

[143] E. Parra, L. H. Moleiro, I. Lopez-Montero, A. Cruz, F. Monroy, and J. Pérez-Gil, "A combined action of pulmonary surfactant proteins SP-B and SP-C modulates permeability and dynamics of phospholipid membranes," *Biochemical Journal*, vol. 438, no. 3, pp. 555–564, 2011.

[144] E. Parra, A. Alcaraz, A. Cruz, V. M. Aguilella, and J. Pérez-Gil, “Hydrophobic pulmonary surfactant proteins SP-B and SP-C induce pore formation in planar lipid membranes: evidence for proteolipid pores,” *Biophys J*, vol. 104, no. 1, pp. 146–155, 2013.

[145] M. A. Ryan *et al.*, “Mapping and analysis of the lytic and fusogenic domains of surfactant protein B,” *Biochemistry*, vol. 44, no. 3, pp. 861–872, 2005.

[146] V. Edwards, E. Cutz, S. Viero, A. M. Moore, and L. Nogee, “Ultrastructure of lamellar bodies in congenital surfactant deficiency,” *Ultrastruct Pathol*, vol. 29, no. 6, pp. 503–509, 2005.

[147] L. M. Nogee *et al.*, “A mutation in the surfactant protein B gene responsible for fatal neonatal respiratory disease in multiple kindreds.,” *J Clin Invest*, vol. 93, no. 4, pp. 1860–1863, 1994.

[148] D. Lukovic *et al.*, “Interfacial behavior of recombinant forms of human pulmonary surfactant protein SP-C,” *Langmuir*, vol. 28, no. 20, pp. 7811–7825, 2012.

[149] N. Roldan, T. K. M. Nyholm, J. P. Slotte, J. Pérez-Gil, and B. García-Álvarez, “Effect of lung surfactant protein SP-C and SP-C-promoted membrane fragmentation on cholesterol dynamics,” *Biophys J*, vol. 111, no. 8, pp. 1703–1713, 2016.

[150] R. Arroyo *et al.*, “Supramolecular assembly of human pulmonary surfactant protein SP-D,” *J Mol Biol*, vol. 430, no. 10, pp. 1495–1509, 2018.

[151] N. Palaniyar, R. A. Ridsdale, C. E. Holterman, K. Inchley, F. Possmayer, and G. Harauz, “Structural changes of surfactant protein A induced by cations reorient the protein on lipid bilayers,” *J Struct Biol*, vol. 122, no. 3, pp. 297–310, 1998.

[152] H. Sano and Y. Kuroki, “The lung collectins, SP-A and SP-D, modulate pulmonary innate immunity,” *Mol Immunol*, vol. 42, no. 3, pp. 279–287, 2005.

[153] E. Robillard, Y. Alarie, P. Dagenais-Perusse, E. Baril, and A. Guilbeault, “Microaerosol administration of synthetic β-γ-dipalmitoyl-L-α-lecithin in the respiratory distress syndrome: a preliminary report,” *Can Med Assoc J*, vol. 90, no. 2, p. 55, 1964.

[154] J. J. Pillow and S. Minocchieri, “Innovation in surfactant therapy II: surfactant administration by aerosolization,” *Neonatology*, vol. 101, no. 4, pp. 337–344, 2012.

[155] O. Blanco and J. Pérez-Gil, “Biochemical and pharmacological differences between preparations of exogenous natural surfactant used to treat Respiratory Distress Syndrome: role of the different components in an efficient pulmonary surfactant,” *Eur J Pharmacol*, vol. 568, no. 1–3, pp. 1–15, 2007.

[156] G. Jorch *et al.*, “To the editor: Surfactant aerosol treatment of respiratory distress syndrome in spontaneously breathing premature infants,” *Pediatr Pulmonol*, vol. 24, no. 3, pp. 222–224, 1997.

[157] M. Arrøe, L. Pedersen-Bjergaard, P. Albertsen, G. Greisen, K. Lundstrøm, and J. Struck, “Inhalation of aerosolized surfactant (Exosurf®) to neonates treated with nasal continuous positive airway pressure,” *Prenatal and Neonatal Medicine*, vol. 3, no. 3, pp. 346–352, 1998.

[158] E. Berggren *et al.*, “Pilot study of nebulized surfactant therapy for neonatal respiratory distress syndrome,” *Acta Paediatr*, vol. 89, no. 4, pp. 460–464, 2000.

[159] H. Bahlmann, B. Sun, G. Nilsson, T. Curstedt, and B. Robertson, “Aerosolized surfactant in lung-lavaged adult rats: factors influencing the therapeutic response,” *Acta Anaesthesiol Scand*, vol. 44, no. 5, pp. 612–622, 2000.

[160] N. N. Finer, T. A. Merritt, G. Bernstein, L. Job, J. Mazela, and R. Segal, “An open label, pilot study of Aerosurf® combined with nCPAP to prevent RDS in preterm neonates,” *J Aerosol Med Pulm Drug Deliv*, vol. 23, no. 5, pp. 303–309, 2010.

[161] C. Dani *et al.*, “A Randomized, Controlled Trial to Investigate the Efficacy of Nebulized Poractant Alfa in Premature Babies with Respiratory Distress Syndrome,” *J Pediatr*, 2022, doi: 10.1016/j.jpeds.2022.02.054.

[162] J. Pérez-Gil and K. M. W. Keough, “Interfacial properties of surfactant proteins,” *Biochimica et Biophysica Acta (BBA)-Molecular Basis of Disease*, vol. 1408, no. 2–3, pp. 203–217, 1998.

[163] J. B. de la Serna *et al.*, “Segregated ordered lipid phases and protein-promoted membrane cohesivity are required for pulmonary surfactant films to stabilize and protect the respiratory surface,” *Faraday Discuss*, vol. 161, pp. 535–548, 2013.

[164] U. Klenz, M. Saleem, M. C. Meyer, and H.-J. Galla, “Influence of lipid saturation grade and headgroup charge: a refined lung surfactant adsorption model,” *Biophys J*, vol. 95, no. 2, pp. 699–709, 2008.

[165] V. Schram, W. R. Anyan, and S. B. Hall, “Non-cooperative effects of lung surfactant proteins on early adsorption to an air/water interface,” *Biochimica et Biophysica Acta (BBA)-Biomembranes*, vol. 1616, no. 2, pp. 165–173, 2003.

[166] R. Qanbar, S. Cheng, F. Possmayer, and S. Schurch, “Role of the palmitoylation of surfactant-associated protein C in surfactant film formation and stability,” *American Journal of Physiology-Lung Cellular and Molecular Physiology*, vol. 271, no. 4, pp. L572–L580, 1996.

[167] M. Gustafsson, M. Palmblad, T. Curstedt, J. Johansson, and S. Schürch, “Palmitoylation of a pulmonary surfactant protein C analogue affects the surface associated lipid reservoir and film stability,” *Biochimica et Biophysica Acta (BBA)-Biomembranes*, vol. 1466, no. 1–2, pp. 169–178, 2000.

[168] D. Schürch, O. L. Ospina, A. Cruz, and J. Pérez-Gil, “Combined and independent action of proteins SP-B and SP-C in the surface behavior and mechanical stability of pulmonary surfactant films,” *Biophys J*, vol. 99, no. 10, pp. 3290–3299, 2010.

[169] K. Rodriguez-Capote, K. Nag, S. Schürch, and F. Possmayer, “Surfactant protein interactions with neutral and acidic phospholipid films,” *American Journal of Physiology-Lung Cellular and Molecular Physiology*, vol. 281, no. 1, pp. L231–L242, 2001.

[170] F. Baumgart, O. L. Ospina, I. Mingarro, I. Rodríguez-Crespo, and J. Pérez-Gil, “Palmitoylation of pulmonary surfactant protein SP-C is critical for its functional cooperation with SP-B to sustain compression/expansion dynamics in cholesterol-containing surfactant films,” *Biophys J*, vol. 99, no. 10, pp. 3234–3243, 2010.

[171] R. V Diemel, M. M. E. Snel, L. M. G. Van Golde, G. Putz, H. P. Haagsman, and J. J. Batenburg, “Effects of cholesterol on surface activity and surface topography of spread surfactant films,” *Biochemistry*, vol. 41, no. 50, pp. 15007–15016, 2002.

[172] L. Gómez-Gil, D. Schürch, E. Goormaghtigh, and J. Pérez-Gil, “Pulmonary surfactant protein SP-C counteracts the deleterious effects of cholesterol on the activity of surfactant films under physiologically relevant compression-expansion dynamics,” *Biophys J*, vol. 97, no. 10, pp. 2736–2745, 2009.

[173] H. Wu *et al.*, “Surfactant proteins A and D inhibit the growth of Gram-negative bacteria by increasing membrane permeability,” *J Clin Invest*, vol. 111, no. 10, pp. 1589–1602, 2003.

[174] F. X. McCormack, R. Gibbons, S. R. Ward, A. Kuzmenko, H. Wu, and G. S. Deepe, “Macrophage-independent fungicidal action of the pulmonary collectins,” *Journal of Biological Chemistry*, vol. 278, no. 38, pp. 36250–36256, 2003.

[175] J. M. Hickman-Davis, J. R. Lindsey, S. Zhu, and S. Matalon, “Surfactant protein A mediates mycoplasmacidal activity of alveolar macrophages,” *American Journal of Physiology-Lung Cellular and Molecular Physiology*, vol. 274, no. 2, pp. L270–L277, 1998.

[176] R. Pasula, J. R. Wright, D. L. Kachel, and W. J. Martin, “Surfactant protein A suppresses reactive nitrogen intermediates by alveolar macrophages in response to Mycobacterium tuberculosis,” *J Clin Invest*, vol. 103, no. 4, pp. 483–490, 1999.

[177] S. Hussain, J. R. Wright, and W. J. Martin, “Surfactant protein A decreases nitric oxide production by macrophages in a tumor necrosis factor-α–dependent mechanism,” *Am J Respir Cell Mol Biol*, vol. 28, no. 4, pp. 520–527, 2003.

[178] A. Aderem and R. J. Ulevitch, “Toll-like receptors in the induction of the innate immune response,” *Nature*, vol. 406, no. 6797, pp. 782–787, 2000.

[179] H. Sano, K. Nagai, H. Tsutsumi, and Y. Kuroki, “Lactoferrin and surfactant protein A exhibit distinct binding specificity to F protein and differently modulate respiratory syncytial virus infection,” *Eur J Immunol*, vol. 33, no. 10, pp. 2894–2902, 2003.

[180] H. Sano, H. Sohma, T. Muta, S. Nomura, D. R. Voelker, and Y. Kuroki, “Pulmonary surfactant protein A modulates the cellular response to smooth and rough lipopolysaccharides by interaction with CD14,” *The Journal of Immunology*, vol. 163, no. 1, pp. 387–395, 1999.

[181] H. Sano, H. Chiba, D. Iwaki, H. Sohma, D. R. Voelker, and Y. Kuroki, “Surfactant proteins A and D bind CD14 by different mechanisms,” *Journal of Biological Chemistry*, vol. 275, no. 29, pp. 22442–22451, 2000.

[182] N. Holme and P. Chetcuti, “The pathophysiology of respiratory distress syndrome in neonates,” *Paediatr Child Health*, vol. 22, no. 12, pp. 507–512, 2012, Accessed: Sep. 27, 2023. [Online]. Available: https://doi.org/10.1016/j.paed.2012.09.001

[183] D. G. Sweet *et al.*, “European consensus guidelines on the management of respiratory distress syndrome–2019 update,” *Neonatology*, vol. 115, no. 4, pp. 432–450, 2019, doi: 10.1159/000499361.

[184] W. Göpel *et al.*, “Avoidance of mechanical ventilation by surfactant treatment of spontaneously breathing preterm infants (AMV): an open-label, randomised, controlled trial,” *The Lancet*, vol. 378, no. 9803, pp. 1627–1634, 2011, doi: 10.1016/S0140-6736(11)60986-0.

[185] M. X. Rojas-Reyes, C. J. Morley, and R. Soll, “Prophylactic versus selective use of surfactant in preventing morbidity and mortality in preterm infants,” *Cochrane Database of Systematic Reviews*, no. 3, 2012, doi: 10.1002/14651858.CD000510.pub2.

[186] M. Vento *et al.*, “Preterm resuscitation with low oxygen causes less oxidative stress, inflammation, and chronic lung disease,” *Pediatrics*, vol. 124, no. 3, pp. e439–e449, 2009, doi: 10.1542/peds.2009-0434.

[187] C. Moretti *et al.*, “Synchronized nasal intermittent positive pressure ventilation of the newborn: technical issues and clinical results,” *Neonatology*, vol. 109, no. 4, pp. 359–365, 2016, doi: 10.1159/000444898.

[188] L. S. Owen and B. J. Manley, “Nasal intermittent positive pressure ventilation in preterm infants: equipment, evidence, and synchronization,” in *Seminars in Fetal and Neonatal Medicine*, Elsevier, 2016, pp. 146–153. doi: 10.1016/j.siny.2016.01.003.

[189] M. S. Dunn *et al.*, “Randomized trial comparing 3 approaches to the initial respiratory management of preterm neonates,” *Pediatrics*, vol. 128, no. 5, pp. e1069–e1076, 2011, doi: 10.1542/peds.2010-3848.

[190] E. Herting, C. Härtel, and W. Göpel, “Less invasive surfactant administration (LISA): chances and limitations,” *Archives of Disease in Childhood-Fetal and Neonatal Edition*, vol. 104, no. 6, pp. F655–F659, 2019, Accessed: Sep. 17, 2023. [Online]. Available: http://dx.doi.org/10.1136/archdischild-2018-316557

[191] J. J. Pillow and S. Minocchieri, “Innovation in surfactant therapy II: surfactant administration by aerosolization,” *Neonatology*, vol. 101, no. 4, pp. 337–344, 2012, doi: 10.1159/000337354.

[192] N. N. Finer, T. A. Merritt, G. Bernstein, L. Job, J. Mazela, and R. Segal, “An open label, pilot study of Aerosurf® combined with nCPAP to prevent RDS in preterm neonates,” *J Aerosol Med Pulm Drug Deliv*, vol. 23, no. 5, pp. 303–309, 2010, doi: 10.1089/jamp.2009.0758.

[193] J. B. Fink, “Aerosol delivery to ventilated infant and pediatric patients,” *Respir Care*, vol. 49, no. 6, pp. 653–665, 2004.

[194] E. Köhler, G. Jilg, S. Avenarius, and G. Jorch, “Lung deposition after inhalation with various nebulisers in preterm infants,” *Archives of Disease in Childhood-Fetal and Neonatal Edition*, vol. 93, no. 4, pp. F275–F279, 2008, doi: 10.1136/adc.2007.121285.

[195] K. K. El Taoum, J. Xi, J. Kim, and A. Berlinski, “In vitro evaluation of aerosols delivered via the nasal route,” *Respir Care*, vol. 60, no. 7, pp. 1015–1025, 2015, doi: 10.4187/respcare.03606.

[196] W. T. McNicholas, “The nose and OSA: variable nasal obstruction may be more important in pathophysiology than fixed obstruction,” *European Respiratory Journal*, vol. 32, no. 1. Eur Respiratory Soc, pp. 3–8, 2008. doi: 10.1183/09031936.00050208.

[197] D. Waisman, “Non-traumatic nasopharyngeal suction in premature newborn infants with upper airway obstruction from secretions following nasal CPAP,” *J Pediatr*, vol. 149, no. 2, p. 279, 2006, doi: 10.1016/j.jpeds.2006.02.044.

[198] S. Tavernini, T. K. Church, D. A. Lewis, M. Noga, A. R. Martin, and W. H. Finlay, “Deposition of micrometer-sized aerosol particles in neonatal nasal airway replicas,” *Aerosol Science and Technology*, vol. 52, no. 4, pp. 407–419, 2018, doi: 10.1080/02786826.2017.1413489.

[199] T. E. Corcoran *et al.*, “Deposition studies of aerosol delivery by nasal cannula to infants,” *Pediatr Pulmonol*, vol. 54, no. 8, pp. 1319–1325, 2019, doi: 10.1002/ppul.24326.

[200] F. Réminiac *et al.*, “Nasal high flow nebulization in infants and toddlers: an in vitro and in vivo scintigraphic study,” *Pediatr Pulmonol*, vol. 52, no. 3, pp. 337–344, 2017, doi: 10.1002/ppul.23509.

[201] J. C. Dubus *et al.*, “Aerosol deposition in neonatal ventilation,” *Pediatr Res*, vol. 58, no. 1, pp. 10–14, 2005, doi: 10.1203/01.PDR.0000156244.84422.55.

[202] S. Tiemersma, S. Minocchieri, R. A. van Lingen, M. Nelle, and S. G. Devadason, “Vibrating membrane devices deliver aerosols more efficient than standard devices: a study in a neonatal upper airway model,” *J Aerosol Med Pulm Drug Deliv*, vol. 26, no. 5, pp. 280–286, 2013, doi: 10.1089/jamp.2012.0993.

[203] C. A. Sennoga *et al.*, “On sizing and counting of microbubbles using optical microscopy,” *Ultrasound Med Biol*, vol. 36, no. 12, pp. 2093–2096, 2010.

[204] D. F. Kienle, J. V De Souza, E. B. Watkins, and T. L. Kuhl, “Thickness and refractive index of DPPC and DPPE monolayers by multiple-beam interferometry,” *Anal Bioanal Chem*, vol. 406, pp. 4725–4733, 2014.

[205] S. A. Jones, G. P. Martin, and M. B. Brown, “High-pressure aerosol suspensions—A novel laser diffraction particle sizing system for hydrofluoroalkane pressurised metered dose inhalers,” *Int J Pharm*, vol. 302, no. 1–2, pp. 154–165, 2005.

[206] A. Haynes, M. S. Shaik, H. Krarup, and M. Singh, “Evaluation of the Malvern Spraytec® with inhalation cell for the measurement of particle size distribution from metered dose inhalers,” *J Pharm Sci*, vol. 93, no. 2, pp. 349–363, 2004.

[207] T. Ghazanfari, A. M. A. Elhissi, Z. Ding, and K. M. G. Taylor, “The influence of fluid physicochemical properties on vibrating-mesh nebulization,” *Int J Pharm*, vol. 339, no. 1–2, pp. 103–111, 2007.

[208] J. C. Waldrep and R. Dhand, “Advanced nebulizer designs employing vibrating mesh/aperture plate technologies for aerosol generation,” *Curr Drug Deliv*, vol. 5, no. 2, pp. 114–119, 2008.

[209] S. Garg, A. A. Thomas, and M. A. Borden, “The effect of lipid monolayer in-plane rigidity on in vivo microbubble circulation persistence,” *Biomaterials*, vol. 34, no. 28, pp. 6862–6870, 2013.

[210] M. H. Dave, M. Kemper, A. R. Schmidt, C. P. Both, and M. Weiss, “Pediatric airway dimensions—a summary and presentation of existing data,” *Pediatric Anesthesia*, vol. 29, no. 8, pp. 782–789, 2019, doi: 10.1111/pan.13665.

[211] K. Bass *et al.*, “Characterizing the effects of nasal prong interfaces on aerosol deposition in a preterm infant nasal model,” *AAPS PharmSciTech*, vol. 23, no. 5, p. 114, 2022.

[212] F. Bianco *et al.*, “Aerosol drug delivery to spontaneously-breathing preterm neonates: lessons learned,” *Respir Res*, vol. 22, pp. 1–31, 2021.

[213] E. Köhler, G. Jilg, S. Avenarius, and G. Jorch, “Lung deposition after inhalation with various nebulisers in preterm infants,” *Archives of Disease in Childhood-Fetal and Neonatal Edition*, 2008.

[214] G. Aladwani *et al.*, “Effects of Different Mesh Nebulizer Sources on the Dispersion of Powder Formulations Produced with a New Small-Particle Spray Dryer,” *Int J Pharm*, p. 123138, 2023.

[215] J. D. Schroeter, G. J. M. Garcia, and J. S. Kimbell, “Effects of surface smoothness on inertial particle deposition in human nasal models,” *J Aerosol Sci*, vol. 42, no. 1, pp. 52–63, 2011.

[216] H. Shi, C. Kleinstreuer, and Z. Zhang, “Modeling of inertial particle transport and deposition in human nasal cavities with wall roughness,” *J Aerosol Sci*, vol. 38, no. 4, pp. 398–419, 2007.

[217] N. Holme and P. Chetcuti, “The pathophysiology of respiratory distress syndrome in neonates,” *Paediatr Child Health*, vol. 22, no. 12, pp. 507–512, 2012, Accessed: Aug. 10, 2023. [Online]. Available: https://doi.org/10.1016/j.paed.2012.09.001

[218] N. Pickerd and S. Kotecha, “Pathophysiology of respiratory distress syndrome,” *Paediatr Child Health*, vol. 19, no. 4, pp. 153–157, 2009, Accessed: Aug. 10, 2023. [Online]. Available: https://doi.org/10.1016/j.paed.2008.12.010

[219] P. P. Hamilton *et al.*, “Comparison of conventional and high-frequency ventilation: oxygenation and lung pathology,” *J Appl Physiol*, vol. 55, no. 1, pp. 131–138, 1983.

[220] L. J. Björklund *et al.*, “Manual ventilation with a few large breaths at birth compromises the therapeutic effect of subsequent surfactant replacement in immature lambs,” *Pediatr Res*, vol. 42, no. 3, pp. 348–355, 1997, doi: 10.1203/00006450-199709000-00016.

[221] D. Kurepa, S. Perveen, Y. Lipener, and V. Kakkilaya, “The use of less invasive surfactant administration (LISA) in the United States with review of the literature,” *Journal of Perinatology*, vol. 39, no. 3, pp. 426–432, 2019.

[222] P. Pareek *et al.*, “Less invasive surfactant administration (LISA) vs. intubation surfactant extubation (InSurE) in preterm infants with respiratory distress syndrome: a pilot randomized controlled trial,” *J Trop Pediatr*, vol. 67, no. 4, p. fmab086, 2021, Accessed: Aug. 10, 2023. [Online]. Available: https://doi.org/10.1093/tropej/fmab086

[223] F. Bianco *et al.*, “Aerosol drug delivery to spontaneously-breathing preterm neonates: lessons learned,” *Respir Res*, vol. 22, no. 1, pp. 1–31, 2021, doi: 10.1186/s12931-020-01585-9.

[224] M. Aron, O. Vince, M. Gray, C. Mannaris, and E. Stride, “Investigating the role of lipid transfer in microbubble-mediated drug delivery,” *Langmuir*, vol. 35, no. 40, pp. 13205–13215, 2019, doi: 10.1021/acs.langmuir.9b02404.

[225] D. Carugo *et al.*, “Modulation of the molecular arrangement in artificial and biological membranes by phospholipid-shelled microbubbles,” *Biomaterials*, vol. 113, pp. 105–117, 2017, doi: 10.1016/j.biomaterials.2016.10.034.

[226] J. Owen *et al.*, “The Role of PEG-40-stearate in the Production, Morphology, and Stability of Microbubbles,” *Langmuir*, vol. 35, no. 31, pp. 10014–10024, 2018.

[227] M. Ibrahim *et al.*, “Polyethylene glycol (PEG): The nature, immunogenicity, and role in the hypersensitivity of PEGylated products,” *Journal of Controlled Release*, vol. 351, pp. 215–230, 2022.

[228] M. R. C. Marques, R. Loebenberg, and M. Almukainzi, “Simulated biological fluids with possible application in dissolution testing,” *Dissolution Technol*, vol. 18, no. 3, pp. 15–28, 2011.

[229] G. Stichtenoth, G. Walter, R. Lange, M. Raith, W. Bernhard, and E. Herting, “Surface tension of airway aspirates withdrawn during neonatal resuscitation reflects lung maturity,” *Pediatr*

Pulmonol, vol. 49, no. 8, pp. 751–756, 2014, Accessed: Aug. 10, 2023. [Online]. Available: https://doi.org/10.1002/ppul.22885

[230] J. D. Merrill *et al.*, “Dysfunction of pulmonary surfactant in chronically ventilated premature infants,” *Pediatr Res*, vol. 56, no. 6, pp. 918–926, 2004, Accessed: Aug. 10, 2023. [Online]. Available: https://doi.org/10.1203/01.PDR.0000145565.45490.D9

[231] M. Krzan, K. Lunkenheimer, and K. Malysa, “Pulsation and bouncing of a bubble prior to rupture and/or foam film formation,” *Langmuir*, vol. 19, no. 17, pp. 6586–6589, 2003, Accessed: Aug. 13, 2023. [Online]. Available: https://doi.org/10.1021/la020919r

[232] P. Wang and P. R. Brito-Parada, “Dynamics of a particle-laden bubble colliding with an air-liquid interface,” *Chemical Engineering Journal*, vol. 429, p. 132427, 2022, Accessed: Aug. 13, 2023. [Online]. Available: https://doi.org/10.1016/j.cej.2021.132427

[233] E. Rio and A. Biance, “Thermodynamic and mechanical timescales involved in foam film rupture and liquid foam coalescence,” *ChemPhysChem*, vol. 15, no. 17, pp. 3692–3707, 2014, Accessed: Aug. 13, 2023. [Online]. Available: https://doi.org/10.1002/cphc.201402195

[234] R. Pichot, R. L. Watson, and I. T. Norton, “Phospholipids at the interface: current trends and challenges,” *Int J Mol Sci*, vol. 14, no. 6, pp. 11767–11794, 2013, Accessed: Aug. 16, 2023. [Online]. Available: https://doi.org/10.3390/ijms140611767

[235] D. Langevin, “Influence of interfacial rheology on foam and emulsion properties,” *Adv Colloid Interface Sci*, vol. 88, no. 1–2, pp. 209–222, 2000, Accessed: Aug. 16, 2023. [Online]. Available: https://doi.org/10.1016/S0001-8686(00)00045-2

[236] C. F. Poets, A. Arning, W. Bernhard, C. Acevedo, and H. Von der Hardt, “Active surfactant in pharyngeal aspirates of term neonates: lipid biochemistry and surface tension function,” *Eur J Clin Invest*, vol. 27, no. 4, pp. 293–298, 1997, Accessed: Aug. 18, 2023. [Online]. Available: https://doi.org/10.1046/j.1365-2362.1997.1050655.x

[237] E. E. Williams *et al.*, “Functional morphometry: non-invasive estimation of the alveolar surface area in extremely preterm infants,” *Pediatr Res*, pp. 1–7, 2023, Accessed: Aug. 18, 2023. [Online]. Available: https://doi.org/10.1038/s41390-023-02597-z

[238] L. J. Smith, K. O. McKay, P. P. van Asperen, H. Selvadurai, and D. A. Fitzgerald, “Normal development of the lung and premature birth,” *Paediatr Respir Rev*, vol. 11, no. 3, pp. 135–142, 2010, Accessed: Sep. 27, 2023. [Online]. Available: https://doi.org/10.1016/j.prrv.2009.12.006

[239] A. Apisarnthanarak, G. Holzmann-Pazgal, A. Hamvas, M. A. Olsen, and V. J. Fraser, “Ventilator-associated pneumonia in extremely preterm neonates in a neonatal intensive care unit: characteristics, risk factors, and outcomes,” *Pediatrics*, vol. 112, no. 6, pp. 1283–1289, 2003, Accessed: Sep. 28, 2023. [Online]. Available: https://doi.org/10.1542/peds.112.6.1283

[240] T. Kobayashi, K. Nitta, M. Ganzuka, S. Inui, G. Grossmann, and B. Robertson, “Inactivation of exogenous surfactant by pulmonary edema fluid,” *Pediatr Res*, vol. 29, no. 4, pp. 353–356, 1991, Accessed: Oct. 02, 2023. [Online]. Available: https://doi.org/10.1203/00006450-199104000-00005

[241] T. Fuchimukai, T. Fujiwara, A. Takahashi, and G. Enhorning, “Artificial pulmonary surfactant inhibited by proteins,” *J Appl Physiol*, vol. 62, no. 2, pp. 429–437, 1987, Accessed: Oct. 02, 2023. [Online]. Available: https://doi.org/10.1152/jappl.1987.62.2.429

[242] M. Rüdiger, W. Friedrich, B. Rüstow, G. Schmalisch, and R. Wauer, “Disturbed surface properties in preterm infants with pneumonia,” *Neonatology*, vol. 79, no. 2, pp. 73–78, 2001, Accessed: Oct. 02, 2023. [Online]. Available: https://doi.org/10.1159/000047070

[243] S. Deshpande, P. Suryawanshi, K. Ahya, R. Maheshwari, and S. Gupta, “Surfactant therapy for early onset pneumonia in late preterm and term neonates needing mechanical ventilation,” *J Clin Diagn Res*, vol. 11, no. 8, p. SC09, 2017, Accessed: Oct. 01, 2023. [Online]. Available: https://doi.org/10.7860%2FJCDR%2F2017%2F28523.10520

[244] M. Ikegami *et al.*, “Intratracheal recombinant surfactant protein D prevents endotoxin shock in the newborn preterm lamb,” *Am J Respir Crit Care Med*, vol. 173, no. 12, pp. 1342–1347, 2006, Accessed: Oct. 01, 2023. [Online]. Available: https://doi.org/10.1164/rccm.200509-1485OC

[245] J. Wirbelauer and C. P. Speer, “The role of surfactant treatment in preterm infants and term newborns with acute respiratory distress syndrome,” *Journal of Perinatology*, vol. 29, no. 2, pp. S18–S22, 2009, Accessed: Oct. 02, 2023. [Online]. Available: https://doi.org/10.1038/jp.2009.30

[246] J. R. Wright, “Immunoregulatory functions of surfactant proteins,” *Nat Rev Immunol*, vol. 5, no. 1, pp. 58–68, 2005, Accessed: Oct. 01, 2023. [Online]. Available: https://doi.org/10.1038/nri1528

[247] S. P. Keese, K. Brandenburg, M. Roessle, and A. B. Schromm, “Pulmonary surfactant protein A-induced changes in the molecular conformation of bacterial deep-rough LPS lead to reduced activity on human macrophages,” *Innate Immun*, vol. 20, no. 8, pp. 787–798, 2014, Accessed: Oct. 06, 2023. [Online]. Available: https://doi.org/10.1177/1753425913506269

[248] M. Yamazoe *et al.*, “Pulmonary surfactant protein D inhibits lipopolysaccharide (LPS)-induced inflammatory cell responses by altering LPS binding to its receptors,” *Journal of Biological Chemistry*, vol. 283, no. 51, pp. 35878–35888, 2008, Accessed: Oct. 06, 2023. [Online]. Available: https://doi.org/10.1074/jbc.M807268200

[249] V. Sender, L. Lang, and C. Stamme, “Surfactant protein-A modulates LPS-induced TLR4 localization and signaling via β-arrestin 2,” *PLoS One*, vol. 8, no. 3, p. e59896, 2013, Accessed: Oct. 08, 2023. [Online]. Available: https://doi.org/10.1371/journal.pone.0059896

[250] L. N. Henning, A. K. Azad, K. V. L. Parsa, J. E. Crowther, S. Tridandapani, and L. S. Schlesinger, “Pulmonary surfactant protein A regulates TLR expression and activity in human macrophages,” *The Journal of Immunology*, vol. 180, no. 12, pp. 7847–7858, 2008, Accessed: Oct. 08, 2023. [Online]. Available: https://doi.org/10.4049/jimmunol.180.12.7847

[251] W. Abate, A. A. Alghaithy, J. Parton, K. P. Jones, and S. K. Jackson, “Surfactant lipids regulate LPS-induced interleukin-8 production in A549 lung epithelial cells by inhibiting translocation of TLR4 into lipid raft domains,” *J Lipid Res*, vol. 51, no. 2, pp. 334–344, 2010, Accessed: Oct. 08, 2023. [Online]. Available: https://doi.org/10.1194/jlr.M000513

[252] H. C. Kim and Y.-Y. Won, “Clinical, technological, and economic issues associated with developing new lung surfactant therapeutics,” *Biotechnol Adv*, vol. 36, no. 4, pp. 1185–1193, 2018, doi: 10.1016/j.biotechadv.2018.03.017.

[253] C. Liu *et al.*, “Mite allergen induces nitric oxide production in alveolar macrophage cell lines via CD14/toll-like receptor 4, and is inhibited by surfactant protein D,” *Clinical & Experimental Allergy*, vol. 35, no. 12, pp. 1615–1624, 2005.

[254] Y. Tomita, A. Rikimaru-Kaneko, K. Hashiguchi, and S. Shirotake, “Effect of anionic and cationic n-butylcyanoacrylate nanoparticles on NO and cytokine production in Raw264. 7 cells,” *Immunopharmacol Immunotoxicol*, vol. 33, no. 4, pp. 730–737, 2011.

[255] J. S. Vankayala *et al.*, “Surfactants and fatty alcohol based novel nanovesicles for resveratrol: Process optimization, characterization and evaluation of functional properties in RAW 264.7 macrophage cells,” *J Mol Liq*, vol. 261, pp. 387–396, 2018.

[256] J. Armstrong *et al.*, “Synergistic effects of p38 mitogen-activated protein kinase inhibition with a corticosteroid in alveolar macrophages from patients with chronic obstructive pulmonary disease,” *Journal of Pharmacology and Experimental Therapeutics*, vol. 338, no. 3, pp. 732–740, 2011.

[257] O. Michel *et al.*, “Evaluation of oral corticosteroids and phosphodiesterase-4 inhibitor on the acute inflammation induced by inhaled lipopolysaccharide in human,” *Pulm Pharmacol Ther*, vol. 20, no. 6, pp. 676–683, 2007.

[258] L. N. Henning, A. K. Azad, K. V. L. Parsa, J. E. Crowther, S. Tridandapani, and L. S. Schlesinger, “Pulmonary surfactant protein A regulates TLR expression and activity in human macrophages,” *The Journal of Immunology*, vol. 180, no. 12, pp. 7847–7858, 2008.

[259] A. Salminen, R. Vuolteenaho, R. Paananen, M. Ojaniemi, and M. Hallman, “Surfactant protein A modulates the lipopolysaccharide-induced inflammatory response related to preterm birth,” *Cytokine*, vol. 56, no. 2, pp. 442–449, 2011.

[260] M. Koptides, T. M. Umstead, J. Floros, and D. S. Phelps, “Surfactant protein A activates NF-kappa B in the THP-1 monocytic cell line,” *American Journal of Physiology-Lung Cellular and Molecular Physiology*, vol. 273, no. 2, pp. L382–L388, 1997.

[261] V. Sender, L. Lang, and C. Stamme, “Surfactant protein-A modulates LPS-induced TLR4 localization and signaling via β-arrestin 2,” *PLoS One*, vol. 8, no. 3, p. e59896, 2013.

[262] M. Mueller, K. Brandenburg, R. Dedrick, A. B. Schromm, and U. Seydel, “Phospholipids inhibit lipopolysaccharide (LPS)-induced cell activation: a role for LPS-binding protein,” *The Journal of Immunology*, vol. 174, no. 2, pp. 1091–1096, 2005.

[263] W. Abate, A. A. Alghaithy, J. Parton, K. P. Jones, and S. K. Jackson, “Surfactant lipids regulate LPS-induced interleukin-8 production in A549 lung epithelial cells by inhibiting translocation of TLR4 into lipid raft domains,” *J Lipid Res*, vol. 51, no. 2, pp. 334–344, 2010.

[264] J. Q. Hiansen *et al.*, “Cholesterol-mediated surfactant dysfunction is mitigated by surfactant protein A,” *Biochimica et Biophysica Acta (BBA)-Biomembranes*, vol. 1848, no. 3, pp. 813–820, 2015.

[265] V. A. Brans, M. D. Gray, E. Sezgin, and E. P. J. Stride, “Protein-Decorated Microbubbles for Ultrasound-Mediated Cell Surface Manipulation,” *ACS Appl Bio Mater*, 2023.

[266] H. J. Knowles *et al.*, “Use of oxygen-loaded nanobubbles to improve tissue oxygenation: Bone-relevant mechanisms of action and effects on osteoclast differentiation,” *Biomaterials*, p. 122448, 2023.

[267] M. Ikegami, F. H. Adams, B. Towers, and A. B. Osher, “The quantity of natural surfactant necessary to prevent the respiratory distress syndrome in premature lambs,” *Pediatr Res*, vol. 14, no. 9, pp. 1082–1085, 1980.

[268] F. H. Adams, B. Towers, A. B. Osher, M. Ikegami, T. Fujiwara, and M. Nozaki, “Effects of tracheal instillation of natural surfactant in premature lambs. I. Clinical and autopsy findings,” *Pediatr Res*, vol. 12, no. 8, pp. 841–848, 1978.

[269] A. Jobe, M. Ikegami, T. Glatz, Y. Yoshida, E. Diakomanolis, and J. Padbury, “Duration and characteristics of treatment of premature lambs with natural surfactant.,” *J Clin Invest*, vol. 67, no. 2, pp. 370–375, 1981.

[270] C. Rey-Santano, V. Mielgo, E. Gastiasoro, A. Valls-i-Soler, and X. Murgia, “Effect of surfactant and partial liquid ventilation treatment on gas exchange and lung mechanics in immature lambs: influence of gestational age,” *PLoS One*, vol. 8, no. 2, p. e56127, 2013.

[271] J. Mazela, T. A. Merritt, M. H. Terry, T. J. Gregory, and A. B. Blood, “Comparison of poractant alfa and lyophilized lucinactant in a preterm lamb model of acute respiratory distress,” *Pediatr Res*, vol. 72, no. 1, pp. 32–37, 2012.

[272] E. Gastiasoro-Cuesta, F. J. Alvarez-Diaz, C. Rey-Santano, A. Arnaiz-Renedo, B. Loureiro-Gonzalez, and A. Valls-i-Soler, “Acute and sustained effects of lucinactant versus poractant-α on pulmonary gas exchange and mechanics in premature lambs with respiratory distress syndrome,” *Pediatrics*, vol. 117, no. 2, pp. 295–303, 2006.

[273] D. K. Rahmel *et al.*, “The non-intubated, spontaneously breathing, continuous positive airway pressure (CPAP) ventilated pre-term lamb: a unique animal model,” *Reproductive Toxicology*, vol. 34, no. 2, pp. 204–215, 2012.